253#15#MT#DAR-FPP

Design of Morphing Leading and Trailing Edge Surfaces for Camber and Twist Control

G.B. Spirlet

23 June 2015

Faculty of Aerospace Engineering · Delft University of Technology

Design of Morphing Leading and Trailing Edge Surfaces for Camber and Twist Control

For obtaining the degree of Master of Science in Aerospace Engineering at Delft University of Technology

G.B. Spirlet

23 June 2015

Faculty of Aerospace Engineering · Delft University of Technology

Delft University Of Technology
Department Of
Flight Propulsion and Performance

The undersigned hereby certify that they have read and recommend to the Faculty of Aerospace Engineering for acceptance a thesis entitled **"Design of Morphing Leading and Trailing Edge Surfaces for Camber and Twist Control"** by **G.B. Spirlet** in partial fulfillment of the requirements for the degree of **Master of Science**.

Dated: 23 June 2015

Head of department: _____
Prof.dr.ir. L.L.M. Veldhuis

Supervisor: _____
dr.ir. R. De Breuker

Supervisor: _____
dr. J. Sodja

Supervisor: _____
ir. N.P.M. Werter

Summary

The application of morphing structures in conventional aircraft is a method to improve aircraft performance by both reducing the total fuel consumption for a given mission profile, or by allowing one type of aircraft to perform a wider range of missions. The current generation of aircraft does not widely use morphing technology to optimize flight performance, instead specialized types are developed specifically for one target mission.

This report shows the process of integrating a span, twist and camber morphing system into an unmanned testbed as part of the CHANGE project. First several configuration concepts are proposed and evaluated which allow the twist/camber system to be developed independently from the span extension system. This results in a wing design where the leading and trailing edges contain the morphing mechanism, while the central wing box provides space for the span extension mechanism. The application of morphing surfaces is also limited to the inboard wing sections, as the internal volume of the tips is dedicated entirely to housing the extending wing sections.

Several options for the morphing mechanisms are discussed and traded off, though eventually a novel system is developed based on open section torsion for twist control and sheet bending for camber control. The magnitude of the deformation required to meet pre-determined target shapes is calculated via numerical simulation, as are the forces which are imparted on the structure and the actuators by elastic loads. Aerodynamic loads are also calculated. Finally, a detail design is proposed for both the leading and trailing edge mechanisms which satisfies the required camber and twist ranges while taking into consideration the maintainability of the structure and availability of parts. The design consists of a GFRP skin of which the top surface acts as a compliant hinge. The lower surface of the skin is supported and constrained by an internal mechanism, while actuation is provided by electric servos. The symmetry of the final design allows for left to right interchangeability of the entire control surface.

Acknowledgments

It is not until the realization sets in that the rest of the report is finished, or rather, when that moment is reached where further effort would yield diminishing returns, that this chapter is provided with content. But whatever the reasons for procrastinating, the chore of generating filler remains. The approach to such a task is routine by now: don't waste any time reinventing the wheel, have a quick look around to check up on the state of the art. It turns out that the conventional use for this section would be to express gratitude towards friends, family, colleagues and figments of schizophrenic delusions. There is typically also a great deal of nostalgic retrospection involved. With almost nine year to recount, perhaps it is best to skip straight to what I know now.

If only I knew then what I know now.... Though to be honest the extent of my knowledge is not exactly all-encompassing. Don't panic, a degree simply implies one meets the minimum requirements to be set loose in the wide world. It is not an indication of supremacy in your field. This would be rather like comparing a swimming diploma with an Olympic gold medal. When using this analogy it must be said that it is quite possible and even quite common for one swimmer to dominate various if not all disciplines of swimming. In contrast it is not quite so common for one person to be the leader in all fields of engineering. Alas the once revered universal renaissance man is no longer considered a feasible ideal. Instead this has devaluated into the concept of a T-shaped engineer where coping with the ever advancing state of the art has led to multidisciplinary skills becoming increasingly shallow and the in depth knowledge becoming increasingly narrow.

When faced with the situation that so much is yet to be learned, the primary question of the individual is never of *how* to do so, as after all, gathering knowledge is the core business of students. The question of *what* to learn is much more difficult to answer. It is all too easy to carry on in the comfort your own field, digging an ever deeper and narrower hole into the landscape, at the risk of losing sight of the bigger picture above, becoming increasingly good at very little, until you are the world's best at absolutely nothing. Others might tend to climb out and prod around at the surface, gradually raking at the terrain around them, only looking deeper when necessary. It comes down to two different mindsets. The first takes the path of least resistance to invent new solutions to existing

problems, the less time spent digging the better. The second feels compelled to invent questions for the purpose of making his hole deeper. The first is an engineer, the second is a scientist.

There is a symbiotic relation between these two professions. The advancing state of the art provided by science offers a broader toolbox for the engineer, while the commercial applications of new technology finances the scientist's research. But what is the ideal ratio of these professions out in the wild? The Airbus Group spent 3 over billion euro on R&D during FY2013, the turnover that year was 59 billion. Let's assume that the demand for scientists within this organization can be quantified by the fraction of R&D costs, then the mere five percent which is dedicated to research reflects that this demand is overwhelmingly small.

If pride is taken from the widely spread notion that Aerospace Engineering at TU Delft has the most difficult curriculum of the country then is it not worth questioning whether this added difficulty adds to the graduates' value as innovators of technology? If a materials and manufacturing 'practical' at this faculty consist of watching a discovery channel documentary about the A380 in a lecture room, then can this be made up at a later stage by cramming more theoretical knowledge? First year students build their own wing box, they are even allowed to operate the rivet guns themselves, but you might as well let them assemble an Ikea cupboard. The thickness of the skin is fixed, so is the choice of material, and so is the geometry of the wingbox. Of course these variables are removed to match the current knowledge of the students, but such manufacturing projects are not repeated at a later stage where the intellect should allow for more freedom in construction choices. Quite to the contrary, all later group projects stop at a conceptual level, and the end result is at best a shiny CATIA rendering and a stack of paper. No one ever has to contact a supplier or manufacturer to ask whether what they just drew can actually be made. And as a result no time is spent on how to draw things that *can* be made. If the iterative design process is performed merely up to the conceptual design level, and very rarely to the detail design level, then no one learns the harsh and priceless lesson of a failed prototype.

This conveniently upholds the illusion of the *first time right design*, the belief that rationale and thorough analysis is enough to predict all shortcomings and solve all problems without the need for prototyping. The result of all this is a level of Quixotism which is difficult to indicate on the two-dimensional space of the T-shaped knowledge sketch, perhaps a third dimension must be added to indicate one's capacities in pragmatic know-how and independence. Another dimension could be used to indicate the level of affinity for hardware over software.

In the end, academic institutions do a good job at providing a basis in engineering skills and knowledge, but they do not hold a monopoly. Ultimately every individual is responsible for his own intellectual formation, but while the required complementary experience can always be obtained elsewhere; the diploma can not.

Delft, The Netherlands G.B. Spirlet
23 June 2015

Contents

List of Figures

List of Tables

Nomenclature

α_t	Local twist angle
δ_{LE}	Deflection at leading edge
δ_{TE}	Deflection at trailing edge
μ_g	Gust alleviation factor
ρ	Air density
K_g	Aeroplane mass ratio
n_1	Limit load factor
n_g	Gust load at cruise speed
U_{de}	Gust velocity
V_A	Manoeuvring speed
V_B	Max gust speed
V_C	Cruise speed
V_D	Dive speed
V_S	Stall speed
V_{Amin}	Minimum allowed manoeuvring speed
V_{Cmin}	Minimum allowed cruise speed
V_{Dmin}	Minimum allowed dive speed
V_{Fmin}	Minimum allowed flap speed
a	Normal force slope
C	Mean geometric chord
c	Airfoil chord
$C_{L\alpha}$	Wing lift slope
CHANGE	Combined morphing assessment using flight envelope data and mission based morphing prototype wing development
EPDM	Ethylene propylene diene monomer

EPP	Expanded polypropylene
g	Gravitational acceleration
L/D	Lift to drag ratio
m	Camber relative to chord
MTOW	Maximum takeoff weight
UAV	Unmanned aerial vehicle
UBI	Universidade da Beira Interior
V	Airspeed

Chapter 1

Introduction

Wings of aircraft are typically designed for a narrow band of cruise conditions where optimum performance is achieved. Even if all design decisions take into account the penalties inflicted on other flight conditions, these penalties are weighted according to the aircraft's expected flight profiles during service. This results in specialized aircraft which do not perform optimally when used in off design flight conditions. A common example of compromise in conflicting requirements is the wing planform area: a larger wing improves short field performance, and a small wing improves cruise performance. Conventional high lift devices can be used to satisfy the field performance requirements at the expense of increased weight at little added drag in the cruise design condition [29]. The operational use of such discrete aerodynamic surfaces is further discretized by regarding their deployment as a departure from the aircraft's 'clean' configuration, and these are therefore rarely used to tweak performance during flight. Some fighter aircraft and sailplanes form an exception to this mindset, as these use leading and trailing edge flaps to continually optimize the aircraft angle of attack during manoeuvres [14].

Morphing can be described as a set of technologies that increase a vehicle's performance by manipulating certain characteristics to better match the vehicle state to the environment and the task at hand [1]. Conventional slats, flaps and even ailerons could therefore be considered as morphing systems by this definition. A common, though false [30], sentimental connotation of morphing is that the geometry of the wing is changed seamlessly with no gaps or discontinuities, though this would imply that true morphing falls under the category of science fiction fantasies which can not be achieved using currently available technology. A definition may be found in that morphing aircraft are designed specifically to incorporate adaptive geometry features which can continually be modified to achieve optimal performance in flight, and that systems are installed to monitor flight conditions and make adjustments accordingly. This defines morphing not as a group of technologies or mechanisms, but rather as how these technologies are used both during the design stage and in flight.

Trivial components such as landing gear satisfy only two of the three properties. If the designer deems the added complexity and weight of retractable landing gear to outweigh the

drag penalty of a fixed undercarriage then the former will be fitted. Operating procedures during take off and landing ensures that the gear is not deployed when it is not needed, e.g. it is retracted as soon as a certain climb rate is reached [8]. However, typically the landing gear only has two positions, up and down, and partially deploying landing gear to improve flight characteristics is only incidentally applied in emergencies [20]. A common example of a rigid actuated structure which can be considered as a morphing system is the variable sweep wing. This technology was developed in the 1960's to meet the requirement of aircraft which could combine long range high altitude cruise and low level supersonic flight. An example of the morphing approach used on a swing-wing design is found in the Grumman F14, where the optimum wing sweep angle is automatically adjusted in function of Mach number and pressure altitude for optimum manoeuvre performance whilst limiting the root bending moment [16]. The addition of a variable sweep mechanism represents a significant structural weight, but in the case of the F14 this is justified as a fixed-geometry aircraft with equivalent loiter, short field and high speed capabilities was estimated to be considerably heavier [31]. Other swing wing aircraft such as the F111 and MiG23 where the sweep angle is manually selected from several pre-set angles can also be considered as morphing provided that this angle is procedurally selected in function of the flight conditions.

A concept as drastic as a variable sweep wing is the result of almost diametrically opposed design requirements involving a capability in both high supersonic speeds and extended subsonic range. Commercial aviation tends to have more subtle variations in flight conditions, thus more subtle geometry changes are sufficient to optimize for these. A study by Embraer indicates that a morphing system may result in L/D improvements of 10% to 25% throughout a typical transport aircraft cruise mission [3]. The morphing concept evaluated in the study consists of a rigid central wingbox section with articulated leading and trailing edges. The AFTI mission adaptive wing flying testbed has shown L/D improvements up to 15% in the transonic range by using adaptive flexible leading and trailing edge flaps. Improvements up to 100% have been measured in low speed flight [6]. The same testbed in an active gust alleviation configuration has shown 20% reductions in root bending moment [24].

The merit of hingeless high lift devices is that their low profile drag allows them to be used for in flight camber optimization. The added weight of such systems can thus be amortized by using them in more than one flight phase [18]. A weight penalty can be justified even if it creates a small advantage over a long time period. For one particular case study of a mission dominated by cruise and loiter, a 10% weight increase pays off if cruise is more than 25% of the total flight time [2].

A large volume of research can be found on the topic of morphing, though the technique is rarely applied to production aircraft. Some notable examples are the Grob elastic flap system used on the G104 [15], and the variable camber Krueger flaps on the Boeing 747 [19]. Except for some recent commercial projects [11], the interest in this field seems to have peaked in the 1980's, but the recent rise of unmanned aviation has provided a low cost platform on which to test morphing technologies and many universities have since conducted small scale adaptive wing research [27] [9] [10].

This report documents the design of control surfaces for an adaptive wing. Chapter 2 details the background of the project and outlines the requirements to be fulfilled. Chapter

3 lists the concepts that were evaluated for the project. All the concepts for the basic layout of the adaptive surfaces and the morphing method are described in detail and chosen by means of a trade-off. Chapter 4 looks into the displacement and forces involved in deforming the control surface so that it matches the target deformation requirements. The detail design of the mechanism is described in chapter 5, which also verifies the design by means of structural analysis on a component level. Finally, chapter 6 contains the procedures for assembly and maintenance of the mechanism.

Chapter 2

Requirements

This chapter will elaborate on the scope and the objectives of the work. First some information is given on the background of the project, and its goals. Some key requirements for the design of the morphing segments are determined on the basis of greater project requirements. The flight envelope is determined in order to allow adequate sizing of the structures which need to be designed.

2.1 CHANGE Project Background

The CHANGE project (Combined morphing assessment using flight envelope data and mission based morphing prototype wing development) is a project with the objective to study and develop a novel morphing system which integrates different morphing mechanisms into in a single wing. The resulting design will be flight tested on an unmanned aircraft which integrates three different morphing techniques: span extension, camber morphing and twist morphing. This is expected to result in an aircraft which can optimize its wing performance over a wide range of angles of attack and airspeeds, allowing efficient cruise as well as loitering capabilities within one aircraft type [23]. A total of nine partners are involved in this consortium, which includes universities and industry. As one of the project partners, TU Delft is to provide a design proposal for the camber and twist morphing system.

The impact of this project is projected to be the creation of technology which allows one (unmanned) aircraft type to be flown in several different mission profiles without redesign or modification. Another potential benefit is in using the morphing system as control surfaces, such as using wing twist or asymmetric span extension for roll control. Longer term improvements may be achieved in the fields of maneuverability, damage tolerance, and recovery from uncontrollable flight conditions, as well as improvements in fuel efficiency.

The test aircraft will be based on the TEKEVER AR4 UAV which is currently in development with one of the partners involved in the project. The parameters of the aircraft and the morphing wing have already been defined and are summarized in table 2.1

MTOW	25 kg
chord	600 mm
span	3-4 m
taper ratio	100%
sweep angle	0 °
airfoil thickness	10%
cruise speed	110 km/h
loiter speed	55 km/h
limit loads*	3.6g -1.6g
safety factor	1.5

*A rationale for increasing the limit load to 5.6g is given in this chapter.

Table 2.1: A summary of the aircraft parameters.

2.2 Target Wing Configuration

The requirements for the morphing system have also been provided from the onset of the project. Several target shapes were given which need to be reproduced. A total of three shapes were provided, each representing an optimal configuration for a specific flight condition [4] [5].

flight condition	take off	cruise	landing/loiter
tip twist	−2 °	−2 °	−3.6 °
tip airfoil	NACA 0010	NACA 0010	NACA 0010
root twist	0.5 °	0.2 °	2 °
root airfoil	NACA 3510	NACA 2510	NACA 6510
wing span	4m	3m	4m

Table 2.2: The wing shape specified in the design

These designs were obtained by iteratively optimizing the twist distribution of a rectangular wing to match a target lift distribution. The airfoil shape was determined in advance and was not changed during the optimization. The airfoil is not lofted along the span continuously, but remains the same as the root airfoil until the tip, where it is faired into a symmetric airfoil. The twist distribution is not linear, and changes for every configuration as shown in figure 2.1.

A notable feature is that the landing configuration is identical to the loiter configuration. Analysis has shown that this provides a sufficiently large lift coefficient to meet the landing speed requirements [5].

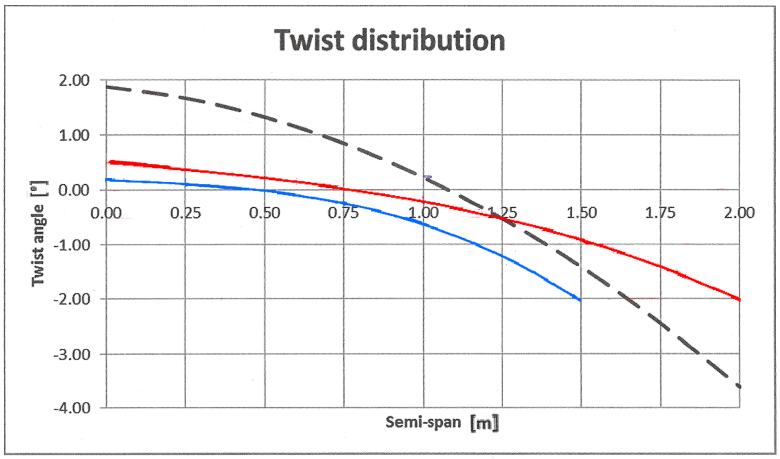

Figure 2.1: The target twist distribution for high speed flight (blue) takeoff (red) and landing/loiter (black dashed).

2.3 Flight Envelope

The flight envelope used for concept sizing is based on CS23 certification specifications [7]. Requirements stated by the project are that the wing should be stressed for -1.6 to 3.6g maneuvers, with an additional safety factor of 1.5. The two span configurations are treated as if they were two different aircraft in order to fully test the load factors compared to CS23 requirements. The values for lift slope and the maximum lift coefficient are taken from the ARA aerodynamic design report [5].

Mass	25kg	25kg
Wingspan	4m	3m
$C_{L\alpha}$	4.125	3.93
C_{Lmax}	1.52	1.45
Chord	0.6m	0.6m
Design speed	55km/h	110km/h

Table 2.3: The aircraft parameters used.

2.3.1 CS23 certification specifications

CS23 specifications are used to verify the load requirements. They specify the requirements an aircraft must fulfil in order to be certified. It is applicable to aircraft with a take-off weight of up to 5670 kg carrying up to 9 passengers excluding the pilot(s). The following paragraphs from CS23 were given as requirements for proposed load cases. A brief summary of the requirements is given for each paragraph and the results are assessed for compatibility with this aircraft. Mainly the paragraphs concerning the requirements of the load diagram are used, which determines maximum allowed load factor for every airspeed.

CS23.335 Design Airspeeds

This paragraph gives minimum and maximum values for airspeeds in various flight phases. The aircraft must be able to withstand various specific loads at each of these airspeeds. These speeds are given in equations in function of aircraft properties such as wing loading, stall speed and limit loads. As CS23 is heavily inspired by JAR23 the equations yield airspeed in knots. Table 2.4 lists the equations, while the resulting values are listed in table 2.5

-	-	Min value	Max value	Exact requirement
V_C	Cruise speed	$33\sqrt{W/S}$	$0.9V_H$	110km/h
V_{Cmin}				$17\sqrt{n_1 W/S}$
V_{Fmin}	Flap speed			$11\sqrt{n_1 W/S}$
V_D	Dive speed	$1.25V_C$ or $1.5V_{Cmin}$		
V_{Dmin}			$24\sqrt{n_1 W/S}$	
V_A	Maneuvering speed	$V_s\sqrt{n_1}$	V_C	
V_{Amin}				$15\sqrt{(n_1 W/S)}$
V_B	Max gust speed	$V_s\sqrt{(n_g)}$	V_C	

Table 2.4: CS23 requirements for V speeds, n_1 is the limit load factor and and n_g is the gust load at cruise speed

CS23.337 Limit manoeuvring load factors

This paragraph of the certification standards states that the positive limit load must be +4.4 or more for a utility class aircraft. The negative limit load must be -1.76. This exceeds the +3.6/-1.6 given by the project requirements.

CS23.341 Gust Load Factors

Gusts are sudden increases in upward wind velocity, these increase the angle of attack of the aircraft and therefore cause an increase in load factor. Some guideline equations are given for the loads that can be expected from gusts. These loads increase linearly in function of airspeed and gust speed. An approximation for the load factor caused by gusts is given by equation 2.1:

$$n = 1 \pm \frac{\rho_0 V a K_g U_{de}}{W/S} \tag{2.1}$$

$$K_g = \frac{0.88\mu_g}{5.3 + \mu_g} \tag{2.2}$$

$$\mu_g = \frac{2W/S}{\rho C a g} \tag{2.3}$$

μ_g and K_g are the gust alleviation factor and aeroplane mass ratio respectively. W/S is the wing loading in N/m^2, ρ is the air density (kg/m^3), C the mean geometric chord (m), a is the normal force slope (1/rad), g is the gravitational acceleration (m/s^2) and V the airspeed (m/s). U_{de} is the velocity of the gust in (m/s).

The values for the normal force slope were taken from the aerodynamic design report by ARA where available, and estimates were used when exact values could not be found. The assumption is made that the value is equivalent to the lift slope for low angles of attack.

The sensitivity to gusts is increased by low wing loading and high aspect ratios, therefore the effects on the loiter configuration are particularly dramatic. For example a gust of 12m/s is sufficient to cause a load of 3.6g at the loiter airspeed of 55km/h (15.3m/s) assuming that the wing does not stall as a result of the increase in angle of attack. Even the cruise configuration gets loaded by +5.6g and -3.6g when flying through a 50fps (15.25m/s) gust at cruise speed of 30m/s, which is a mandatory CS23 load case.

This situation also indicates that a 3.6g limit load is insufficient, though it must be said that encountering a 15m/s gust at a 300m cruise altitude is unlikely over flat terrain. Also the assumptions made in the gust load equation may not apply to an aircraft of this size and weight. Especially as the diameter of the gust distribution used in these assumptions is given in function of the mean chord of the aircraft. The gust model therefore assumes that the vertical velocity increases from zero to up to 66fps (20.1m/s) in the space of just 8m.

CS23.333 Flight Envelope

The flight envelope indicates the safe ranges of load factor and airspeeds for the aircraft. It is a combination of the gust envelope and the manoeuvring envelope, with specific requirements given for gust loads at various airspeeds. The requirements for manoeuvring are that the aircraft must withstand both positive and negative limit loads up to dive speed. The gust requirements state that the aircraft must withstand a ±50fps gust at cruise speed and a ±25fps gust at dive speed.

Resulting values

The following results are obtained when feeding the aircraft parameters into the equations and requirements given in the discussed paragraphs of CS23. Distinction will be made between cruise and loiter configurations (wings retracted and extended), as results are almost exclusively affected by wing area and aspect ratio.

Several conflicting requirements arise for the loiter configuration if the design loiter speed of 55km/h (15.4m/s) is maintained as cruise speed. Firstly the minimum cruise speed is higher than the design loiter speed. This in turn leads to a large difference for the two

-	Min value (loiter/cruise)	Max value (loiter/cruise)	Exact requirement (loiter/cruise)
V_C	24.8/28.6	$0.9V_H$	30.9 /30.9
V_{Cmin}			24.2 / 28
V_{Fmin}			15.7 / 18.1
V_D	38.6 or 36.4 / 38.6 or 42		
V_{Dmin}			34.2 / 39.5
V_A	19.9 / 23.5	30.9 /30.9	
V_{Amin}			21.4 / 24.7
V_B	20.4 / 29.3	30.9 /30.9	

Table 2.5: values for V speeds in m/s

definitions of minimum dive speed. Also the manoeuvre speed has some difficult extremes; the minimum value exceeds the maximum. The two definitions for minimum cruise speed are similar, but both are greater than the design loiter speed. This is due to the low airspeed chosen during loiter, and because the specifications merely define cruise speed as the speed at which the aircraft is able to structurally withstand a 25fps gust. When the 110km/h (30.9m/s) cruise speed is taken for both configurations, the numbers make more sense. The obtained values for the cruise configuration show no contradictions and comply well with the design requirements. An overview of the allowed speed ranges for various V-speeds is shown in figure 2.2

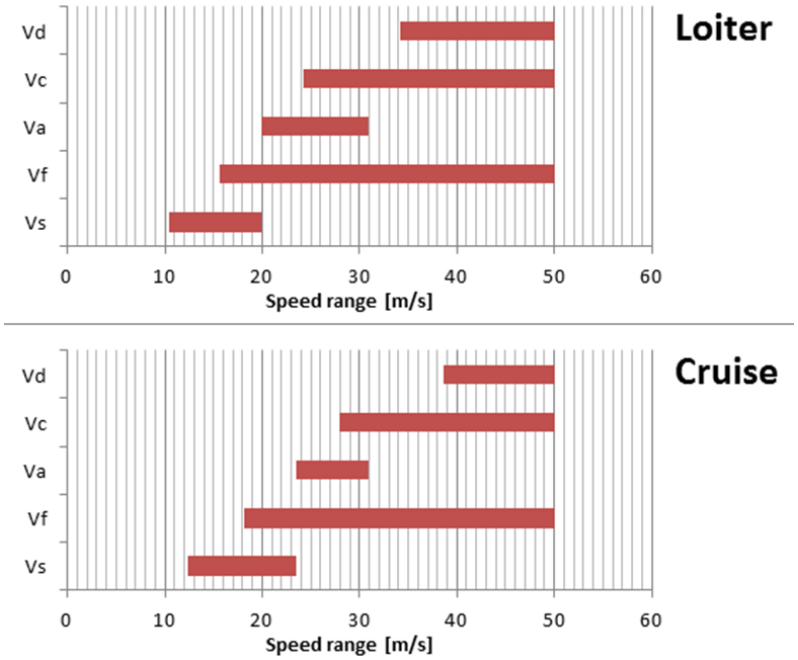

Figure 2.2: The speed range allowed for both configurations assuming 110km/h cruise speed.

The load factors due to gusts can also be computed using these speeds, which combined with the stall speed line and ultimate load lines create the outlines of the load diagram.

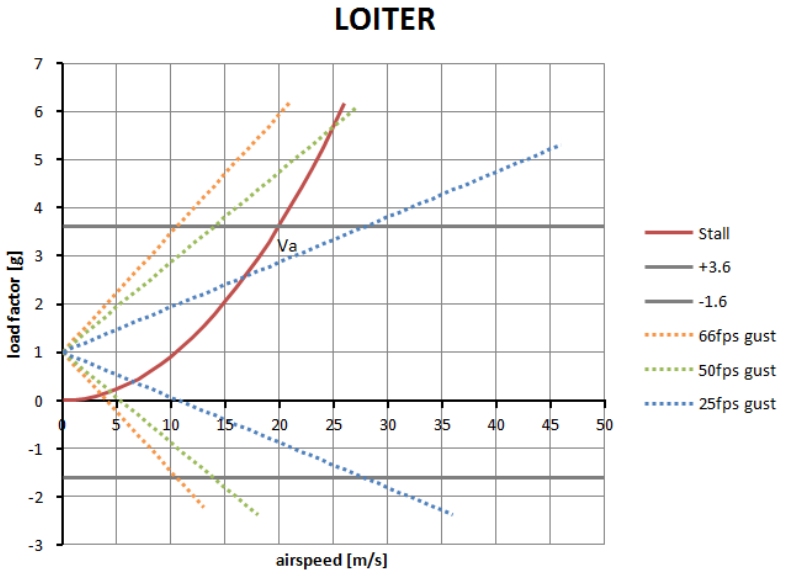

Figure 2.3: The gust loads encountered in the loiter configuration showing that the stall line intersects the 50fps gust line at approximately 5.5g.

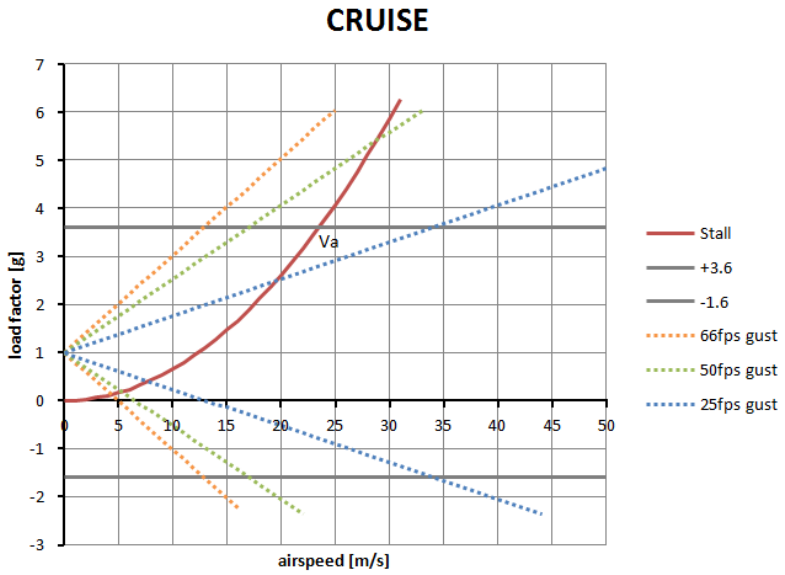

Figure 2.4: The gust loads encountered in the cruise configuration.

Figures 2.3 and 2.4 show the resulting load diagrams for both configurations. The negative stall limit line is omitted due to the unavailability of data on the maximum lift coefficients at negative angles of attack. The first thing that becomes apparent is that the 66fps gust loading is way beyond the stall limit for the greatest part of the speed range (though utility class aircraft do not need to comply with requirements involving 66fps gusts). The 50fps gust requirement at cruise speed would require ultimate loads in excess of +5.5 and -3.5 for the cruise configuration and in excess of +6.5 for the loiter configuration. The speed where the 25fps gust line reaches the ultimate load value would

mark the dive speed for the aircraft. For both configurations this speed is too low to comply with the requirements set in CS23.335. The manoeuvre speed requirements are just met, but would allow for a larger margin if the ultimate load were to be increased. In order to satisfy the dive speed, manoeuvre speed, and cruise speed gust requirements, the ultimate load must be raised to +5.6 -3.6 for the cruise configuration and +6.6 -4.7 for the loiter configuration. This is of course assuming that the loiter wing must meet the same cruise speed requirements as the cruise wing. The only reason assuming a 30m/s (110km/h) cruise speed for the loiter wing was because the specifications do not allow it to be below the stall speed for an ultimate load manoeuvre.

2.3.2 Conclusions

It seems that the assumptions made for the speed requirements for CS23 aircraft become increasingly erroneous for small scale aircraft with low wing loading. Though adequate values exist for all the specified V-speeds if the cruise speed is maintained higher than intended, the subsequent gust loads at this speed become excessively high. Also the assumption that gusts have smaller diameters when encountered by small planes seems slightly out of touch with reality. A more pragmatic set of specifications can be found in CS22 for sailplanes and motor gliders, where the gust load requirements have been reduced to 15m/s at manoeuvre speed and 7.5m/s at dive speed. The concept of cruise speed is also abandoned. The limit manoeuvring load factor is however increased, to a minimum of +5.3 -2.6.

The practical information learned from this is that if one wishes to maintain CS23 standards for the cruise wing, the ultimate load must be increased to +5.6 and -3.6. This would provide a safer margin of operation (as well as making the aircraft less prone to damage in ground handling). It is the authors opinion that these new requirements be applied to cruise configuration only. The loiter configurations may maintain the previous +3.6 -1.6 limits. This can be justified by restricting the speed with extended wingtips to below the manoeuvre speed of 20m/s, where the loads are limited aerodynamically. This would result in the values found in table 2.6. A limit load factor of +5.6 is therefore maintained for all components in this design.

Configuration	Loiter	Cruise
Limit load	+3.6 -1.6	+5.6 -3.6
1g Stall speed	10 m/s	12 m/s
Manoeuver speed	(25 m/s)	29 m/s
Dive speed	20m/s	tbd
Design speed	55km/h (15.3m/s)	110km/h (31m/s)

Table 2.6: Suggested values for both airfraft configurations

Chapter 3

Concepts and Trade-off

Several concepts can be considered for application in the CHANGE aerodynamic wing design, which requires both seamless camber morphing and wing twist, as well as seamless wing extension. The concepts described here satisfy the requirements for twist and camber. From the requirements listed in table 2.2, the largest twist angle over the entire wing occurs in the landing configuration where the root has an incidence of $+2\,^\circ$ and the tip $-3.6\,^\circ$. The camber is either 6% or 2% depending on the configuration, and remains constant over the entire span except at the very tip where a symmetric airfoil is applied to reduce induced drag.

If the design goal of nonlinear twist and camber is to be met, then the skin needs to comply to shear strains which practically eliminate a rigid skin structure. Therefore initial solutions were sought using distributed compliance structures. This increase in flexibility however requires adding stiffening structures to the wing in the form of a spar or wingbox.

Concepts are first introduced in a basic form and then worked out in more detail and applied to the specific CHANGE design case. This allows a trade off to be made to decide which concept is developed into a detailed design.

The requirement of incorporating a telescopic span extension system was enforced, and evaluation of the preliminary concepts led to the decision of using a rigid wing box system. At this stage wing box was sized at 40% chord in order to accommodate the telescopic wing extensions. This leaves the morphing leading and trailing edges with each 30% of the chord. Figure 3.1 shows an embodiment of this concept. The wing extension is 500m long.

3.1 Spar Detailed Concepts

A few excursive designs were evaluated which would also satisfy the principal requirements set for the wingbox while offering either more simplicity or better morphing capabilities.

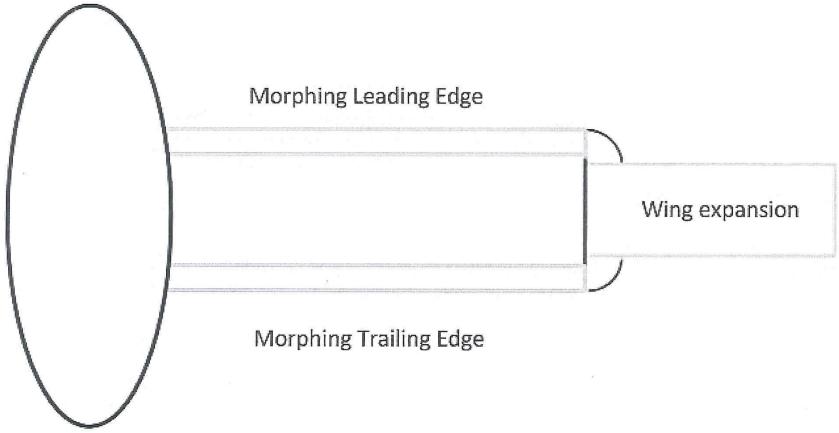

Figure 3.1: The wing spar and control surface layout to be used as agreed by UBI and TUDelft.

A W-shaped wingbox is introduced, but will be omitted in the trade off as it can not accommodate the telescopic extension. This leaves four concepts which can incorporate a span extension system: the axis spar, the rigid wingbox, a tapered rigid wingbox for increased morphing surface, and a concept from UBI which leaves room for a full chord extension.

3.1.1 Axis Spar

In order to achieve a specific twist angle at any spanwise location, each section must be allowed to rotate freely around a central torsionally stiff spar. This is shown in figure 3.2, with a cambered and twisted airfoil as an example deformation.

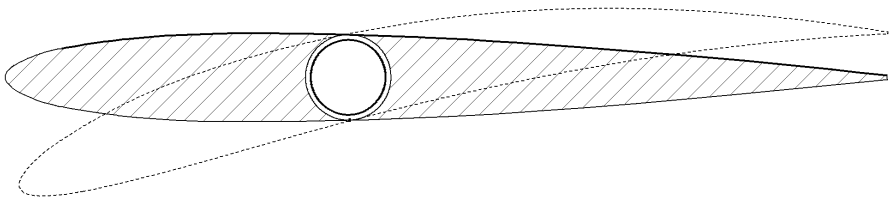

Figure 3.2: The axis spar concept.

Though this requires the spar to be designed to fit within the confines of a round tube, it offers the greatest freedom in combinations of camber and twist. Another drawback is the requirement for several actuators to be distributed over the wing which adds to complexity, however as each actuator only transfers the moment load of a small spanwise section they can be kept relatively lightweight.

The axis spar concept can be adapted to include room for storing the undeployed wing extension provided the axis passes outside the middle 40% of the chord provided to house it and its mechanism. locating the spar in front of this area is the optimal location, as it is quite near to the thickest part of the airfoil. Placing the spar at this forward location deteriorates the morphing capacity of the leading edge, but the narrow depth of the spar

allows for more overall adaptability over the entire airfoil. When combined with flexible skin morphing surfaces, this should provide full nonlinear morphing capability near the root, while still maintaining fair adaptability at the trailing edge of the section which houses the wing extension. The concept is illustrated in figure 3.3. The sketch shows the spar in a red color and the extension is to be housed within the dark blue volume. All other areas can be used as morphing surfaces.

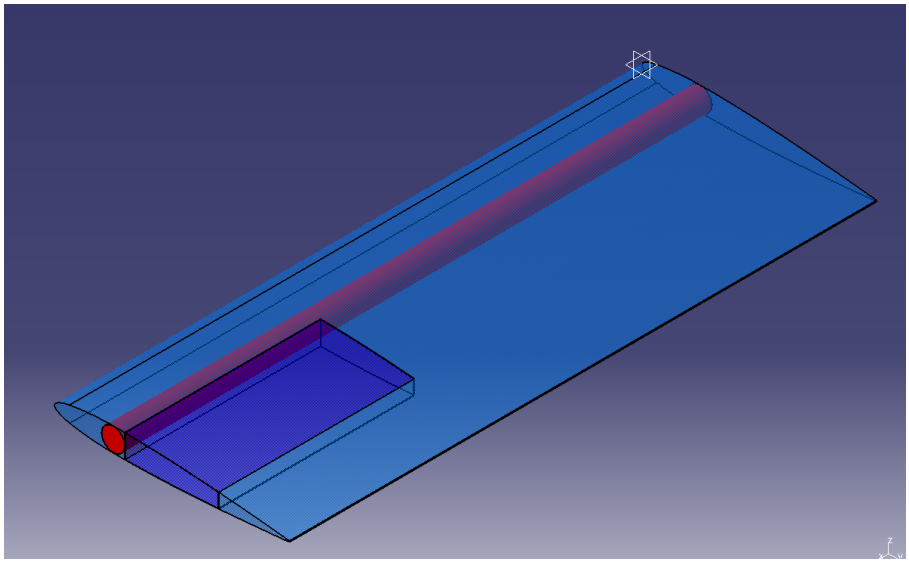

Figure 3.3: A detail concept sketch of the axis spar, showing the volume provided for housing the wing extension. The tip of the semi span is oriented towards the bottom left corner of the image.

There are some disadvantages to this system, the mechanism of the wing extension system is as of yet unknown, so no evaluation can be made of how much room needs to be reserved inboard from the housing area. This makes it difficult to allocate space to the different parties involved in the design. Another uncertainty is in the load transfer from the wing extension to the round spar, which increases the overall complexity of the design.

3.1.2 Rigid Wingbox

Another solution is to add a conventional torsionally stiff wingbox to the wing. This restricts a pure twist actuation and adds a stiff section in which the camber cannot change, but is by far the simplest option.

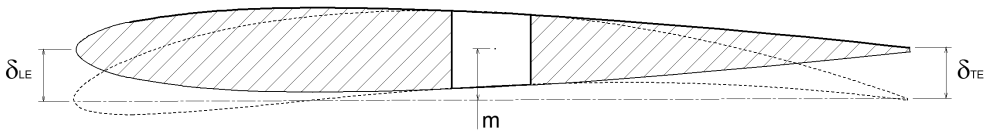

Figure 3.4: The stiff wingbox concept.

Shown in figure 3.4 is the concept applied to a NACA0010 airfoil, the dotted outline shows the same airfoil cambered to 6%, effectively mimicking a NACA6510. If the fidelity

of the airfoil may be traded off in favour of wing twist, then a differential deflection of the leading edge and trailing edge can replicate this function. The following equations approximate the twist and camber obtained for any deflection of the leading and trailing edges:

$$\alpha_t \approx \sin \alpha_t = \frac{\delta_{TE} - \delta_{LE}}{c} \tag{3.1}$$

$$m = \frac{\delta_{TE} + \delta_{LE}}{2c} \tag{3.2}$$

This set can be solved for the deflection in function of required camber and twist:

$$\delta_{TE} = c\left(m + \frac{\alpha_t}{2}\right) \tag{3.3}$$

$$\delta_{LE} = c\left(m - \frac{\alpha_t}{2}\right) \tag{3.4}$$

Where c is the airfoil chord, m is the camber relative to the chord, and δ are the absolute deflections at the leading and trailing edges. The twist angle α_t is in radians.

In order to obtain a camber of 6% with a twist of $+2\,^\circ$ the deflections must be 46.47mm and 25.52mm downwards for the trailing and leading edge respectively, which for a 600mm chord length is not beyond practicality.

This concept with a simple rigid wingbox of constant dimensions over the entire span is applied to the requirements set by the CHANGE targets. It allows 30% of the chord at the leading edge and 30% of the chord at the trailing edge to approximate the target twist and camber. The wingbox has a constant width of 40% of the chord all the way to the tip, these values have been determined in concord with the other partners involved in the design. Simplicity is key here, all morphing surfaces are straight, which is expected to simplify their design. However this simplicity is achieved at the expense of reduced adaptability, as the wingbox creates a relatively large section in the middle of the airfoil which cannot change shape. Figure 3.5 shows this concept applied to a semi-span section of the wing.

3.1.3 Tapered Rigid Wingbox

The shortcomings of the rigid winbox in terms of limited morphing surface can be reduced by decreasing the size of the wingbox near the root. This does not necessarily have to adversely affect the structure of the wing, as the size of the wingbox is driven by the chord

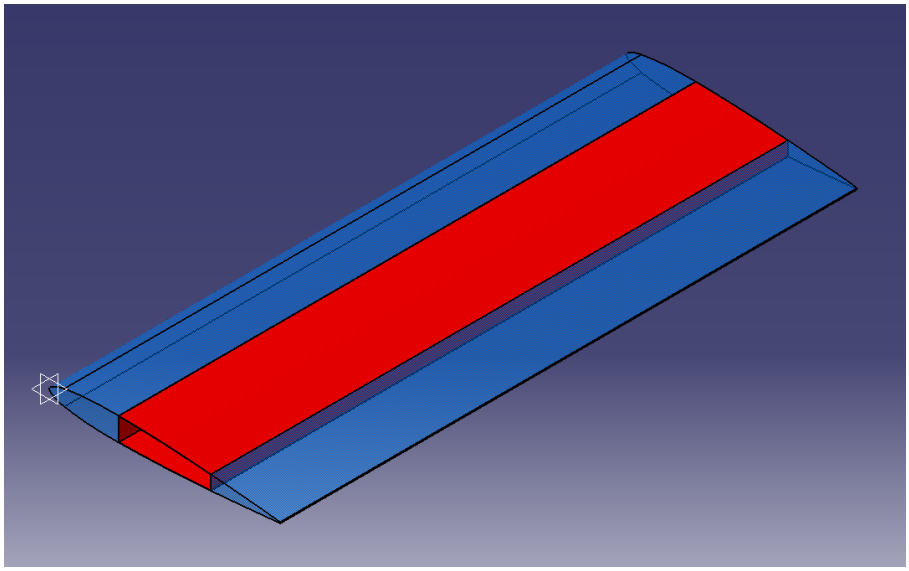

Figure 3.5: A detail concept sketch of the rigid wingbox. The tip of the semi span is oriented towards the bottom left corner of the image.

length made available for the wing extension. As this extension only consists of a 500mm stub, the wingbox inward of this point can be made smaller. This leaves more area for adaptive surfaces, however the nature of these will have to be more complex as these no longer have uniform chordwise dimensions. The concept is shown in figure 3.6. Accurate sizing of the inboard wingbox does however require knowledge of the span extension mechanism which was not known at this point in the design.

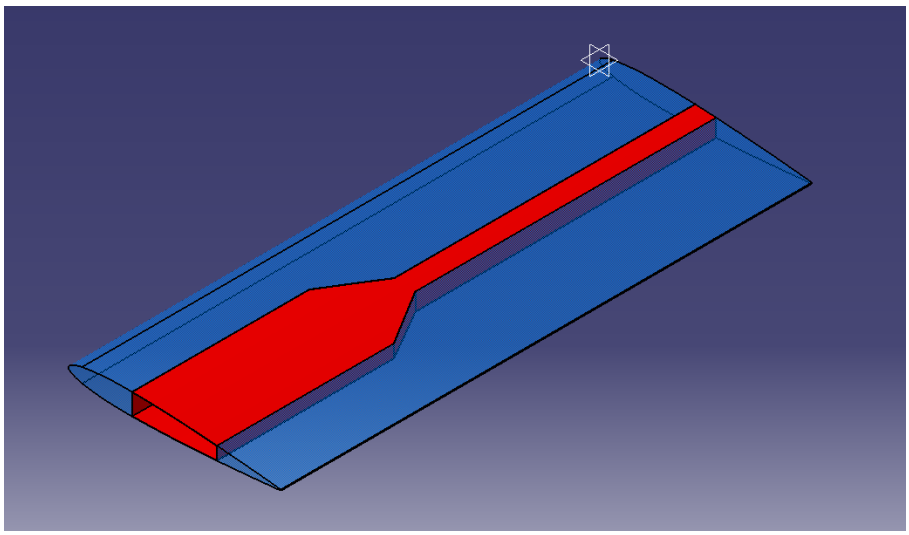

Figure 3.6: A detail concept sketch of the Tapered wingbox. The tip of the semi span is oriented towards the bottom left corner of the image.

3.1.4 UBI Concept

If a full chord span extension is required, then the volume available for stowage must be adapted accordingly. This does however limit the adaptability in the outer 500mm of the wing. Such layout is presented in figure 3.7.

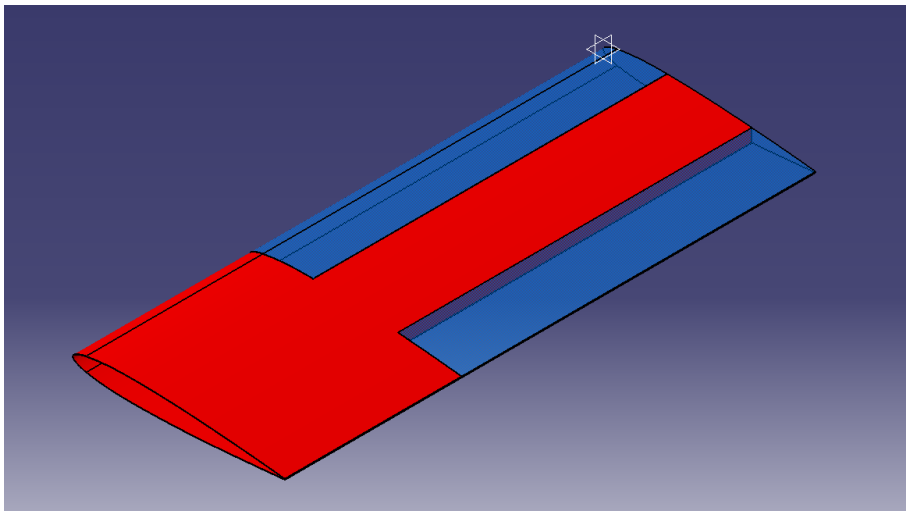

Figure 3.7: A detail concept sketch of a wingbox allowing for full chord wing extensions. The tip of the semi span is oriented towards the bottom left corner of the image.

This leaves very little adaptive surface on the main wing, but allows for full chord wing extensions without the need for expandable structures. More surface area can thus be made available for adaptive mechanisms on the wing extensions themselves. The adaptive leading and trailing edges on the main wing also have a simple constant chord dimension similar to the rigid spar concept, they are merely shorter in the span direction.

3.1.5 W-Shaped Wingbox

Some shortcomings of the stiff square wingbox concept may be overcome by a twist actuated W-shaped wingbox as shown in figure 3.8.

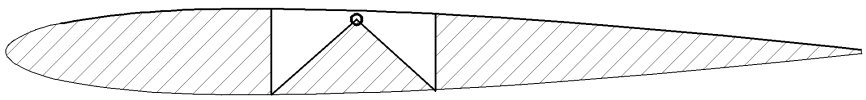

Figure 3.8: W-shaped wingbox with a sliding joint where the two diagonal flanges meet.

This feature adds adaptability to the otherwise rigid wingbox and allows the lower airfoil surface to contract and better approximate a cambered airfoil. A spanwise sliding joint in the middle of the wigbox allows an actuator to introduce shear strain in the box, thus causing the wing to twist. This adds the freedom of independent actuation of camber and twist, but the concept remains limited to a constant twist rate over the entire wing. For a thin walled open section such as the spar it can be assumed that the torsional stiffness is negligible compared to the aerodynamic loads and the rigidity of the surrounding

compliant structures, so actuation loads will be largely dependent on the latter. Placing the sliding joint near the shear centre of the spar will prevent shear forces due to wing bending to load the actuating mechanism. This concept offers a great flexibility in airfoil morphing but it cannot accomodate the span extension mechanism, so it is not developed further.

3.1.6 Trade-Off

The concepts are evaluated by four properties: adaptability, weight, complexity and modularity. Adaptability is measured by the fraction of the total morphing surface area (relative to the cruise condition wing surface) allowed by the concept. This value is scaled such that a score of 1 is given to the concept deemed lightest. Adaptability is estimated as a value from 0 to 1 based on the total adaptive surface area. Complexity is also estimated subjectively with the simplest concept being given a score of 1. Modularity is a binary value, this can be either one or zero, based on whether a morphing system matching the spar arrangement can be fitted to any other wing type.

The spars can be traded off using a simple trade off table in which these four qualities are weighted equally. An overview of the trade off is given in table 3.1.

The advantage of the axis spar when it comes to adaptability becomes clear in the trade off table, this concept should allow up to 85% of the planform surface to alter its camber and twist. This large surface is likely to come with a weight penalty though, an additional disadvantage of 10% was added to the score to account for a more complex load transfer from the span extension to the tubular main spar. Furthermore, this concept can not be considered modular as the deforming mechanism must be tailored to match the exact properties and requirements of the wing shape. Overall this design scores fairly low, and this does reflect the technically ambitious requirements which are needed to make this concept work.

The rigid spar comes out fairly low on the adaptability score, with only 60% of its absolute surface area available for morphing, but this is made up by a more positive mark on the weight estimate. The results also reflect that this shares a top place for the most simple solution. This simplicity also manifests itself in the straight and uniform shape of the morphing surfaces, which show potential for a modular design solution. One disadvantage is that the limitation imposed on the dimensions of the span extension due to the small storage area inside by the narrow wingbox will require a more complex outer wing design.

The latter limitation is remedied in the UBI concept, though at the expense of the adaptive surface score, as *only* 40% of the total wing surface (with extensions retracted) is adaptive. The rigid section left in the middle of the semi span (shown in figure 4.5) when the wings are fully extended also limits the possibility to adapt the lift distribution in all flight conditions.

The tapered spar is estimated to fall somewhere in between the axis spar and the rigid spar when it comes to the adaptive surface area, a value of 70% was used in the trade off. Structurally this concept was not given any weight penalties other than those caused by the larger morphing surface area. The tapered and irregular nature of the remaining surfaces do however require a design approach which is not expected to yield a modular result.

	Axis	Rigid	Tapered	UBI
Adaptability	1,00	0,71	0,82	0,47
Weight	0,59	0,83	0,77	1,00
Complexity	0,40	1,00	0,70	1,00
Modularity	0,00	1,00	0,00	1,00
TOTAL	1,99	3,54	2,29	3,47

Table 3.1: Trade off for the spar configuration

The results of this points towards the Rigid concept and UBI spar concepts as very close competitors. However, the use of the rigid spar concept hinges on the development of the expandable airfoil, whereas the UBI concept can be used in combination with any type of wing expansion. Both the UBI concept and the rigid spar concept have rectangular morphing surface areas, so a morphing system may very well be found which can be applied to both spar arrangements. A sensible conclusion would be to go for the UBI concept, while maintaining the possibility of extending the adaptive region to the tip of the cruise wing should suitable chord expansion technology become available. The same conclusion was made independently at a higher level in the project.

3.2 Morphing Detailed Concepts

Various concepts for the morphing surfaces have been worked out for this project. These concepts include rigid skin systems as well as flexible skin systems. Some expanding/inflatable concepts are also proposed for use on the wing extensions. These concepts are described in detail, after which a trade off is performed to select the most adequate system for this particular application.

3.2.1 'Conventional' Mechanism

This is a conventional kinematic mechanism which forms a rigid skeletal system to support a flexible skin. This type of morphing uses a flexible skin which is shaped by some type of load bearing structure. The skin therefore does not add to the rigidity and merely serves the purpose of creating a smooth aerodynamic surface. Advantages of this method would be more flexibility in what shapes can be created, at the expense of more complex actuation mechanisms required to create these. Such systems have been successfully applied in other experimental structures [25] [12]. Figure 3.9 shows a generic mechanical morphing system applied to a CHANGE wing section.

Placing several mechanisms along the span would allow this system to produce nonlinear deformations. An obvious drawback of this system is the large number of required parts and its design complexity. The skin material to be used for this concept is fibre reinforced EPDM (ethylene propylene diene monomer), which was proposed by one of the project partners. EPDM is an elastomer with an elongation at break of over 300% [13]. The mechanism can be manufactured from either aluminium or polymer depending on the internal strength requirements.

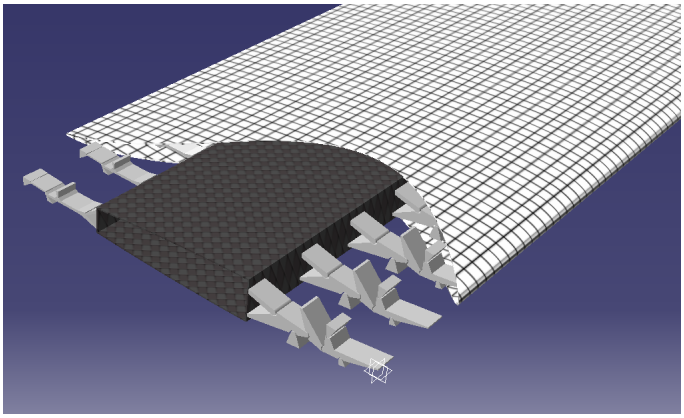

Figure 3.9: The mechanical morphing concept.

3.2.2 Distributed Compliance

Distributed compliance is a term used to describe flexible systems which are topologically formed to deform elastically in a predetermined way. It distinguishes itself from mechanisms by the property that a compliant structure does not contain hinges but instead relies on small strains throughout the structure to achieve a large overall deformation [11]. Such structures have the advantage of containing significantly fewer discrete parts, but rather one large complex part, which can be either an advantage or a disadvantage depending on the manufacturing process. For this project a concept involving a tailored EPP structure is proposed, as illustrated in figure 3.10.

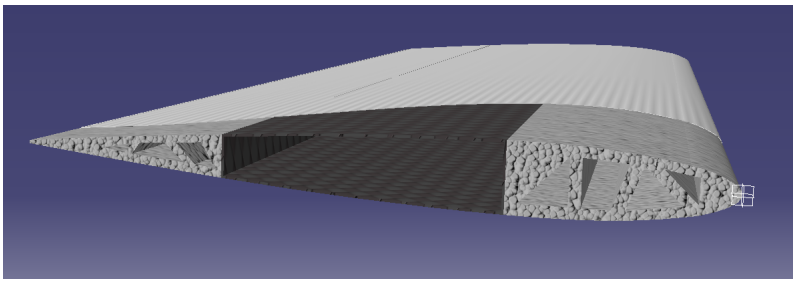

Figure 3.10: A proposed embodiment of the distributed compliance morphing concept.

EPP (expanded polypropylene) is a flexible foam material which can be cut from a block in any shape using a computer numerical control (CNC) hot wire cutter. This allows complex topologies to be manufactured relatively easily from bulk material. Disadvantages are that the low stiffness of the EPP material limits the ability to retain its shape in high wing loading applications.

3.2.3 Slotted Skin

This concept is inspired by a mechanism by Vos et al. [28] but is modified to include a camber mechanism. The defining feature of this concept is that the skin is stressed and does not require a support structure. This would allow for a more simple and lightweight

structure, though the variety of shapes that could be achieved may be limited, as the shearing required for complex double curved deformations requires a greater force and might cause excessive strain in the material.

A more rigid skin structure has the benefit of needing little to no internal support structure, which leaves ample volume for actuators to be placed inside the leading and trailing edge area itself. The slotted skin approach also has potential for greatly reducing the required number of moving parts, as in a way this also uses the principle of distributed compliance, the difference being that the load bearing structure is integrated into the skin and that a hinge is formed by the upper skin near the spar. This does impose limitations on the adaptability of the wing: deformations which require in-plane strain of the skin would impose inhibitive strength requirements on the actuation system. This rules out non-linear twist and camber distributions. The layout is shown in figure 3.11. The material deemed most suitable for this application is glass or carbon fibre reinforced epoxy. This is thought to be able to provide sufficient structural rigidity while retaining a deformable thin walled skin.

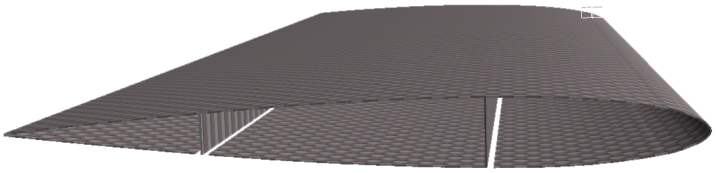

Figure 3.11: The slotted skin morphing concept

The skin of the lower surface of both the leading and trailing edge is interrupted along a slot near the spar. The airfoil can contract and expand along this slot, causing a deformation in camber. Twist is achieved by differential actuation along the span. A simple cardboard and EPP mockup has determined that this differential camber actuation is coupled to a spanwise sliding motion, so this also needs to be accommodated. Figure 3.11 also shows a slot in the wingbox, which allows the wingbox to be twisted as well.

3.2.4 Inflatable Attached Skin

In order to significantly increase the wing area by means of telescopic wing extensions, the chord of these must be maximized. As a large part of the wing might be taken up by morphing mechanisms, it makes sense to minimize the dead space taken up by stowed wing extensions. A possible solution to this might be an inflatable or telescopic leading edge.

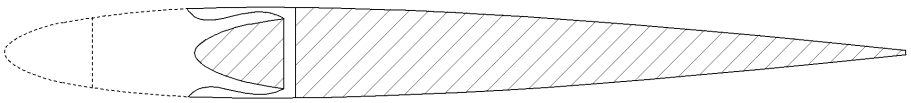

Figure 3.12: Extending leading edge concept.

Figure 3.12 depicts a configuration where this is applied to a NACA0010 airfoil, which shows the potential to reduce the chord by up to 20%. This may be further increased by applying a similar mechanism to the trailing edge. Obvious drawbacks include the complexity of the required actuation mechanisms, which is further increased when combined with camber and twist morphing.

Inflatable wing structures in particular have been considered for the wing extensions. A full literature review on the topic has revealed no suitable existing systems which can be both deployed and retracted in flight. This has not deterred the author to come up with some ideas of his own. The proposed concepts rely on open cell polyurethane foam covered with a flexible impermeable skin. The open cell foam maintains a distributed load on the skin to keep the inflation pressure from deforming it. Figures 3.13 and 3.14 show this idea when applied to the CHANGE wing.

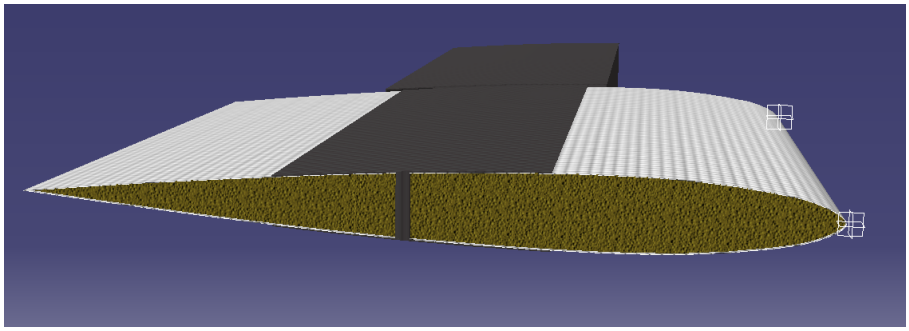

Figure 3.13: An inflatable wing extension with a solid core

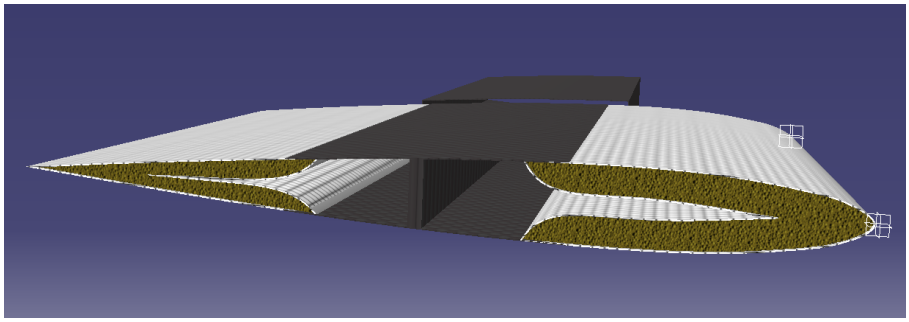

Figure 3.14: An inflatable wing extension with a hollow core

The solid core requires a skin which does not attach directly to the top flange of the I beam spar. This allows the foam to crush into the area between the flanges, but it also leaves a small front facing step in the airfoil.

The skin can be made flush with the flange if material is removed from the core to allow the resulting inflatable sandwich to fold inward. This hollow core concept does require a second skin to be attached to the inner surface to counter the out of plane bending moment caused by the internal pressure. Without this, the skin will simply bulge out into a cylindrical shape.

3.2.5 'Inflatable' Detached Skin

The use of open cell foam can also be developed into a detached skin concept where the skin is used for both actuating and deploying the airfoil. An impression of this can be found in figure 3.15.

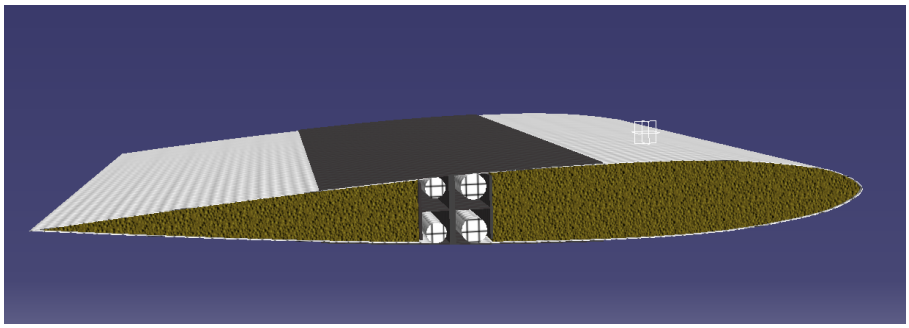

Figure 3.15: An open cell foam core where the skin is used for both deploying and actuating the airfoil

The skin is wrapped around the airfoil and connected to a winch mechanism which can pull the airfoil inwards. Camber can be modified by retracting the bottom skin more than the top skin. This is not a pressurized inflatable system, so no pressurisation system is required.

A mockup of this concept was built, which revealed that quite large camber deflections can be achieved, though the skin separates from the core over any resulting concave contour. This is shown in figure 3.16.

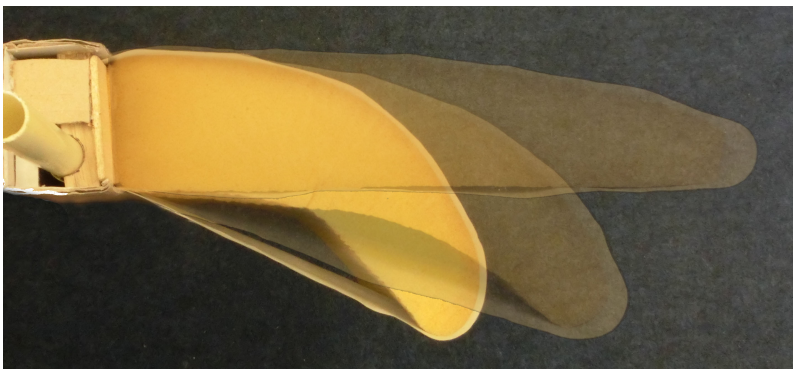

Figure 3.16: A mockup showing an extreme deflection and the resulting concave contour.

The limitations of this concept are its inability to achieve twist morphing, and the complexity of the winch system which has to accurately actuate four spools separately. The mockup also showed a high degree of flexibility which shows that this does not lend itself to aircraft with high wing loadings, though this can be improved by using stiffer foam. The mockup uses a polyurethane foam core and a glassfibre reinforced neoprene skin.

3.2.6 Trade-Off

The morphing mechanism was selected on the basis of the project requirement for a novel method of actuation. A significant amount of prior work can be found on the subjects of mechanical morphing and even distributed compliance morphing wings. Therefore the field is narrowed down to just the slotted skin system. The idea of inflatable airfoils was also to be pursued further time permitting, though priority was given to the slotted skin concept as main focus. This decision can be supported by a trade off which evaluates the relative adaptability, weight, and complexity of each concept.

The adaptability score is based on the nature of the deformations which are expected to be achievable using the proposed concepts, multiplied by the surface area it makes available for morphing. A distinction is made between linear and nonlinear twist and camber distributions. Both the mechanical and distributed compliance concepts are given a absolute score of 1 for adaptability, the slotted skin is given a 0.8 to account for the linear limitation of the deformations. The inflatable concepts are given a 1.5 score to account for the fact that using these would result in significant adaptive surface gain on the main wing.

The complexity and weight can only be roughly estimated, but this is sufficient to support a decision regarding what concepts should be developed further. The inflatable and expandable systems were given high weight and complexity penalties because of the unconventional and largely unknown actuation requirements associated with these concepts. This makes them an overall unattractive option. The distributed compliance system is estimated to have a fairly low weight and complexity due to the proposed use of integrally formed expanded polymer foam components. The mechanical system is expected to be more complex and heavy due to its high expected parts count. The slotted skin concept comes out on top due to its simplicity and low expected weight, despite having a considerably lower adaptability both is terms of surface area and the quality of deformation.

	Mech	DC	Slot	Inflatable	Detached
Adaptability	1	1	0.8	1.5	1.5
Relative	0,67	0,67	0,53	1,00	1,00
Weight	0,86	0,86	1,00	0,71	0,71
Complexity	0,88	1,00	1,00	0,50	0,50
TOTAL	2,41	2,53	2,53	2,21	2,21

Table 3.2: Trade off for the morphing mechanism

Chapter 4

Deflections and Reaction Forces

The concept selection process has led to a design using a rigid wingbox combined with adaptive leading and trailing edges which must provide the necessary deformations to comply with the target shapes of the cruise, loiter and take-off configurations. These target shapes are translated into requirements for the deflections which need to be achieved by the adaptive surfaces, and this is in turn used for sizing in the remainder of the design.

4.1 Mechanics of the Concept

This morphing system relies on the torsional flexibility of open thin sections for twist control and camber control. Both twist and camber can be controlled by changing the positions of the extremities of the skin panels.

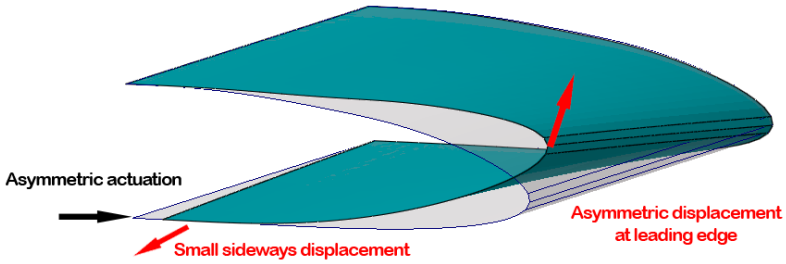

Figure 4.1: Twist morphing of the leading edge, with input actuation and resulting twist deformation at the leading edge. The sideways movement is an effect cased by the twisting of the section.

Figure 4.1 shows the concept applied to the leading edge surface. When one corner is actuated forwards while the other remains fixed, one end of the surface will move up and the other will stay in place, which introduces twist in the surface. This is coupled with a small sideways movement of the lower skin. When both corners are moved forward by the same amount then the leading edge will move up over the entire span, which can be used to reduce the camber of the leading edge. This can be seen in figure 4.2.

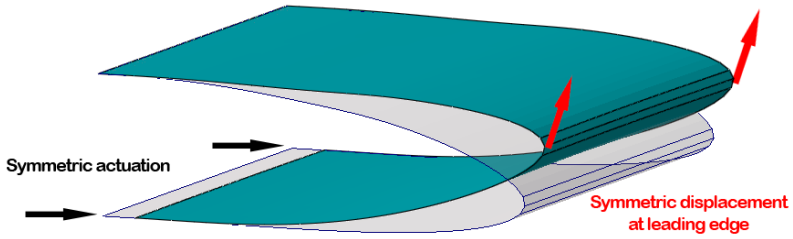

Figure 4.2: Camber morphing of the leading edge surface, showing input actuation and resulting deformation at the leading edge

This principle is also valid for the trailing edge. Figure 4.3 shows how a greater twist can be achieved if both ends are moved in opposite directions, which also results in a sideways movement of the lower skin. The wedge shape of the trailing edge can also be twisted quite easily.

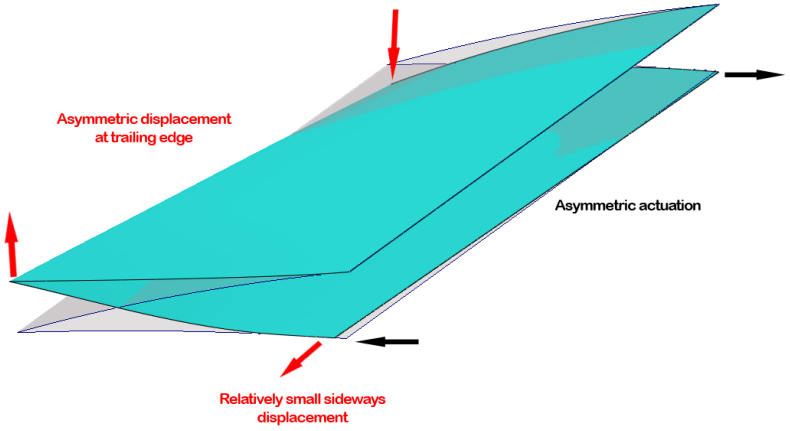

Figure 4.3: Twist morphing of the trailing edge surface, with input actuation and resulting deformation at the trailing edge. The sideways movement is an effect cased by the twisting of the surface.

Figure 4.4 shows camber morphing applied to the trailing edge. Any linear twist and camber distribution can be achieved by a combination of inputs.

The skin must be flexible to limit the force required for actuation, but stiff enough to limit deformation due to aerodynamic loads. Ideally the laminate could be tailored specifically such that the deformed shape matches an optimal aerodynamic shape. However, the time and resources required for such an optimization would exceed the scope of this project. A limited and unpublished analysis has been performed on the topic of skin laminate thickness by another student. The results of this research are the basis of the assumption that the aerodynamic deformation remains acceptable when the leading edge skin in made of a uniform constant thickness 1.5mm quasi-isotropic GFRP prepreg 6 layer laminate. The trailing edge is made of a uniform constant thickness 1mm quasi-isotropic GFRP prepreg 4 layer laminate. The material to be used, Gurit EHG250-68-37 cloth, has been suggested by the CHANGE project partners.

The concept is verified using an ABAQUS simulation model where the lower skin is subjected to a 200N sideways force near the spar, which causes a significant twist de-

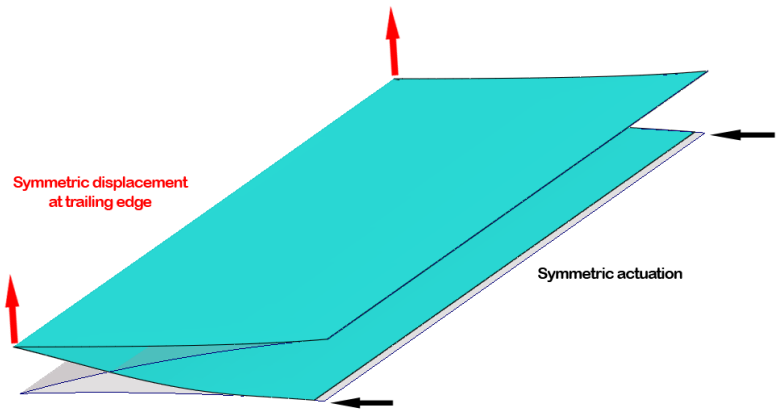

Figure 4.4: Camber morphing of the trailing edge

formation of +/-15mm vertical displacement at the leading edge. If the same force was applied while the edges are constrained from moving forwards to simulate fixed actuators, then this 200N force only causes a +/-1mm displacement. A 48N reaction force is required from the actuators to keep the edges pinned in place. These results imply that merely constraining the chordwise motion of the corners is sufficient to stop the surface from significantly deforming under loads. This has been confirmed qualitatively with simple mockup structures. The ABAQUS model used in the analysis will be discussed in more detail further in this chapter where the calculations for the the elastic loads are presented.

4.2 Undeformed Wing Shape

An undeformed wing shape must be selected which can be adapted to form all required deflections. Continuity of the airfoil must also be taken into account. A list was made of the airfoil properties for all the configurations, which included data on the camber and twist angles at various span locations.

The rigid wingbox is to remain untwisted and has the camber properties of the loiter configuration target shape. The undeformed leading and trailing edge adaptive structures follow this shape, ideally the undeformed assembled wing has zero twist angle and a constant camber of 6% over the entire span with a small symmetric NACA 0010 section at the very tip (for a 4m span case). The adaptive surfaces will thus have a constant NACA 6510 airfoil shape between the root and at the 1m span mark. Due to the high-wing configuration of this aircraft the first 100mm from the root outwards are not to be fitted with adaptive surfaces. Figure 4.5 shows a semi span of the undeformed wing shape with its various components. The rigid wing spar and span extension enclosure are colored red, the adaptive surfaces are blue and the span extensions are orange. This also shows the drastic impact of the span extension system on the overall adaptability of the wing, as the morphing surfaces are now limited to a 900mm section near the root.

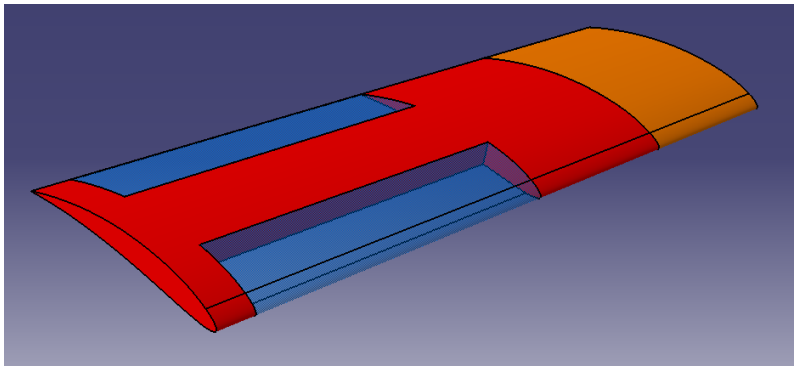

Figure 4.5: The undeformed NACA6510 wing shape semi span with rigid spar (red), adaptive surfaces (blue) and span extensions (orange). The wing root is pointing towards the bottom left

4.3 Required Deflections

The deflections required to achieve the target shape in all configurations can be computed using equations 3.3 and 3.4 as derived in chapter 3. These deflections are based on geometric approximation of the target airfoils, and therefore do not guarantee similar aerodynamic properties. It is recommended that future iterations of the design include verification of the aerodynamic properties of the deformed shapes.

Table 4.1 gives an overview of the deflections needed at both the root and at 1m span for all three configurations. An upwards deflection is defined as positive.

		camber [-]	twist [deg]	LE defl. [mm]	TE defl. [mm]
root	-	0,06	0	0	0
	takeoff	0,03	0,5	20,62	15,38
	cruise	0,02	0,2	25,05	22,95
	loiter	0,06	1,8	9,42	-9,42
1m	-	0,06	0	0	0
	takeoff	0,03	-0,25	16,70	19,31
	cruise	0,02	-0,6	20,86	27,14
	loiter	0,06	0,25	1,31	-1,31

Table 4.1: The deflections required to match the target configurations (upwards positive)

The values for twist and camber were taken from the aerodynamic design reports by ARA[4][5], the target twist distribution is give in figure 2.1.

The deflections needed to match the target configurations are mostly upwards when starting from the undeformed wing shape, which means that the elastic forces caused by the structure are partially cancelled out by the upwards aerodynamic loads on the airfoil. This reduces the magnitude of the forces to be delivered by the actuators. All requirements for twist and camber can be met with a vertical leading edge travel of 0 to 25mm and a trailing edge travel of -9.5 to 27mm. The large deformations required to approximate the NACA 2510 airfoil in the cruise configuration still lead to gaps between the morphing

surfaces and the undeformable sections, but measures can be taken to limit their adverse aerodynamic effects. Similar gaps caused by conventional flaps or ailerons can be faired using aerodynamic fences[21].

The vertical motions of the leading and trailing edges are coupled to the longitudinal motions of the free edges of the surface, as demonstrated in section 4.1. The exact relationship of these displacements was evaluated in an ABAQUS simulation where the upper skin is assumed fully clamped and the lower skin is allowed free translation and rotation in the plane tangent to the skin surface. Several configurations of this constraint were simulated at various locations to evaluate the effect on the quality of the resulting shape and the forces required for actuation. The results of this indicate that greater forces and displacements are required if the lower skin is attached further away from the spar, though it does not vary significantly up to approximately 30mm. The shape of the deformed airfoil is also greatly affected, as can be seen in figure 4.6.

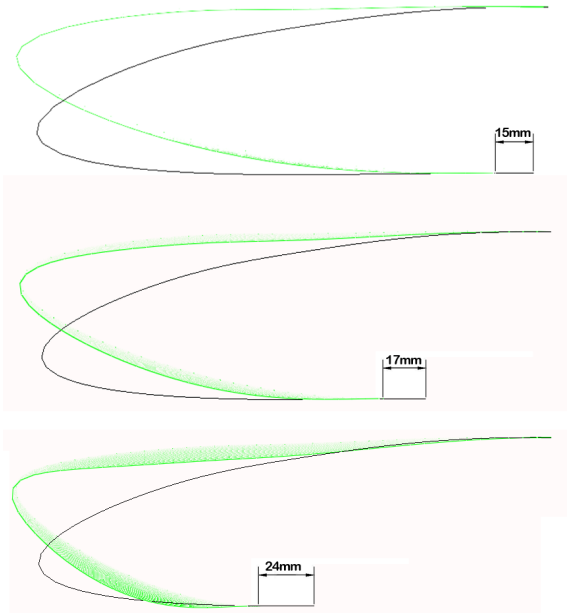

Figure 4.6: The deformation of the leading edge when the bottom skin is guided at the spar (top), 40mm forward of the spar (middle), and at 80mm forward of the spar (bottom). All have a 27mm upward displacement of the leading edge, which requires 15mm, 17mm and 24mm of actuation respectively.

The guide distance of the leading and trailing edge was set at 30mm on the basis of these results. Further ABAQUS analysis reveals that the relation between vertical displacement and horizontal actuation travel is almost completely linear. As shown in figures 4.7 and 4.8

This upwards/forwards coupling analysis is performed for the leading and trailing edges at various relative tip and root displacements. A symmetric case is considered where both tip and root are moved in the same direction, as is an asymmetric case where the tip is actuated and the root remains pinned. The results allow the estimation of the input travel needed to meet all deformation requirements, these are summarized in table 4.2.

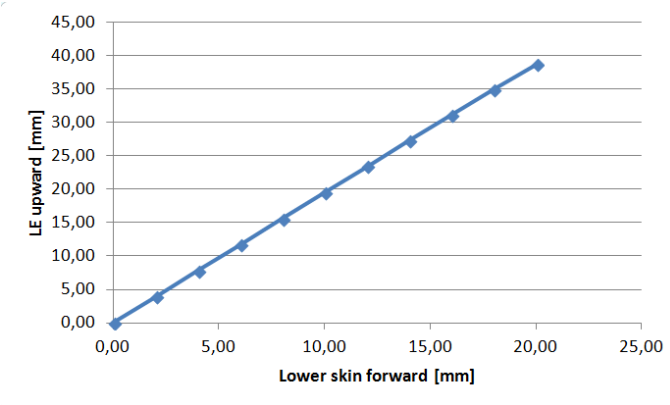

Figure 4.7: The vertical travel of the leading edge in function of the lower skin actuation.

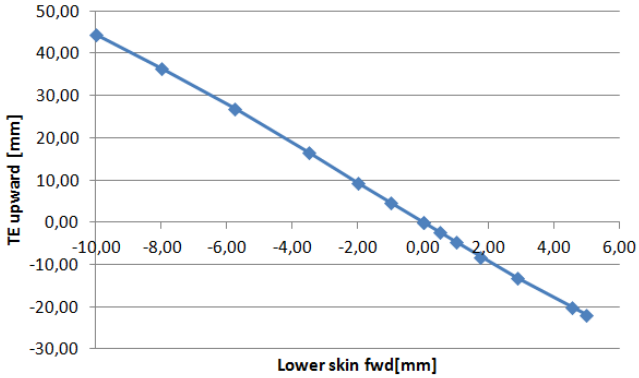

Figure 4.8: The vertical travel of the trailing edge in function of the lower skin actuation.

		LE [mm]	TE [mm]
root	-	0	0
	takeoff	10,68	-3,50
	cruise	12,98	-5,21
	loiter	4,88	2,14
1m	-	0	0
	takeoff	8,65	-4,39
	cruise	10,81	-6,17
	loiter	0,68	0,30

Table 4.2: The input travel required to match the target configurations (forward positive)

The extremes of the required input travel for the leading and trailing edge are +13/-0mm and +2.1/-6.2mm respectively. The maximum sideways travel of the lower skin is encountered when both inputs are at opposing extremes. This is 1.7mm for the trailing edge surface and 3.5mm for the leading edge surface. The nature of the deformation is depicted in figure 4.9, where the extreme deformations of the skin are superimposed with the target airfoils. This shows how these airfoils are merely approximated by matching

the positions of the leading and trailing edges, and are very unlikely to match their aerodynamic properties. The figure does not show the rotation of the airfoils and the maximum camber of two target airfoils do not coincide, which makes it appear as if the travel envelope of the deformation is greater than necessary.

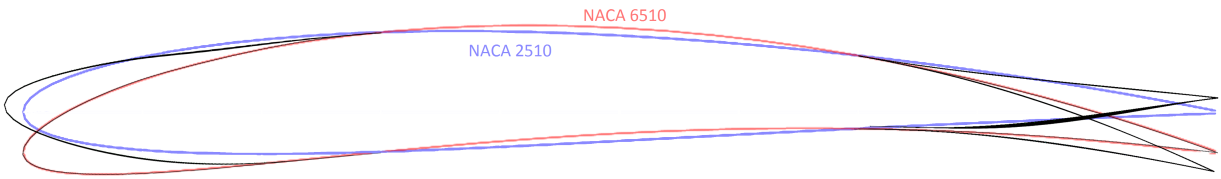

Figure 4.9: The shapes of the wing skin in its extreme positions. The target airfoils are superimposed in red (NACA 6510) and blue (NACA2510). The lines in black represent the extreme positions of the deformed wing skin.

Allowable freeplay or backlash determines the accuracy with which the surfaces must be actuated to limit flutter. Civil Aeronautics Administration guidelines for personal type aircraft are used to establish limits on actuation freeplay. For ailerons the total free play may not exceed 2.5% of the aileron chord aft of the hinge line [17]. This translates to a 4.5mm vertical play at the leading and trailing edges. The actuation must therefore have no more that 2.3mm freeplay at the leading edge and no more than 1mm at the trailing edge.

4.4 Actuation and Support Force

The sizing and structural design of the mechanism connecting the spar with the lower skin relies on an accurate estimation of the reaction forces which it must carry to the main spar. These forces consist mainly of elastic forces caused by the deformation of the morphing surface, and aerodynamic loads caused by the lift and drag effects.

4.4.1 Aerodynamic Loads

The aerodynamic loads on the trailing edge structure can be modeled as rigid body simply supported at two points where the skin joins the spar. A schematic representation of the loads on the trailing edge surface is given in figure 4.10. Deformations caused by these aerodynamic loads are assumed to be small, so no significant reaction moment is expected in the skin itself, and the vertical reaction forces are assumed to have the same magnitude.

The vertical reaction forces are each half of the lift load over the surface, while the horizontal forces are a couple which counters the bending moment. Both can be calculated from the lift distribution over the chord, which has been numerically calculated in the ARA aerodynamics report [5].

The pressure coefficient distribution is used to obtain a chordwise shear and bending plot for the NACA6510 airfoil at the highest analyzed angle of attack. This gives an indication of the forces that can be expected under operating conditions, as the highest wing loading

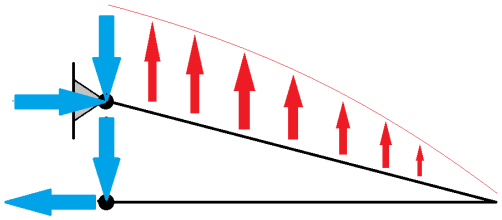

Figure 4.10: A schematic indicating the loads (red) and reaction forces (blue) on a trailing edge surface.

is likely to occur near stall angle, a high angle of attack is selected. This also corresponds to the largest leading edge actuator force due to the increased suction peak at the front of the airfoil. The values for shear and moment are still a function of free stream dynamic pressure, which allows to scale the forces for higher load factors by increasing the free stream velocity. The section lift coefficient will however remain the same, and equals 1.148.

A chordwise numerical integration of the pressure distribution yields the moment and shear distributions of figures 4.12 and 4.11. The somewhat unusual units of the values indicate a 1Nm bending moment per meter of span per N/m^2 of dynamic pressure. For the shear force this is a 1N force per meter of span per N/m^2 of dynamic pressure. The curves represent the internal moment and shear forces in the airfoil if it were a slender beam clamped at either the leading or trailing edge.

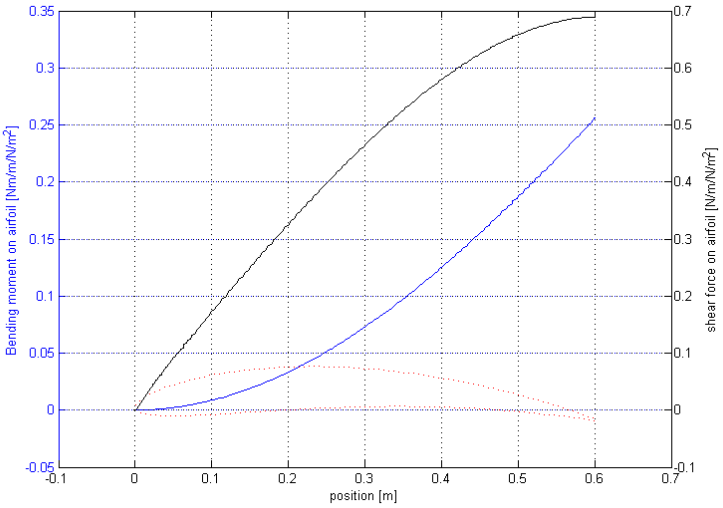

Figure 4.11: Shear and moment distribution around the trailing edge, NACA6510 $C_l = 1.148$.

A dynamic pressure of $664N/m^2$ is required to perform a 5.6g manoeuvre with a 3m span wing and a C_L of 1.148. This corresponds to an equivalent airspeed of 33m/s which is beyond the manoeuvre speed, so the load factor is not limited by stall but rather by

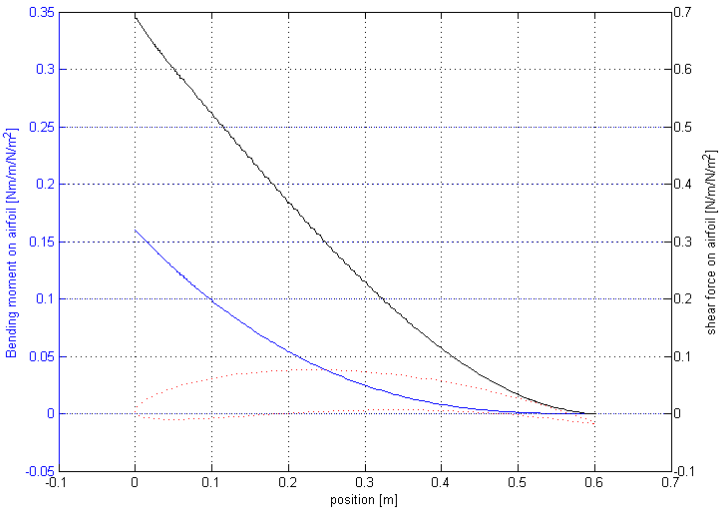

Figure 4.12: Shear and moment distribution around the leading edge, NACA6510 $C_l = 1.148$.

the aircraft ultimate load. Performing a limit load 3.6g manoeuvre with a 4m wingspan requires a lower dynamic pressure of $383N/m^2$, and an equivalent airspeed of 25m/s so this case is automatically satisfied.

The reaction forces from aerodynamic loads can now be evaluated for a dynamic pressure of $664N/m^2$ and a C_L of 1.148. The bending moment coefficient at the leading edge can be read from figure 4.11 at the 0.18m chord location, this is equal to 0.0275. Multiplying this with the dynamic pressure we obtain the bending moment of 18.24Nm per meter span. The same can be done for the trailing edge to obtain a bending moment of 4.16Nm/m. The bending moment is transferred by a horizontal force couple on the top and bottom skin. For the four digit NACA series airfoil of the CHANGE design the thickness at the 30% and 70% locations is 60mm and 35mm respectively. This leads to a horizontal reaction force of 304N per meter span at the leading edge and 119N per meter span at the trailing edge. When this force is concentrated at each corner of a 900mm section as specified in the elastic loads analysis, then this causes a reaction force of 136.8N at the leading edge surface and 53.6N force at the trailing edge surface. The vertical forces given in this table are of the upper and lower skin combined. Figure 4.10 shows the location and direction of these forces on a trailing edge surface. The value of this shear force for the leading edge is obtained from figure 4.11, where the black line at x position has a value of $0.299N/N/m^2$, multiplying this with the dynamic pressure of 664Pa then one obtains the total vertical force per meter span of 198.7N/m. An overview of the reaction forces is given in table 4.3.

4.4.2 Elastic Loads

The elastic loads are obtained from the ABAQUS model which was also used to determine the nature of the deformation. Two cases were analyzed: symmetric actuation and an asymmetric actuation. These cases were evaluated for both the leading and the trailing

LE Bending moment [Nm/m]	18.24
TE Bending moment [Nm/m]	4.16
LE Total vertical force [N/m]	198.7
TE Total vertical force [N/m]	64.3
LE Horizontal reaction force [N/m]	304
TE Horizontal reaction force [N/m]	119

Table 4.3: an overview of the computed aerodynamic reaction forces in a 5.6g maneuver

edge surface. The objective of the simulation is to estimate the actuation forces required to deform the surfaces, and to obtain values of the reaction forces which the deformed surface exerts on the rest of the wing structure. A 5mm quad mesh was used for the leading and trailing edge models, which corresponds to 12960 elements. The results of the mesh convergence analysis are shown in figure 4.13.

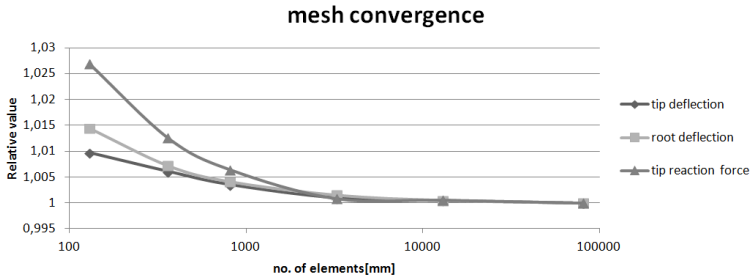

Figure 4.13: Mesh convergence analysis performed on the leading edge control surface geometry, showing adequate convergence below 10mm mesh size. The values are scaled for clarity and should be multiplied by 19.6, 19.4 and 35.67 to obtain the actual values of the vertical tip deflection, vertical root deflection and tip reaction force respectively.

Leading Edge Analysis

The leading edge forces were evaluated in the following configuration: A 1.5mm thick uniform glass fibre laminate of six layers EHG250-68-37 in a [(45)/(0)/(45)/(0)/(45)/(0)] quasi-isotropic configuration. The top edge of the skin is fully clamped while the lower skin is constrained in the vertical direction along two spanwise lines at 10mm and 30mm from the edge. This type of constraint allows translation and rotation in the plane tangent to the skin surface, while limiting rotation along the spanwise axis. The actuation forces are exerted at the outer edges of the forward line. The constraints and the coordinate system are shown in figure 4.14.

Reaction forces are registered in three locations: along the fully clamped upper edge and along the two constrained lower lines. The resulting force distributions are shown in figure 4.15 and figure 4.16, which depict the symmetrical and asymmetrical load case respectively.

Figure 4.15 shows the reaction forces of a symmetric actuation where both corners are

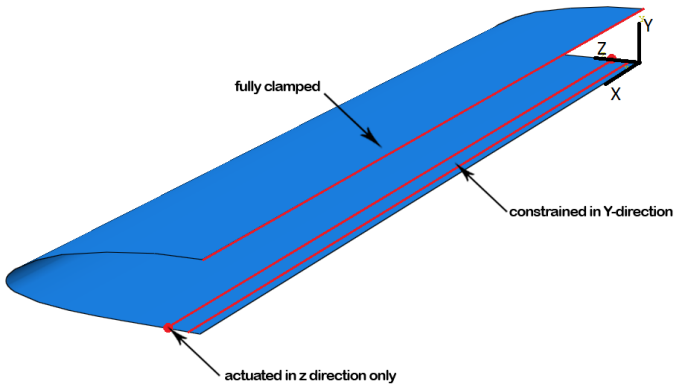

Figure 4.14: The coordinate system, boundary conditions and input locations for the leading edge surface.

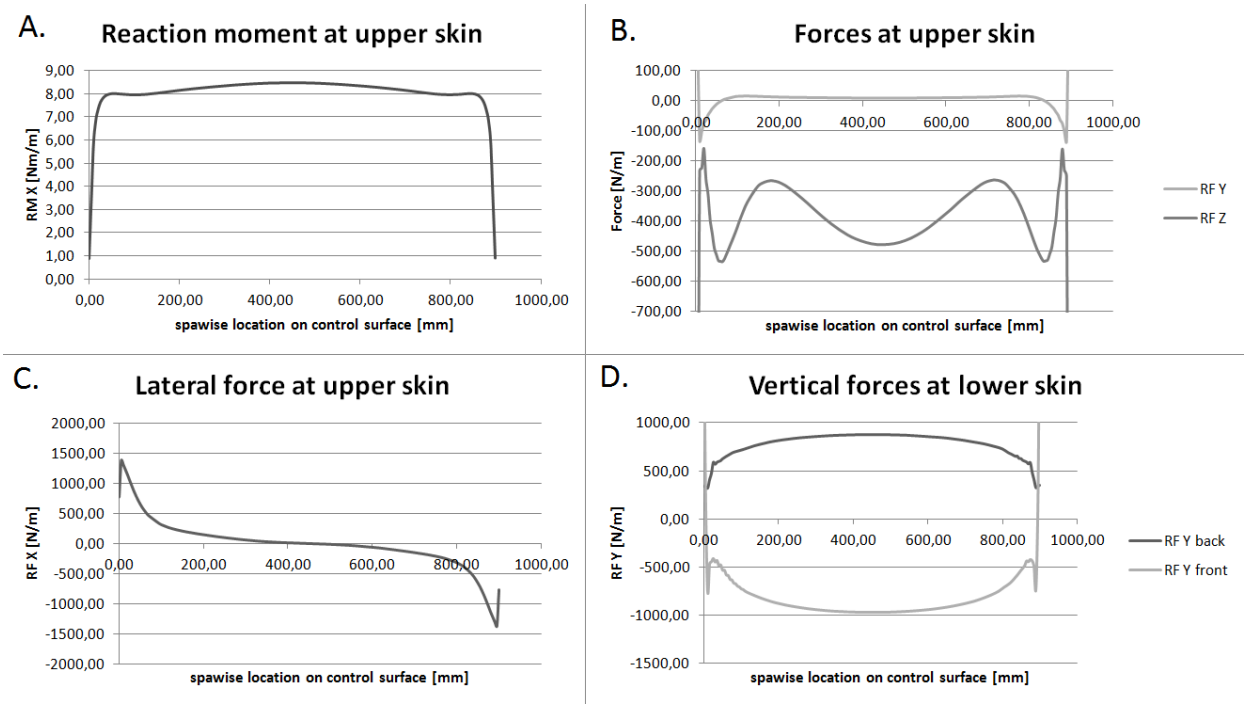

Figure 4.15: The computed reaction forces on the leading edge surface in a symmetric actuation.

moved 14mm forwards, resulting in a 27mm vertical upward displacement at the leading edge. The force required at both input locations is 183N. The graphs represent the distributed forces acting upon the leading edge surface by the constraints. Subplot A is of the reaction moment at the upper skin, which has a relatively constant value with a peak at 8,5Nm/m at the center of the control surface. This value rapidly declines near the edges. Subplot B is of the vertical and horizontal reaction forces at the clamped top skin. The Vertical RF Y distribution shows a fairly weak constant force of approximately 20N/m upwards, which has strong negative peaks near the edges, indicating that the structure has a tendency to deform into a saddle shape, with the ends curling upwards. The horizontal RF Z distribution shows a unusual pattern which varies from -200N/m to

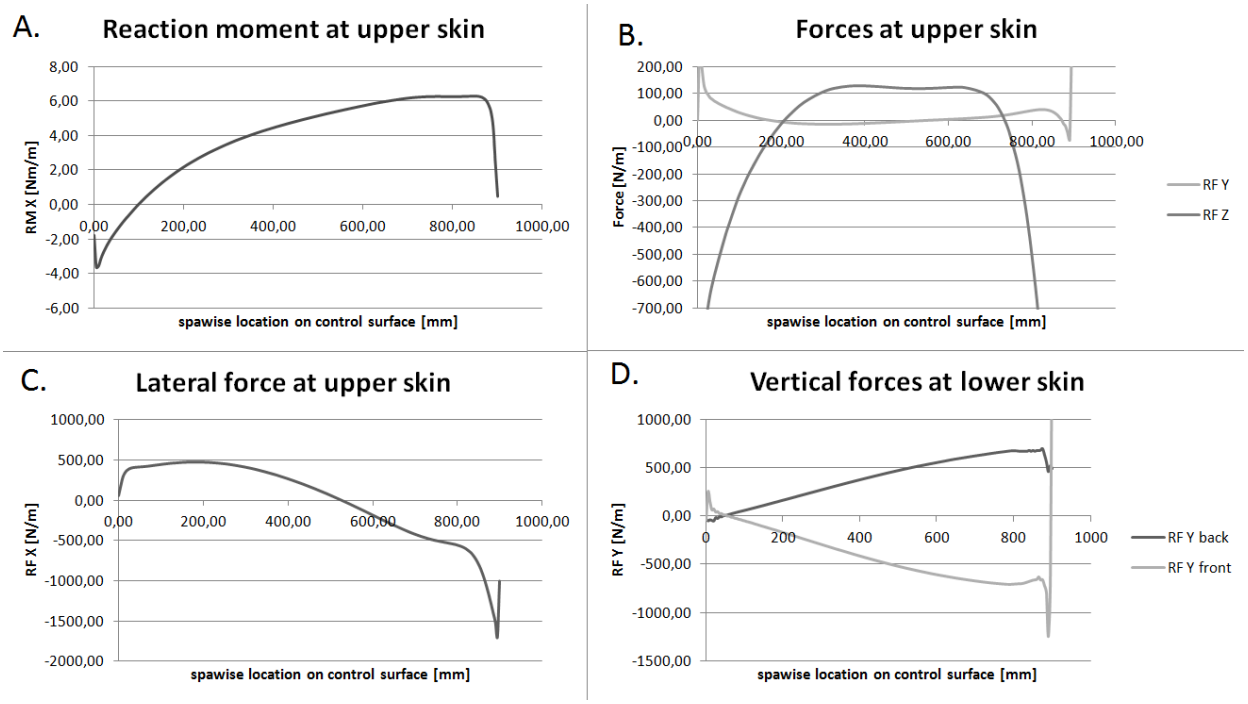

Figure 4.16: The computed reaction forces on the leading edge surface in an asymmetric actuation.

-530N/m (forwards positive). Subplot C shows the spanwise force distribution along the clamped top skin, the values increase at the edges as this force represents the accumulated contraction of the skin. The peak value reaches almost 1500N/m. Subplot D shows the reaction forces at the vertically constrained lines of the lower skin. These show an upwards force at the rear line and a downwards force at the front line, together these form a force couple which resists the upwards rotation of the leading edge and ensures a continuous airfoil shape without kinks. The maximum value of these is 896N/m upwards at the rear position, and 960N/m downwards at the forward position. The values decrease gradually near the edges, the peaks at the outer positions of the forwards distribution can be attributed to the actuation loads.

Figure 4.16 shows the reaction forces of an asymmetric actuation only: the corner at location x=900mm is moved 14mm forwards, the other corner is pinned down. The forward force required at the input location is 131N, while a 52N forward force must be exerted on the pinned corner for it to remain in place. There are some observable differences between both cases. The reaction moment has a lower value at the actuated side, and a negative value at the pinned side. The forces at the upper skin are considerably different, as RF Z has changed direction and exhibits considerably large peaks near the edges. RF Y has also changed direction at the pinned edge, but the magnitude remains approximately the same. The vertical forces at the lower skin remain practically unchanged at the actuated side, and gradually approach zero at the pinned side. The lateral force at the upper skin has a slightly higher value at the actuated edge and then forms a plateau where the skin is pushed towards the center of the surface.

Trailing Edge Analysis

The leading edge forces were evaluated in the following configuration: A 1mm thick uniform glass fibre laminate of four layers EHG250-68-37 cloth in a [(0)/(45)/(45)/(0)] configuration. The top edge of the skin is fully clamped while the lower skin is constrained in the vertical direction along two spanwise lines at 10mm and 30mm from the edge. The actuation forces are exerted at both outer edges of the rear line. The constraints and the coordinate system are shown in figure 4.17.

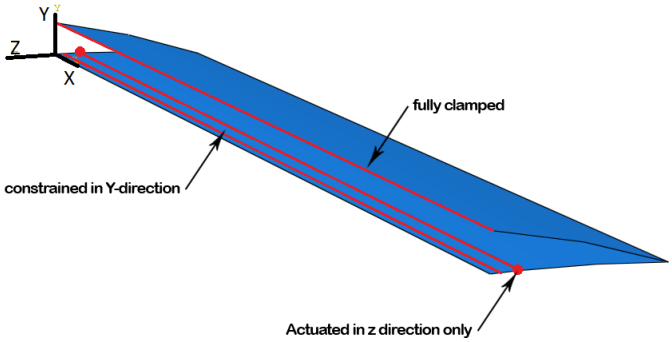

Figure 4.17: The coordinate system, boundary conditions and input locations for the leading edge surface.

The force distributions along the fully clamped edge and along the two constrained lines are evaluated for both a symmetric and an asymmetric case. The resulting force distributions are shown in figure 4.18 and figure 4.19.

Figure 4.18 shows the reaction forces of a symmetric actuation where both corners are moved 6mm backwards, resulting in a 27mm vertical upward displacement at the trailing edge. The force required at both input locations is 130N. The graphs represent the distributed forces acting upon the trailing edge surface by the constraints. Subplot A is of the reaction moment at the upper skin, which has a relatively constant value of no more than -5Nm/m at the center of the control surface. This value slightly rises then suddenly drops near the edges. Subplot B is of the vertical and horizontal reaction forces at the clamped top skin. The Vertical RF Y distribution shows a fairly weak constant force of approximately -25N/m (downwards), which has strong positive (upward) peaks near the edges, indicating that this structure, just as the leading edge surface, has a tendency to deform into a saddle shape with the ends curling upwards. The horizontal RFZ distribution shows a pattern which varies from -50N/m in the center to peaks of over 1000N/m at the edges (forwards positive). This is in contrast to the bumpy distribution encountered at the symmetric leading edge load case. Subplot D shows the reaction forces at the vertically constrained lines of the lower skin. These show an upwards force at the rear line and a downwards force at the front line, which together form a force couple which resists the upwards rotation of the trailing edge and ensures a continuous airfoil shape without kinks. The maximum value of these forces is -377N/m (downwards) at the rear position, and 330N/m (upwards) at the forward position. The values decrease gradually near the edges, and the nature of the distribution has many similarities with the leading edge. The peaks at the outer positions of the forwards distribution can also be attributed to the actuation loads. Subplot C shows the spanwise force distribution

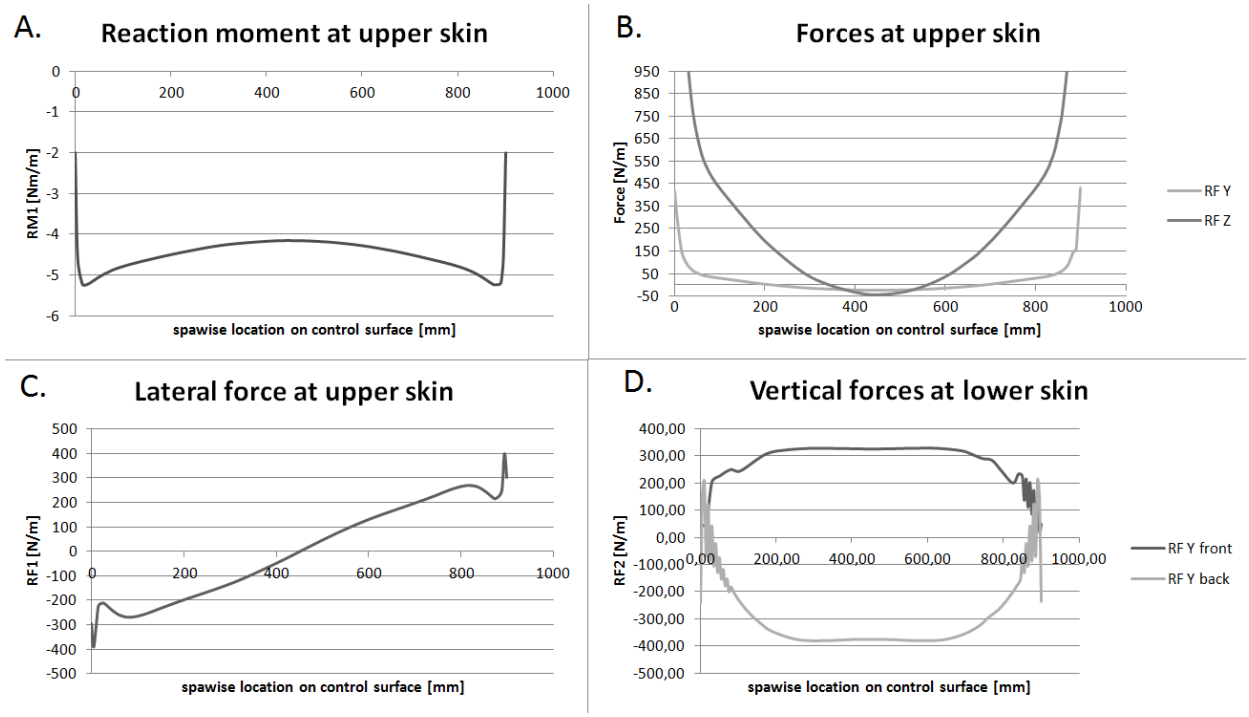

Figure 4.18: The computed reaction forces on the trailing edge surface in a symmetric actuation.

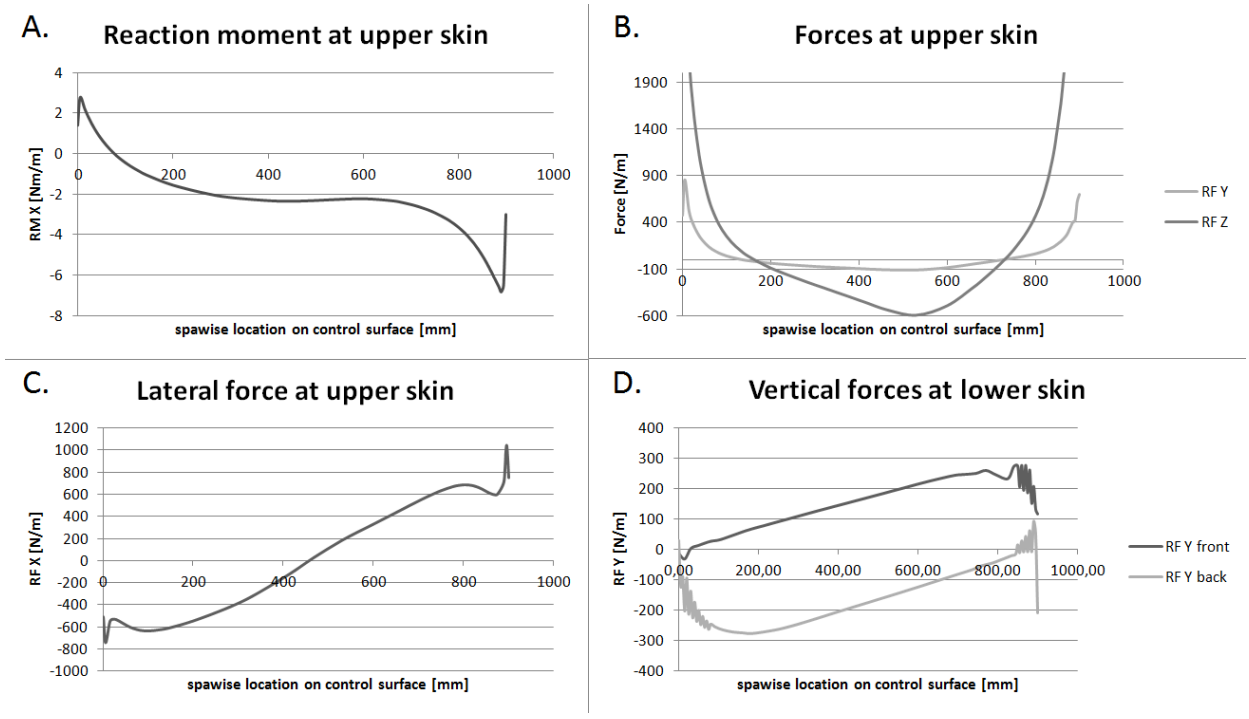

Figure 4.19: The computed reaction forces on the trailing edge surface in an asymmetric actuation.

along the clamped top skin, the values increase at the edges as this force represents the accumulated contraction of the skin. The magnitude of this force is much smaller at the leading edge, with peaks below 300N/m.

Figure 4.19 shows the reaction forces of an asymmetric actuation only: the end at location x=900mm is moved 6mm forwards, the other end is pinned down. The forward force required at the input location is 100N, while a 36N forward force must be exerted on the pinned corner for it to remain in place. There are some observable differences between both cases. The reaction moment has a greater negative value at the actuated side, and a positive value at the pinned side. In contrast to difference between the load cases on the trailing edge, the forces at the upper skin have not changed significantly. RF Z simply shows slightly higher peaks near the edges, but has a much deeper trough which reaches -600N/m (backwards). The distribution of RF Y has changed in amplitude but not in shape. The vertical forces at the lower skin have some differences, as the front constraint force becomes slightly lower at the actuated end, and gradually approaches zero at the pinned side. The distribution of the rear constraint exhibits greater negative values (downward force) near the pinned side. There seems to be some jitter in the values for adjacent nodes near the edges. The lateral force at the upper skin has a higher overall value with little other changes compared to the other load case.

Chapter 5

Mechanical System

A mechanical system is engineered to connect the skin of the morphing system to the wingbox while allowing unconstrained movement in some directions. Other requirements such as modularity, and ease of access for maintenance and inspections are also be taken into account during the design process. The skin joint must allow translation and rotation in the plane tangent to the skin surface, all other types of motion have to be constrained. Part of the resulting aerodynamic and elastic loads are transferred to the wingbox through this system, so it must be able to withstand these structurally. Figure 5.1 shows an overview of the degrees of freedom which are required from the joint mechanism.

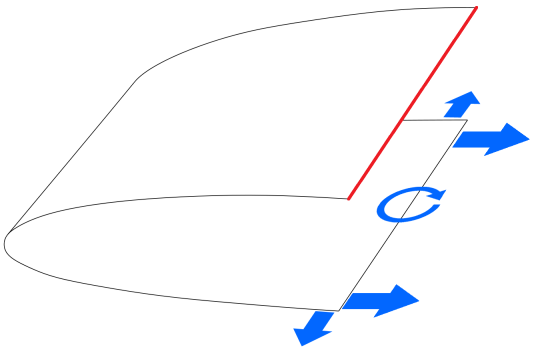

Figure 5.1: The required degrees of freedom in the skin joint.

In all considered concepts the top skin is attached rigidly to the spar in order to ensure a continuous contour. The bottom skin must be able to move relative to the spar, so this is to be linked with a mechanical skin joint. This joint is placed intentionally at the bottom of the airfoil to limit the adverse aerodynamic effects caused by a discontinuity. The red edge on the upper surface in figure 5.1 represents a fully clamped condition, the blue arrows indicate the motions that must remain unconstrained. The magnitude of the required displacements has already been established in chapter 4. Translation normal to the surface and all other rotations are to be constrained to limit discontinuities in the

airfoil shape. The mechanism is also to be modular and easily serviceable, and make as much use of commercial of the shelf parts as possible.

5.1 Joint Concepts

Several mechanical systems are evaluated, each uses a distinctive method to constrain the motion of the skin in the required directions. In order to achieve this the skin can either be clamped between straight or curved guides, slide along discrete pins and slots, or be connected to the spar with a ball linkage system. Each concept is briefly explained, after which the method deemed most suitable is selected in a trade-off.

5.1.1 Curved Guide System

This system uses a continuous slide joint in which a thin and elastic skin is allowed to move between two curved guides. The curve of the guides allows the skin to retract upwards and avoid space constraints due to the presence of the spar. The system has been proposed by a project partner and a technology demonstrator has already been built by TEKEVER. An annotated section view of the system applied to a trailing edge flap in shown in figure 5.2.

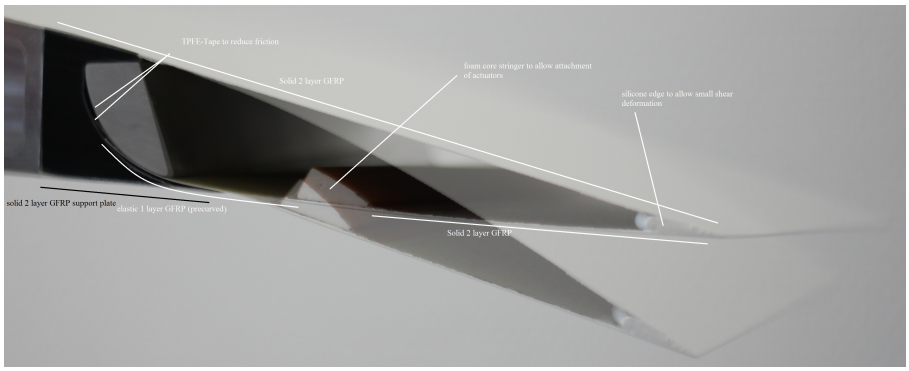

Figure 5.2: A slide joint for thin skins using curved guides (image from TEKEVER)

The curve in the guides also limits the thickness of the skin that can be used with this system. The strain in a sheet of material is related to the ratio of the bend radius with relation to the thickness of the sheet, so the radius must be decreased for thicker skins. Equation 5.1 can be derived from Bernoulli-Euler bending theory:

$$\varepsilon = \frac{t}{2R} \tag{5.1}$$

This equation can be used to determine that a 30mm radius in a 1mm thick skin causes a strain (ε) of 1.6%, which is still below the elongation at break for glass fibers. However, a section of the skin has to slide in and out of the curved guide every time the airfoil

shape is changed, which might cause fatigue related defects in the long term. The energy required for this deformation must be also be delivered by the actuators at every cycle. Further limitations of the proposed systems are that it takes up a lot of room and that little volume remains available for the actuators.

5.1.2 Straight Guide System

The disadvantages of the curved guide system are caused mainly by the curved nature of the supports, an otherwise identical straight system can also be considered. The concept is depicted in figure 5.3.

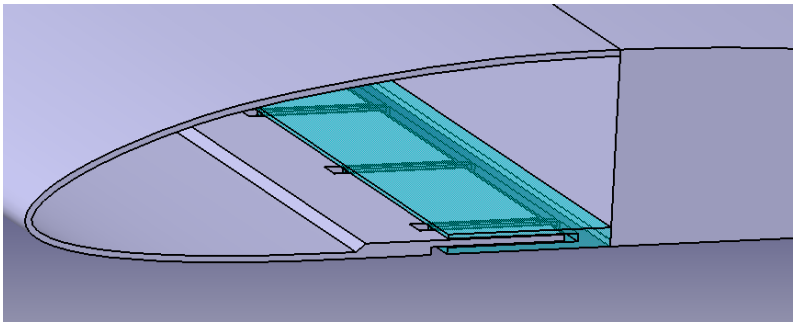

Figure 5.3: A straight guide system fitted to the leading edge surface.

This concept leaves ample room for actuators, but the rigid section must extend far enough forwards to adequately support the skin, which increases the force required for a given deflection. Figure 5.3 shows how the lower guide plate is connected to the upper plate through slots in the skin, which allows these plates to be remain relatively thin and lightweight.

5.1.3 Rigid Slot System

A solution can also be found which does not require significant local deformations. This relies on a system with rigid flat pins which slide trough hat shaped guides. Figure 5.4 shows a trailing edge surface fitted with such a system.

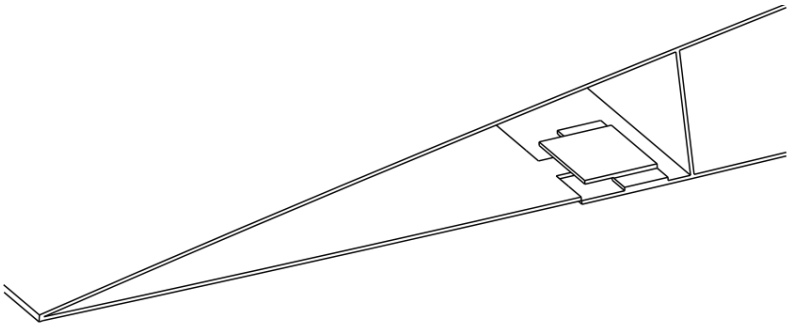

Figure 5.4: A slide joint using rigid elements.

This provides free motion in all required directions. The hat guides are wider than the pins which allows the lowed skin to move a certain distance in a spanwise direction to accommodate the deformations required for twist morphing. The pins can also move in and out of the hats to meet the needs of the camber deformations. The low profile of the guide system leave ample room for actuators and wire looms to be placed inside the adaptive sections. Further development of this concept would require a method to be found for reliably attaching the rigid pins and guides to the composite skin.

5.1.4 Ball Linkage System

The translation of the lower skin can also be approximated by a parallel mechanism consisting of sets of push-rods connected to the structure via ball-linkages. These effectively constrain the distance between the upper and lower skin, thus confining the movement of the latter to a circular translation around the fixed end of the ball joint. In plane rotation required for twist deformation is also possible provided the skin can slightly elastically deform out of plane. The principle of operation is shown in figure 5.5.

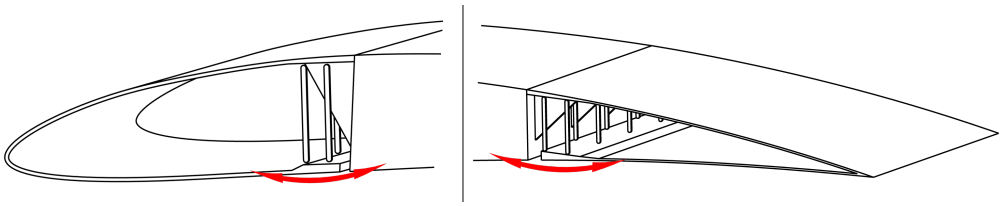

Figure 5.5: A joint using linkages

5.2 Trade-off

The linkage system and the straight guide system are considered as concepts for this application. Both designs have been worked out in further detail in order to determine the best solution for a detail design. The choice is made based on manufacturing, assembly and the total mass of the system.
The manufacturing score takes into account the type of tooling required to manufacture the parts. This includes machining operations: the number of faces which need to be milled, the number of faces that have holes, the number of holes with threads and the number of jigs needed. Special requirements on the skin are also taken into account, this includes bonding steps and double moulds to ensure tolerances on the skin thickness. The latter is needed at locations where the inside of the skin must have a well defined contour, such as at the location of the attachment with the ribs, and between the guide plates.
The assembly score consists of the total number of parts in the system, the steps required for assembly, and the number of parts which need to be disassembled in order to access the actuators.
The mass score is based on the estimated total mass of the components, the mass of the skin is not included, as it would otherwise dominate this value.
These values are obtained from the design state of both concepts at the time that the trade off was performed, and therefore do not reflect the final detailed design. The design

of both concepts was brought to a level where the trade-off criteria could be evaluated with reasonable confidence. Though obviously some changes have been made during the detailed design process, the layout, basic shape and manufacturability of components has remained largely unaltered.

The results of the trade off are presented in table 5.1 and table 5.2 for the leading edge and trailing edge respectively. This analysis supports the decision to use the ball linkage mechanism for the leading edge surface, and to use the guide plate mechanism for the trailing edge surface. Though the results indicate a close tie between both concepts for the trailing edge, a practical reason for using the guide plate system is that the smaller scale of the ball linkage mechanism would make assembly excessively tedious and labour intensive.

Leading edge		Bias	Ball Links		Guide Plates	
Mass	Mass [g]	5,00	271,00	3,39	400,00	5,00
Manufacturing	Faces w. holes [#]	1,00	2,00	0,67	3,00	1,00
	Threads [#]	1,00	1,00	0,33	3,00	1,00
	Holes [#]	1,00	25,00	0,56	45,00	1,00
	Jigs [#]	1,00	2,00	0,67	3,00	1,00
Skin	Double mould [#]	1,00	1,00	0,50	2,00	1,00
	Bonding [#]	1,00	1,00	0,09	11,00	1,00
Assembly	Assy. steps [#]	2,00	5,00	1,43	7,00	2,00
	Parts [#]	2,00	71,00	2,00	38,00	1,07
	Disassy parts [#]	2,00	10,00	0,95	21,00	2,00
Total				10,58		16,07

Table 5.1: The trade off which led to the selection of the ball linkage system for the leading edge surface.

Trailing edge		Bias	Ball Links		Guide Plates	
Mass	Mass [g]	5,00	138,00	5,00	115,00	4,17
Manufacturing	Faces w. holes [#]	1,00	2,00	0,67	3,00	1,00
	Threads [#]	1,00	2,00	1,00	2,00	1,00
	Holes [#]	1,00	35,00	1,00	30,00	0,86
	Jigs [#]	1,00	2,00	0,67	3,00	1,00
Skin	Double mould [#]	1,00	1,00	0,50	2,00	1,00
	Bonding [#]	1,00	1,00	1,00	1,00	1,00
Assembly	Assy. steps [#]	2,00	5,00	2,00	4,00	1,60
	Parts [#]	2,00	66,00	2,00	27,00	0,82
	Disassy. parts [#]	2,00	5,00	0,91	11,00	2,00
Total				14,74		14,44

Table 5.2: The trade off which led to the selection of the guide plate system for the trailing edge surface.

5.3 Actuator Sizing

The horizontal force at the joint is transferred via the actuators into the wing structure. Therefore the actuators must be sized to provide both the necessary force and displacement required to deform the structure in flight. This can either be done using many small actuators positioned along the span, or two larger ones at the extremities. Only commercial of the shelf servomotors have been considered for availability reasons. A torque-weight diagram of several RC servos is shown is figure 5.6.

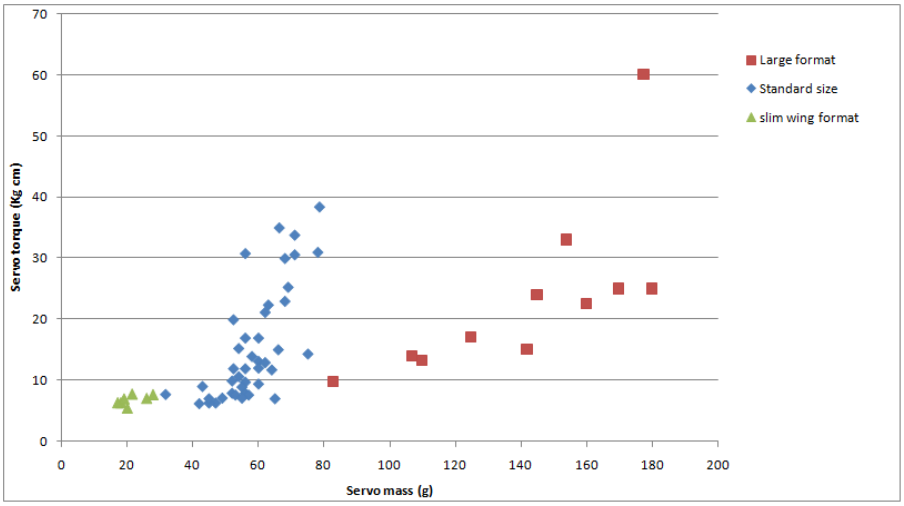

Figure 5.6: The torque to weigh distribution for various types of RC servos. (data from ServoDatabase.com)

One notices that weight of servos is mainly related to size, and only to a lesser extent to torque. The large format servos have dimensions of around 60x30x60mm, standard format is 40x20x40mm and Slim Wing servos are thinner than 20mm. The weight penalty without apparent torque increase of large format servos has discouraged their application in this design. The low increase in mass for added torque also points towards the use of two large servos rather than many smaller ones. Size is also a driving factor, as the center wingbox must be left empty to accommodate the extending wing. Therefore the entire actuating mechanism must be housed inside the leading and trailing edges. A full sized mock up has confirmed that it is possible to house a standard size servo inside the trailing edge while allowing sufficient room for actuation. The volume of the leading edge is sufficiently ample to accommodate any servo without difficulty.

The results discussed in chapter 4 show that the travel required from the leading edge servo is 13mm, and 8.3mm at the trailing edge. When using a servo with 180 degrees travel the length of the servo horn can be half the required displacement length. This has the added benefit of providing an over-centre mechanism in both extreme positions, so that the actuator does not have to provide torque to maintain the elastic and/or aerodynamic loads constantly. The torque required from each servo can be computed by combining the aerodynamic loads and the elastic loads which are presented in chapter 4.

Figure 5.7 shows the torque which must be delivered by the leading edge actuator from zero to 13mm displacement for various aerodynamic loads with 10N increments. The

assumption is made that the surface is actuated at the corner, which is consistent with the analysis in section 4. If the servo has a 6.5mm arm and 180 degrees travel then the torque can remain zero in the two extreme positions. An increasing aerodynamic load alleviates the maximum torque required, and even reverses the value at higher loads. The aerodynamic force expected on a single actuator during level flight is approximately 25N, the 140N load corresponds to the 5.6g load case. The maximum elastic load is 183N.

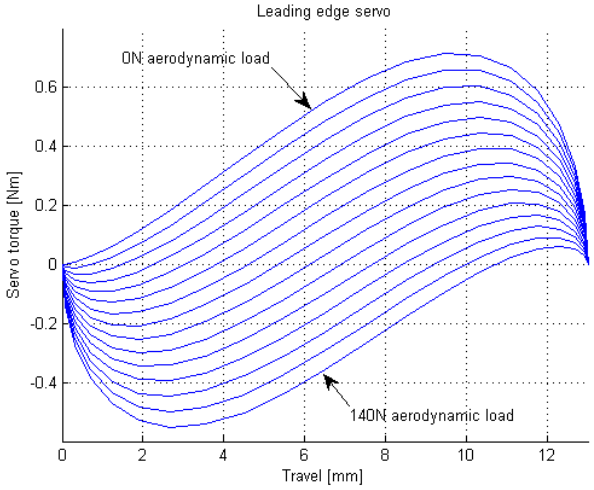

Figure 5.7: The torque curves of a leading edge actuator for various aerodynamic loads. The servo arm is 6.5mm long, travel is 180 degrees.

From this plot one can determine that the servo must provide at least 0.7Nm (7kgcm) of torque continuously. This can be met with a standard size servo, specifically the Hitec HS-7950TH. Full specs of this servo are given in table 5.3.

Figure 5.8 shows the torque which must be delivered by the trailing edge actuator from -2.1 to 6.2mm displacement for various aerodynamic loads with 10N increments. Here too the assumption is made that the surface is actuated at the corner as in section 4. This servo only has a 130 degree travel so the torque can only be zero in one position and the arm must be longer than half the total travel, namely 5mm. An increasing aerodynamic load also alleviates the maximum torque required at upward deflections, but increases the absolute value at downwards trailing edge deflections. The aerodynamic force expected on a single actuator during level flight is approximately 10N, during a 5.6g maneuver this is approximately 54N. The maximum elastic load occurs when the trailing edge is deflected fully upwards, and is 130N.

The trailing edge servo must provide at least 0.4Nm (4kgcm) continuously. A MKS HBL6625 servo has been selected for this purpose. This servo can deliver over 10kgcm of torque and has a thin profile which is preferable for the trailing edge. Full specifications are given in table 5.3 and figure 5.9.

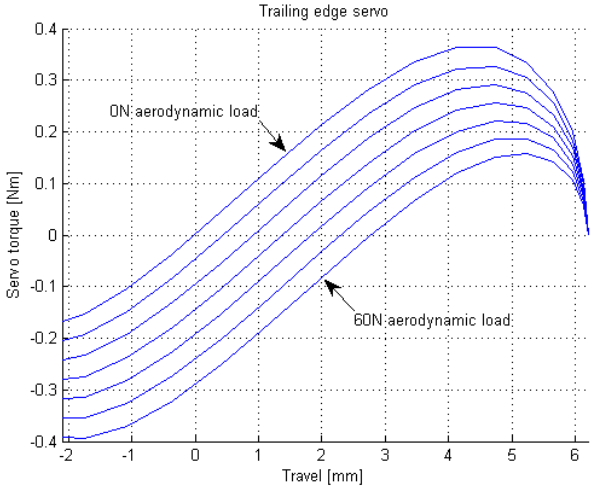

Figure 5.8: The torque curves of a trailing edge actuator for various aerodynamic loads. The servo arm is 5mm long and the servo travels 130 degrees.

-	Leading edge	Trailing edge
Type	HS-7950TH	HBL6625
Mass [g]	68	28
Dimensions [mm]	40x20x38	30x10x35
Stall torque [kgcm]	35	10.4
Operating speed [sec/60deg]	0.13	0.11
Rated voltage [V]	7.4	8.4
Max current [A]	4.5	1.5
Cost [USD]	150	130

Table 5.3: Servo properties.

5.4 Mechanism Detail Design

The sizing process involved making an initial overall design, then estimating the forces to which each part is subjected and finally optimizing the part for those loads. The concept of the wing structure specified that the shear web would have appropriate threaded holes for mounting the leading and trailing edge assemblies. The mechanism is contained entirely within the leading and trailing edges, as can be seen in figure 5.10 which shows the full range of deformation of the system.

5.4.1 Leading Edge

The leading edge surface is actuated via a system of ball linkages which connect to the lower skin. Parts are designed to attach the upper part of the ball linkages and the upper skin to the wing structure, and also to attach the lower end of the ball link to the lower skin. A method is devised to attach the actuators to the wing structure and the lower skin surface. The ball linkages are commercially available, the specific make used in the

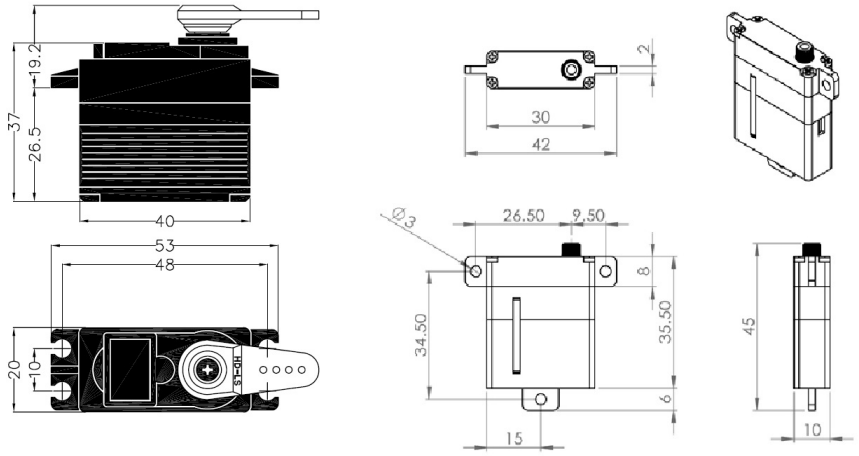

Figure 5.9: Dimensions of the servos used in the design. HS-7950TH (left) and HBL6625 (right).

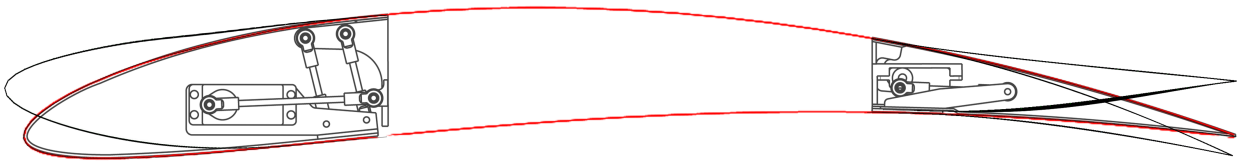

Figure 5.10: An illustration of the mechanism inside the wing structure showing the full range of deformation.

drawings are M3 Truck Specs Rod Ends but these may be substituted with any other suitable replacement.

This is achieved by placing five ribs at constant intervals along the span. The ribs attach to the upper skin and the wing spar, while providing support for the ball linkages. The linkages in turn connect to a T-shaped part which is bonded to the lower skin. The servos are also mounted on these T-shaped extrusions, and connect to the rear spar via a bracket. The design is shown in figure 5.11. Technical drawings of all individual parts can be found in appendix A.

A total of five ribs are used, which is driven by bulging of the skin in between linkages rather than stresses in the mechanisms. These ribs connect to the wingbox shear web with two M4 hex head bolts. Sufficient clearance is provided around the head to use a ratchet ring spanner for easy assembly and maintenance. The top skin is attached to the ribs by a single row of countersunk fasteners, where a local reinforcement is to add sufficient skin thickness to prevent pull-trough failure. By nature, the ball links guide the skin in a circular path as it slides forwards, though the vertical displacement is no more than 1.5mm for a horizontal travel of 13mm and a 44mm linkage length.

The gap between the skin surface and the wingbox can be sealed using special mylar tape

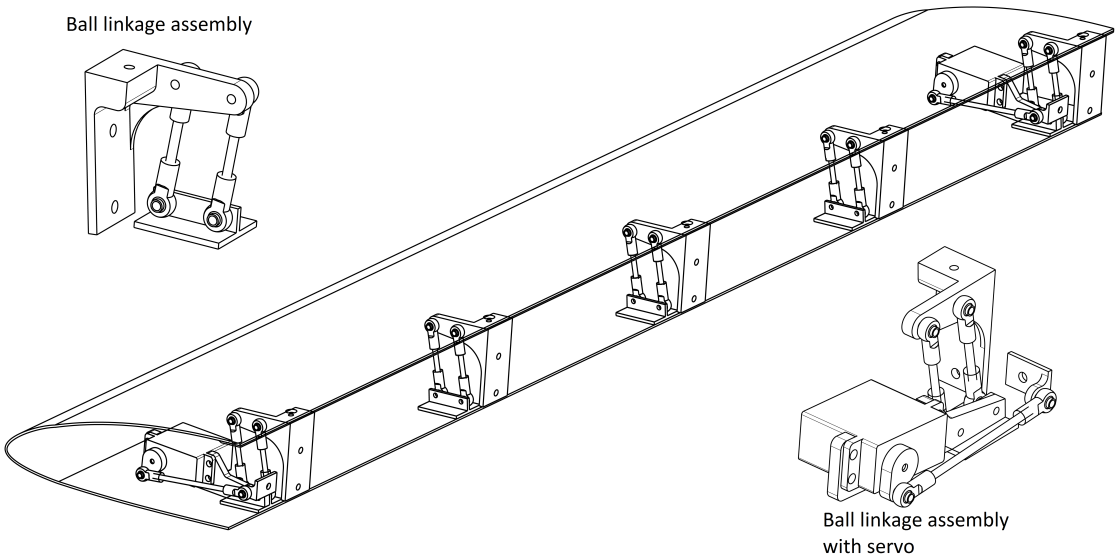

Figure 5.11: Final design of the leading edge assembly.

[22], as is commonly used on control surfaces in general aviation. The pre-bent mylar tape provides a flexible seal which can be attached to the leading edge skin and bridges the gap created when the airfoil is deflected upwards. Figure 5.12 shows the sealing tape combined with a turbulator strip to seal the gap between the vertical stabilizer and the rudder.

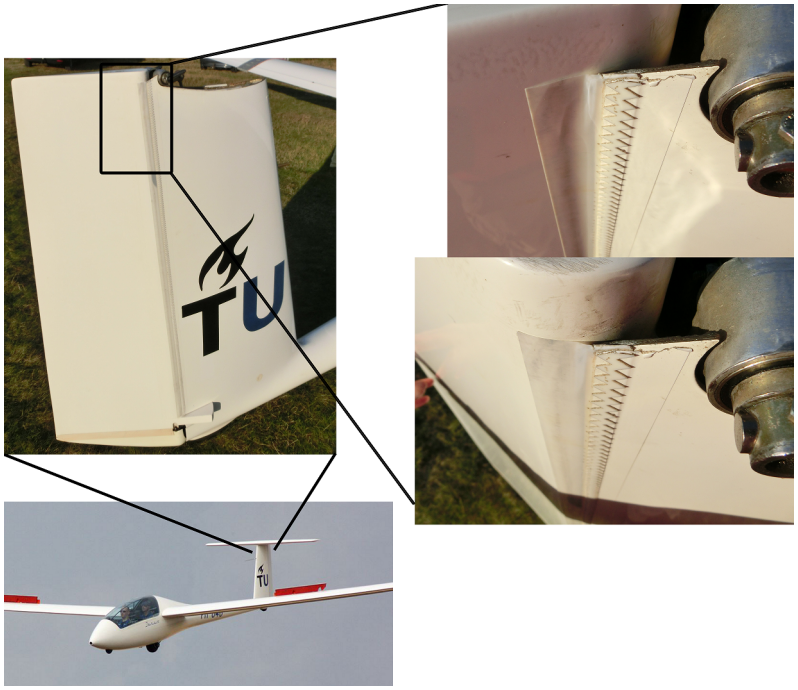

Figure 5.12: Mylar tape used to seal a gap between a vertical stabilizer and rudder.

5.4.2 Trailing Edge

The trailing edge surface is joined to the wing structure via a sliding joint where the reaction forces of the lower skin are carried by two parallel plates which act as slide bearings. These are also held in place by five rib-like brackets which are mounted on the wing box. The plates are of the same thickness as the wing skin, and of the same material. The actuator servo mounts to the wing box via a bracket and actuates the lower skin via a pushrod connected to an arm extending from the lower skin. The top guide plate is interrupted at the extremities to allow for the control horn to be bonded directly to the lower skin. An assembly view is shown in figure 5.13. Technical drawings of all individual parts can be found in appendix A.

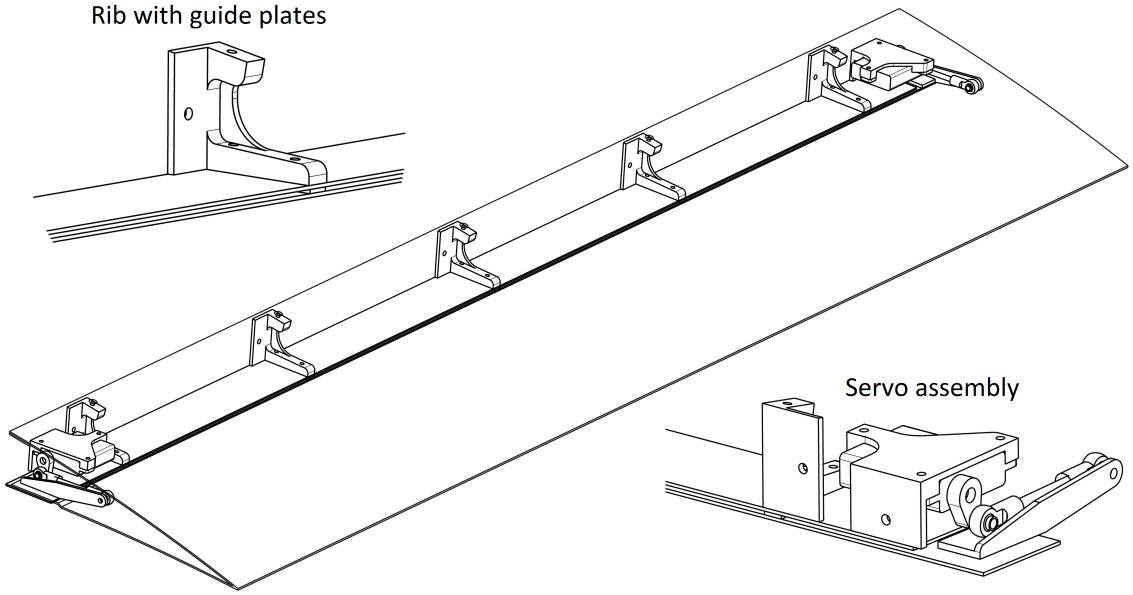

Figure 5.13: Final design of the trailing edge assembly.

The guide plates are joined together by inserts which align with the ribs so that these can be firmly connected using countersunk fasteners. The ribs are connected to the wingbox with single M3 hex bolts. The top skin is also attached to the ribs by countersunk fasteners. A local reinforcement of the skin is to provide additional thickness to prevent pull-trough failure. Gaps must be left in the lower skin so that it can slide around the inserts with sufficient margin to accommodate the sideways travel experienced during maximum twist deformation. A view of just the skin is provided in figure 5.14. The skin can slide inwards a total of 4mm, and still has a 20mm overlap with the guide plates when it is extended outwards by 10mm. This offers a considerable margin to the estimated values for the displacement as defined in chapter 4. The total depth of the guide plates is 35mm.

5.5 Design Loads

The aerodynamic and elastic reaction forces acting on the skin are calculated in chapter 4. These are used to obtain an estimate for the forces acting on each part of the mechanism.

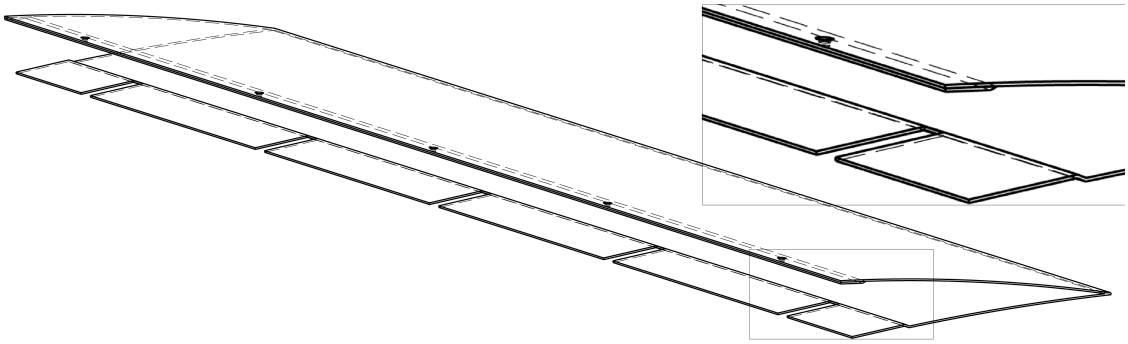

Figure 5.14: The trailing edge surface skin showing the slots.

A margin is taken by assuming the peak force applies over the entire span of the actuated surface. This allows some future modifications to be made to the skin layup without requiring a redesign of the mechanisms.

5.5.1 Leading Edge

For the five identical supports of the leading edge, discrete forces can be identified on each segment, these are indicated on figure 5.15. The forces are in relation to the coordinate system of the surface model, which is tangent to the direction of travel of the lower skin, hence the slight rotation with respect to the front spar. The values of these forces are given in table 5.4. Not shown are the reaction forces at the bolt holes and along contact area with the wingbox.

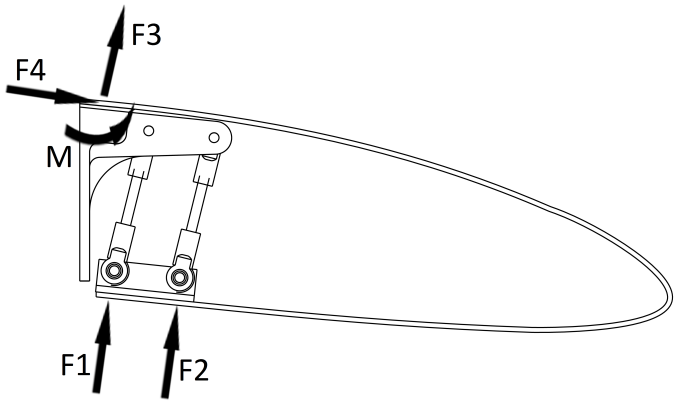

Figure 5.15: The forces on the leading edge mechanism.

Additional forces are introduced by the actuators. These are assumed to only affect the outer mechanisms and are further discussed in section 5.6.

5.5.2 Trailing Edge

Discrete forces can also be identified on each segment of the five identical supports of the trailing edge, these are indicated on figure 5.16. The values of these forces are given in

-	Elastic	Aerodynamic
F1 [N]	-161	9
F2 [N]	173	9
F3 [N]	10	18
F4 [N]	95	-55
M [Nm]	1.53	0

Table 5.4: The values of the forces on the leading edge mechanism.

table 5.5. As the peak load of F4 is quite high in the edge, the highest value is not used, instead the value is based on the reaction forces 100mm from the edge of the skin. This can be justified because the top skin is not fully clamped but rather pinned in discrete locations, so the local average force near the outer fastener can be used for sizing.

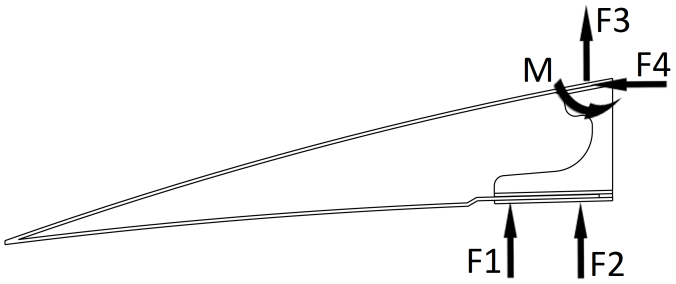

Figure 5.16: The forces on the trailing edge mechanism.

-	Elastic	Aerodynamic
F1 [N]	68	3
F2 [N]	-60	3
F3 [N]	-27	6
F4 [N]	81	-21
M [Nm]	-1	0

Table 5.5: The values of the forces on the trailing edge mechanism.

5.6 Verification

A verification is performed to check whether the mechanisms are able to withstand the predicted loads. This can be done using back of the envelope calculations for most parts, while FEM analysis in ABAQUS is used for the more complex components such as the ribs and skin. All fasteners and components are checked for stress during predicted operational conditions. Some parts have seen several iterations of design and analysis in order to reduce peak stresses, while other parts, such as most fasteners, are sized mainly for manufacturability and are therefore structurally over-dimensioned.

5.6.1 Leading Edge

The major components of the leading edge mechanism are the ball linkages, the T-shaped extrusions, the skin, the ribs and all of its fasteners, and the servo mounting plate.

Ball Linkages

The ball linkages are commercial off the shelf parts commonly used in unmanned aircraft, the specific type used in the design is an 'M3 Truck Specs Rod End'. The ball linkages are connected by a threaded rod which can be adjusted to the appropriate length. These rods must withstand the tensile and compressive forces of F1 and F2 in figure 5.15, which are estimated to be in the order of 200N. The Euler buckling equation for pinned columns (equation 5.2) is used to check whether the compressive force is within limits. The critical force for an M3 steel threaded rod with a length of 44mm is 1955N, which is an order of magnitude above the expected load.

$$F_{crit} = \frac{\pi EI}{L^2} \tag{5.2}$$

The ball linkages are attached to the ribs and T-shaped extrusions with M3 bolts which have a stress area of 5.03mm^2. For a 200N shear force this results in a 40MPa shear stress, which is achievable with bolts of any class. The inserted thread length in the ball linkages is also not critical, as a contact area of 5mm (or 10 turns) would result in an acceptable 10Mpa shear force when subjected to a 200N axial load [26]. A margin of safety of over 10 is achieved even with 316 stainless steel threaded rod.

T-extrusions

The T-extrusions are checked for stresses around the holes used to connect the ball linkages. Bearing stress is 33.3MPa. Shear tear-out stress is 11.1MPa.

The extrusions are bonded to the skin, so it must be verified that no excessive peel forces occur. A typical maximum peel force for an aluminium-epoxy bond is 300N/25mm which provides a 50% margin even when the conservative assumption is made that the whole force is carried through by the very edge of the part. The edge where peel stress is expected is shown in figure 5.17.

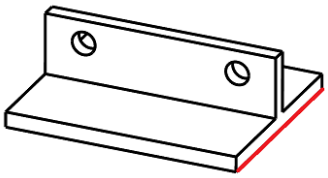

Figure 5.17: The edge (in red) on the t-extrusion where peel stress is expected to occur.

The servos are attached to the two outer extrusions of each leading edge control surface. A 200N actuation force can cause a 5Nm in-plane torque on the bonded joint. For the 30mm by 25mm bonded area of the extrusion this induces an additional shear distribution with a peak value of 1.2MPa located at the center of the long edge. This is shown in figure 5.18.

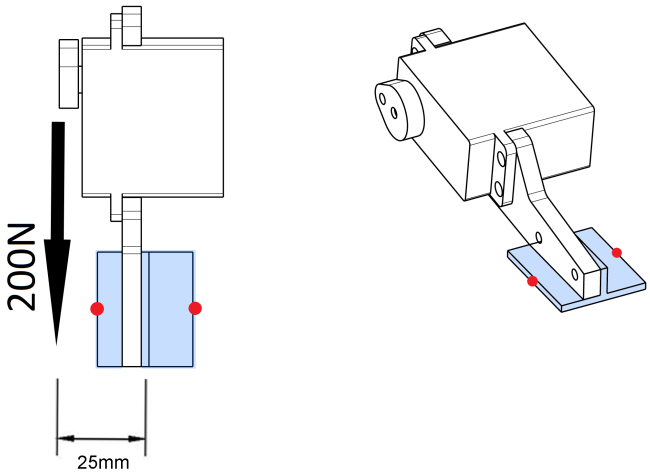

Figure 5.18: The actuation force causes a 5Nm torque on the extrusion. The red dot indicates the location of the largest shear stress in the bond due to this torque.

Leading Edge Skin

The ABAQUS finite element analysis results described in chapter 4 are used to verify that no excessive strain occurs in the skin during maximum deformation. The maximum strain when the skin is symmetrically deflected to its top position is 0.22%. This strain occurs in the outer ply of the lower skin, as can be seen in figure 5.19. In the asymmetric deformation case the max in plane strain is 0.198% which occurs at the actuation point on the lower skin. This is well below the elongation at break for GFRP.

The upper edge of the skin is attached to the ribs by means of mechanical fasteners, the stresses around these holes are also evaluated. The skin is locally reinforced to a thickness of 2.5mm in a quasi-isotropic laminate. The holes are located 2.5 times the hole diameter from the edge. The horizontal shear force varies from -55N to 95N per hole, where a positive force causes tension in the skin. The bearing stress for the 95N load is 12MPa. Net section tension is negligible because of the large spacing between the holes. The tear out stress is 2.5MPa.

The fastener is also slightly loaded axially, the magnitude of this force is expected to reach up to 28N for the elastic and aerodynamic forces combined, with an additional 200N caused by the reaction moment creating a force couple with the edge of the rib. The pull-through forces for countersunk fasteners in thin composite laminates could not be found in literature, but were the force to be transferred directly from the skin to the shaft of the bolt then this would cause no more than a 8.5MPa of shear stress during operation.

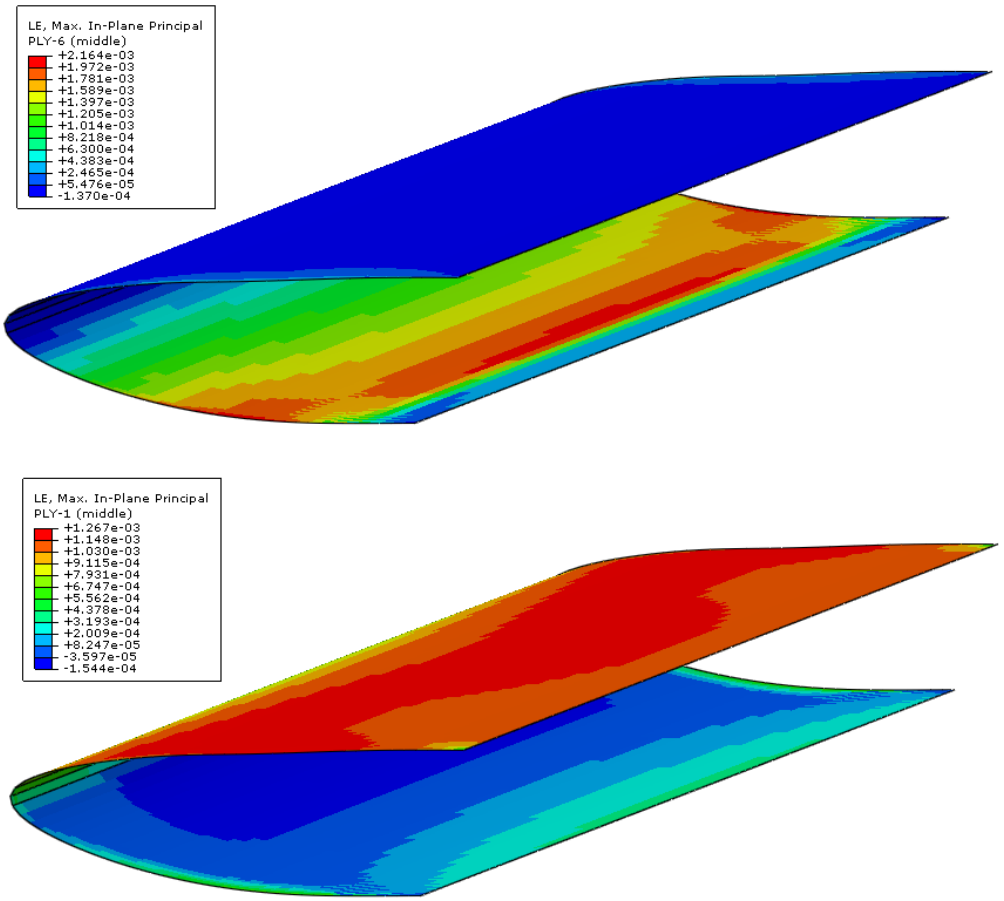

Figure 5.19: The maximum in-plane strain of the leading edge skin at maximum symmetric upward deflection, for outer ply (top) and inner ply (bottom).

The lower skin is bonded to the T-shaped extrusions which constrain its movement locally. The behaviour of the skin in between these supports is analyzed using an ABAQUS simulation. The same material properties and simulation parameters are used as for the analyses of chapter 4. A section of flat but otherwise identical laminate to that used on the leading edge skin is fully clamped on one edge. It can translate vertically and forwards only on both side edges, while the rotation in the longitudinal axis is constrained on these edges.The remaining edge is completely free. This is done to simulate a section of skin which is part of an infinitely long wing. The T-shaped part is tied near the free edge of this sheet, and a force couple of 225N is applied to mimic the forces exerted by the ball linkages. Results of the simulation indicate that the unsupported parts will bulge out slightly, but this is predicted to be only 2.47mm at the peaks. The more concentrated constraint of the extrusions does increase the strain slightly, to a maximum of 0.71% in the outer ply just in front of the T-shaped extrusion. The strain distribution in the outer ply and the nature of its deformation is shown in figure 5.20.

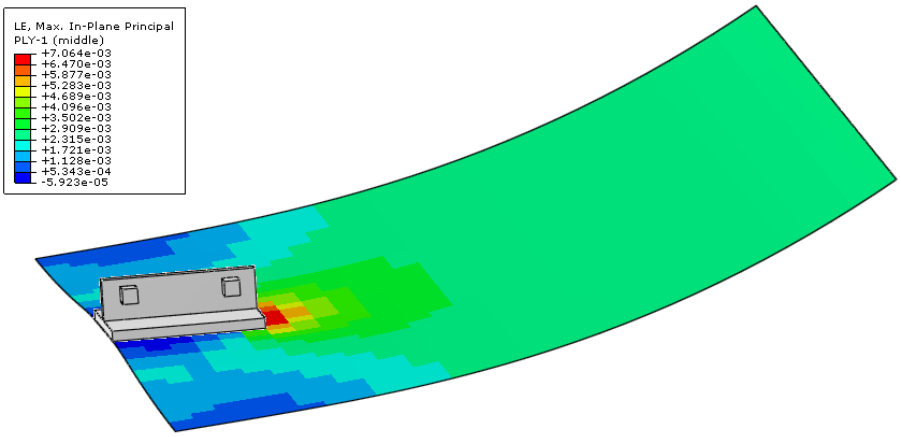

Figure 5.20: The maximum in-plane strain of the leading edge skin around the bonded T-shaped part of the leading edge mechanism.

Leading Edge Rib

The complex topology of the ribs calls for a numerical analysis when it comes to calculating the internal stresses caused by the reaction forces of the skin. A 2mm quadratic tet mesh is used for this analysis. A 375N upward force is applied to the forward ball linkage hole, and a 375N downwards force is applied to the other ball linkage hole. The part is clamped at the two spar attachment holes.

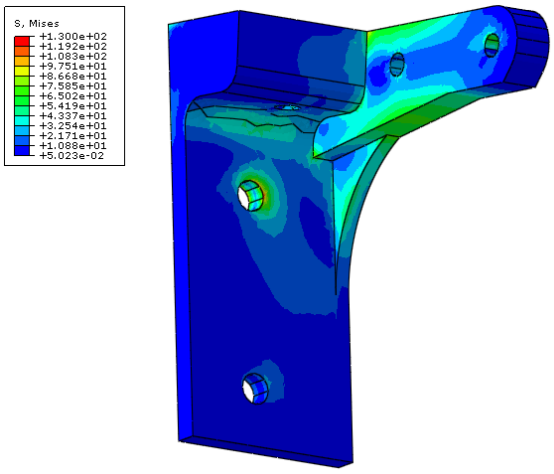

Figure 5.21: The Von Mises stress in the leading edge rib.

Several iterations of this design were evaluated, the top beam has been made thicker and the flange below the top beam have been enlarged to limit stress concentrations in these locations. The high stresses around the top clamped bolt hole can be considered an artifact of the analysis, as the head of the bolt and washers will distribute the reaction forces over a larger area. The stresses in this part allow it to be made of aluminium alloy with a margin of safety of 2.5 in case of 7075T6.

Two M4 bolts are used to attach the ribs to hardpoints provided in the shear web. M4

bolts of 8.8 class have a tensile yield load of 5.6kN, this surpasses the sum of all forces on the rib by an order of magnitude. The same holds for the M3 countersunk fasteners used to hold down the top skin, which have a yield stress of 3kN but are required to hold only 48N. The local hole stresses caused by the ball linkages in the upper 'beam' of the rib are all lower than 15MPa.

Servo Mounting Plate

The servo is held in place by a 5mm thick plate attached to the T-shaped support as shown in figure 5.11. The load on the servo is transmitted to the skin via this part. The thickness of the bracket is driven by bending caused by the offset force. The distance between the neutral plane of the bracket and the joint of the ball linkage is 20mm, for a 200N actuation force this causes a 4Nm moment in the bracket. This can be analyzed using classical beam theory, the maximum stress is estimated to be 74MPa at surface of the section at the forward hole. The servo is mounted on the bracket using screws, where a pair of two screws must carry a load of 83N.

The ball linkage connecting the servo to the wingbox is 85mm long, using equation 5.2 the critical load for this linkage is 524N, while only 200N is expected during operation.

5.6.2 Trailing Edge

The following parts of the trailing edge mechanism are analysed: the skin, the ribs, the servo mount and the control horn. The guide plates are not further evaluated as it is assumed that the lower plate's thickness being 50% greater than that of the trailing edge skin ensures a sufficiently over-dimensioned design.

Trailing Edge Skin

A numerical analysis is performed to verify that no excessive strain occurs in the skin during operational deformation. The ABAQUS simulations are used to determine the strain in the plies at maximum symmetric and asymmetric deformation. Figure 5.22 shows the strain distributions in the symmetric case, and figure 5.23 shows the strain in the asymmetric case. The maximum strain of 0.18% occurs at the clamped top skin near the edge in the asymmetric deformation case. This is well below the elongation at break for glass fiber composites.

The upper edge of the skin is attached to the ribs by means of mechanical fasteners, the stresses around these holes are also evaluated. The skin is locally reinforced to a thickness of 2mm in a quasi-isotropic laminate. The holes are located 2.5 times the hole diameter from the edge. The combined peak elastic force and aerodynamic loads cause the shear force to vary from -21N to 81N per hole, where a positive force causes tension in the skin. The bearing stress for the 81N load is 13.5MPa. Net section tension is negligible. The tear out stress is 2.7MPa. Similar to the situation at the leading edge, the fasteners are also loaded axially, though the skin tends to push down on the rib slightly, the reaction moment creates a force couple of 133N with the edge of the rib. Assuming the force is transferred directly from the skin to the shaft of the bolt this would cause approximately 7MPa of shear stress on the surface of the shaft.

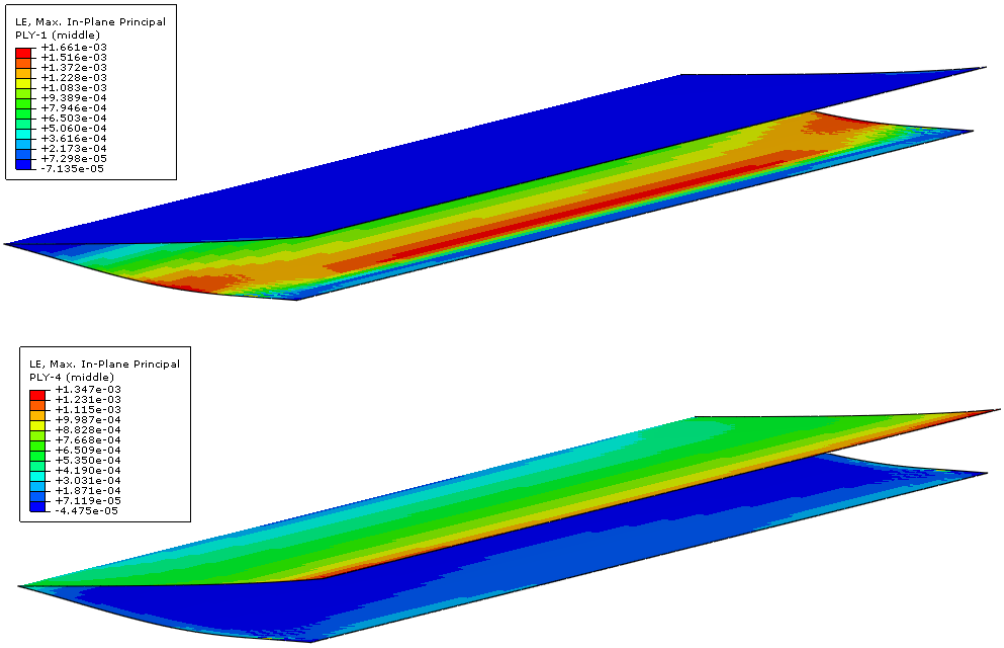

Figure 5.22: The maximum in-plane strain of the trailing edge skin for the outer ply (top) and inner ply (bottom). Maximum symmetric deformation.

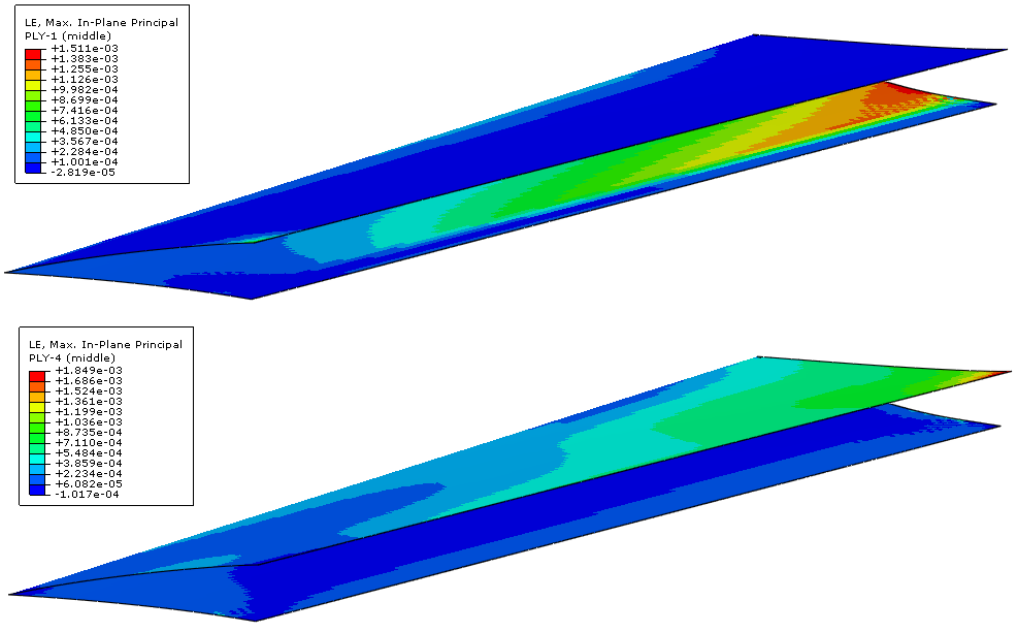

Figure 5.23: The maximum in-plane strain of the trailing edge skin for the outer ply (top) and inner ply (bottom). Maximum asymmetric deformation

Trailing Edge Rib

The internal stresses of the ribs are evaluated using ABAQUS analysis of the part using a 1mm quadratic tet mesh. The skin's reaction forces and aerodynamic loads are applied

to the holes for the fasteners. The following conditions are used: an upward vertical force of 100N is applied to the hole at the extremity of the lower beam, a downward 100N force is applied to the lower hole closest to the spar, and a shear distribution of $1N/mm^2$ over the top surface, totaling a 127N force to the rear. The model is clamped at the hole which connects it with the rear spar. The upper rear edge is constrained in sideways translation to model the constraint imposed by the presence of the skin. The highest stress occurs at the clamped hole, this value may be disregarded as in reality the use of a bolt and washer will distribute the load over a larger area, reducing the peak value. The maximum stress in the rest of the part is around 100MPa, which occurs in the filleted flange between the top and bottom parts.

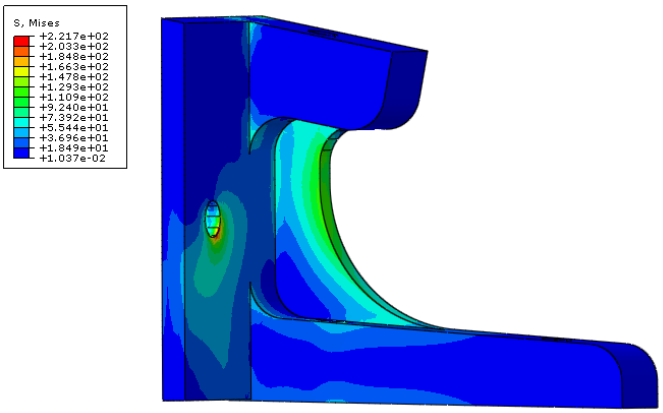

Figure 5.24: The Von Mises stress in the trailing edge rib.

The stresses on the fasteners can be verified using relatively simple mechanical analysis. The ribs are attached to the rear spar web using a single M3 bolt. This bolt experiences a shear force in the order of 20N and a tensile force in the order of 150N. In contrast, the maximum rated tensile force of a class 8.8 M3 bolt is over 3kN.

The guide plates and the top skin are held in place with M3 bolts. The greatest expected tensile load at the lower bolts is 57N, while the upper bolts are expected to experience 81N in shear.

Servo Mount

The servo mount is designed to fit to the three lugs on the servo and attaches to the rear spar with a single M3 bolt. Rotation is constrained by the guide plates contacting the mount along the bottom. The internal stresses are evaluated in an ABAQUS simulation, where a 56N vertical upward force is applied to the outer hole, a 56N vertical downward force is applied to the hole closest to the spar and a 28N force is applied to the rear middle hole. This load case corresponds to the servo exerting maximum torque, and results in a maximum stress of 157MPa. In reality the stresses will be lower as the servo itself adds a load path to the assembly. A 1mm quadratic tet mesh is used in the analysis. A visualization of the results is shown in figure 5.25.

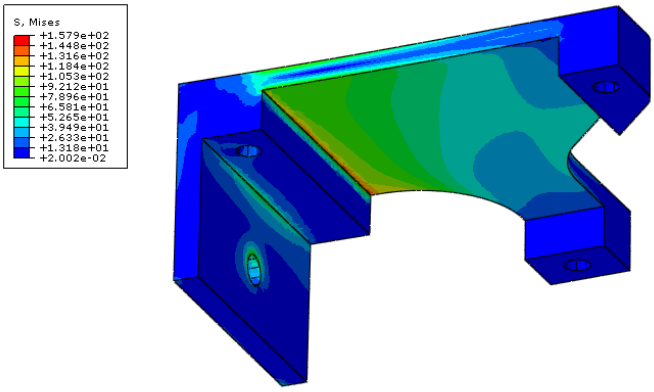

Figure 5.25: The Von Mises stress in the trailing edge servo mount.

Control Horn

The servo connects to ball linkage which in turn actuates a control horn connected to the lower skin at the guide plates. The critical buckling load for the 51mm long linkage is 1455N, the highest expected compressive force is 131N, the highest expected tensile force is 141N. The arm consists of a 2mm thick plate with a 15mm wide flange which is bonded to the lower skin. The 4mm offset of the attachment point of the ball linkage to the neutral plane of the part causes a 150N force to induce a 0.6Nm moment in the horn. This leads to a deflection at the end of 1.14mm. In a worst case scenario this can be combined with the maximum sideways 1.7mm displacement of the lower skin which further angles the force of the pushrod. The sideways component of this force then becomes 5.5% of the actuator force, or 8.3N. This would cause a further 0.4mm sideways displacement of the horn, bringing the total sideways displacement to 3.4mm. The bending moment in the root of the horn becomes 0.93Nm and the peak stress at this location is estimated at 147MPa, which provides a margin of safety of 2 if Al 7075T6 is used.

The bonded flange is 30mm long and 15mm wide, the load case for this joint is a 150N load at the end of the horn which causes a 2.25Nm moment. The bonded joint must therefore react with a 75N force couple over 30mm. Even in the unlikely case that this 75N is concentrated in the outer 15mm edge then this would still be within limits for peel stress on epoxy-Al bonds, which is approximately 300N/25mm.

The ball linkage is connected to the end of the arm by means of a M3 bolt. For a 150N load, the bearing stress around the hole is 25MPa and shear tear-out stress is 15MPa.

Chapter 6

Assembly and Maintenance

The requirement was given to make the system modular to aid in assembly and maintenance. This has been achieved by the use of removable fasteners which allow easy access to all parts. The constant chord of the wing has also allowed the design of a system where all parts are interchangeable between the left and right side.

Another requirement was that the system be easy to maintain and that all actuators remain accessible. This chapter will detail the procedures for assembling the control surfaces and the steps required to access the actuators for servicing or replacement.

6.1 Leading Edge

6.1.1 Assembly

The following steps are required for assembly:

1. bond T-extrusions to skin
2. assemble the ball linkages and adjust the rods to the correct length
3. attach the ball linkages to the ribs and T-extrusions
4. assemble servo mechanism, adjust control rods to correct length
5. attach the servos to the T-extrusions at the extremities
6. route servo wires via surface skin with cable tie mounts
7. insert and fasten bolts connecting ribs to wingbox
8. insert and fasten bolts connecting servo bracket to wingbox
9. insert and fasten bolts connecting upper skin and ribs
10. apply mylar gap sealing tape

6.1.2 Maintenance

In order to access the actuators the entire assembly can be removed as follows:

1. Remove mylar sealing tape
2. Extend the actuators to the full forward position
3. The bolts connecting the servo lugs to the shear web are now accessible through the gap and can be removed
4. With the actuators disconnected the gap can be jacked open even further
5. Remove the M4 bolts holding the ribs in place.
6. The whole leading edge section can be removed and actuators are freely accessible.

6.2 Trailing edge

6.2.1 Assembly

The trailing edge surface is assembled as follows:

1. bond the guide plates to the spacers, observing that the holes are aligned
2. bond the servo horns to the lower skin
3. attach the servo assembly to the servo horn
4. route servo wires via surface skin with cable tie mounts
5. insert the bolts attaching the ribs to the wingbox, do no fully tighten to allow for alignment
6. insert and tighten the bolts attaching the servo brackets to the wingbox
7. insert and fasten the M3 bolts to attach the ribs to the skin
8. tighten the rib bolts through the gap between the lower skin and the wingbox
9. slide guide plates over lower skin, insert and tighten lower bolts

6.2.2 Maintenance

The servos can be accessed by removing the entire assembly:

1. remove bolts connecting guide plates to ribs
2. slide out guide plate
3. remove bolts connecting servo bracket and ribs to wingbox (can be accessed through gap)
4. the whole trailing edge assembly can now be removed and actuators are freely accessible.

6.3 Bill of Materials

Part Name	#	Unit mass [g]	Description
Leading edge skin	1	1030	
Leading edge rib	5	24	
T-extrusion	5	5	
Leading edge servo plate	2	13	
Leading edge servo lug	2	2	
Trailing edge skin	1	680	
Trailing edge rib	5	9	
Guide plates	1	211	
Servo horn	2	5	
Trailing edge servo mount	2	12	
Ball links	28	3	Truck Specs Rod End (M3)
Trailing edge servo	2	28	HBL6625
Leading edge servo	2	68	HS-7950TH
M4x15 countersunk bolts	5		upper LE skin
M3x30 threaded rod	10		LE guide links
M3x75 threaded rod	2		LE servos
M3x20 bolts	20		LE guides
M3x15 bolts	4		LE control linkages
M3 nylock nuts	22		LE guides and servo lugs
M3 DIN433 washer	25		
M4x10 bolts	12		LE ribs, lugs
M4 DIN 9021 washer	12		LE ribs, lugs
M3x10 countersunk bolts	5		TE skin
M3x10 bolts	17		guide plates, TE ribs
M3x5 bolts	6		TE servos

Table 6.1: The bill of materials for one leading edge control surface and one trailing edge control surface. The total mass excluding the fasteners is 2450g.

Chapter 7

Conclusions

This report has shown the design of morphing control surfaces incorporating twist and camber morphing for an experimental unmanned aerial vehicle. Various concepts have been proposed for the wing configuration, the control surface concept, and the type of control surface mechanism. This has resulted in a glass fibre skin design which can reproduce a linear approximation of all requirements for twist and camber within the section of the span which was assigned to be equipped with the control surfaces. A detail design has also been proposed and has been analyzed with various numerical and analytical methods to verify the structural soundness of the mechanism. The design is completed to a workshop ready state and technical drawings are provided, as are assembly and maintenance procedures.

The limitations of the concept as applied in this particular application are that some sections of the wing are not equipped with adaptive surfaces, and therefore remain at a constant camber and twist angle. A wing with full span leading and trailing edge surfaces can be made using this modular design, though it cannot be combined with a full chord span extension system.

Suggestions for future research on the topic would include a more in depth optimization of the skin thickness to reduce weight and elastic actuation loads. This can be combined with an aerodynamic study to improve the aerodynamic properties of the deformed shape via a topological optimization. The current limitation to only linear twist distributions can be partly mitigated by placing many short modules along the span, which would enable the wing to assume a wider variety of lift distributions.

This technology may also find future applications in wind turbine rotor design. Current variable pitch rotors have a fixed twist distributions and rotate the entire blade to optimize for varying wind speeds. This technology has the potential to achieve a optimal angles of attack over the entire blade span while also offering a better actuation response for active gust alleviation.

References

[1] Silvestro Barbarino, Onur Bilgen, Rafic M. Ajaj, Michael I. Friswell, and Daniel J. Inman. A review of morphing aircraft. *Journal of Intelligent Material Systems and Structures*, 22(9):823–877, 2011.

[2] Jason Bowman, Brian Sanders, Bryan Cannon, Jayanth Kudva, Shiv Joshi, and Terrence Weisshaar. Development of Next Generation Morphing Aircraft Structures. In *48th AIAA/ASME/ASCE/AHS/ASC Structures, Structural Dynamics, and Materials Conference*, 2007.

[3] F.M. Catalano, P.C. Greco Jr, and A.L. Martins. Viscous and Wave Drag Optimization for a Transport Aircraft Mission Adaptive Wing. In *Proceedings of the ICAS 2002 CONGRESS*, 2002.

[4] Andrea Ciarella. Baseline Wing Aerodynamic Design . Technical report, ARA, 2013.

[5] Andrea Ciarella. High Speed, Take Off and Landing Wing Aerodynamic Design. Technical report, ARA, 2013.

[6] Boeing Advanced Systems Co. AFTI/F-1ll Mission Adaptive Wing Briefing to Industry. Technical report, Boeing, 1988.

[7] EASA. Certification Specifications for Normal, Utility, Aerobatic, and Commuter Category Aeroplanes. http://easa.europa.eu/system/files/dfu/CS-23%20Amdt%203.pdf.

[8] FAA. *Standard Operating Procedures for Flight Deck Crewmembers*, 2000.

[9] Erdogan Tolga Insuyu. Aero-structural Design And Analysis Of An Unmanned Aerial Vehicle And Its Mission Adaptive Wing. Master's thesis, METU, 2010.

[10] Jamey D. Jacob, Jr. James E. Lumpp, Suzanne Weaver Smith, and William T. Smith. Multidisciplinary Design Experience of a High Altitude Inflatable Wing UAV for Aerospace Workforce Development. In *44th AIAA Aerospace Sciences Meeting and Exhibit*, Reno, Nevada, January 2006.

[11] Sridhar Kota, Joel Hetrick, Russell Osborn, Donald Paul, Ed Pendleton, Peter Flick, and Carl Tilmann. Design and application of compliant mechanisms for morphing aircraft structures. In *Proceedings of SPIE Vol. 5054*, 2003.

[12] Vincent LAJUX. *Methodology for the Design of Leading Edge DevicesApplied to Variable Camber*. Ph.D. Thesis, Cranfield University, 2007.

[13] Deltech Controls LLC. Ethylene Propylene Diene Monomer (EPDM). http://www.deltechcontrols.com/seat_material_ds.pdf.

[14] Lockheed Martin. *Flight Manual F16A/B blocks 10 and 15*, 1995.

[15] Mathias Mueller. Grob G 104 Speed Astir II B Erfahrungsbericht. http://www.segelflug.de/tests/SPEED-ASTIR/.

[16] US Navy. *F14 Pilot's Flight Operating Manual*.

[17] Robert Rosenbaum and A. A. Vollmecke. Simplified Flutter Prevention Criteria for Personal Type Aircraft. Technical Report Airframe and Equipment Engineering Report No. 45, Civil Aeronautics Administration, Washington, D.C., 1952.

[18] Brian Roth, Chris Peters, and William A. Crossley. Aircraft Sizing With Morphing As An Independent Variable: Motivation, Strategies And Investigations. In *AIAA's Aircraft Technology, Integration, and Operations (ATIO) 2002 Technical*, 2002.

[19] Peter K. C. Rudolph. High-Lift Systems on Commercial Subsonic Airliners. Technical Report NASA Contractor Report 4746, NASA, 1996.

[20] T. J. Slaybough. Something Missing. *Aerospace Safety*, 20 (4): 4 – 7, 1964.

[21] J.W. Slooff, W.B. de Wolf, H.M.M. van der Wal, and J.E.J. Maseland. Aerodynamic and aero-acoustic effects of flap tip fences. Technical report, NLR, 2002.

[22] Hansjorg Streifeneder. Adhesive tapes, pre-bent mylar seals adhesive tape, 3-D-Turbulator tapes, combi-tapes, teflon tapes, textile tapes. http://www.streifly.de/shop%20baender-e.htm.

[23] TEKEVER. CHANGE Project Summary. http://change.tekever.com/homepage.

[24] Stephen V. Thornton. Reduction of Structural Loads Using Maneuver Load Control on the Advanced Fighter Technology Integration AFTI/F-111 Mission Adaptive Wing. Technical report, NASA, 1993.

[25] G. A. A. Thuwis. *Stiffness and Layout Tailoring of a Morphing High-lift System with Aeroelastic Loads*. Ph.D. Thesis, TU Delft, 2012.

[26] Anton van Beek. Werktuigbouw en Tribologie. http://www.werktuigbouw.nl.

[27] Roelof Vos. Post-Buckled Precompressed elements: a new class of control actuators for morphing wing UAVs. Technical report, TUDelft, Auburn University, 2005.

[28] Roelof Vos, Zafer Gurdal, and Mostafa Abdalla. Mechanism for Warp-Controlled Twist of a Morphing Wing. *Journal of Aircraft*, 47 (2): 450 – 457, 2010.

[29] Terrence A. Weisshaar. Morphing Aircraft Technology New Shapes for Aircraft Design. Technical report, DARPA, 2006.

[30] Terrence A. Weisshaar. Morphing aircraft systems: Historical perspectives and future challenges. *Journal of Aircraft*, 50(2), 2013.

[31] R Whitford. *Design for Air Combat*. Janes Information Group, 1982.

Appendix A

Technical Drawings

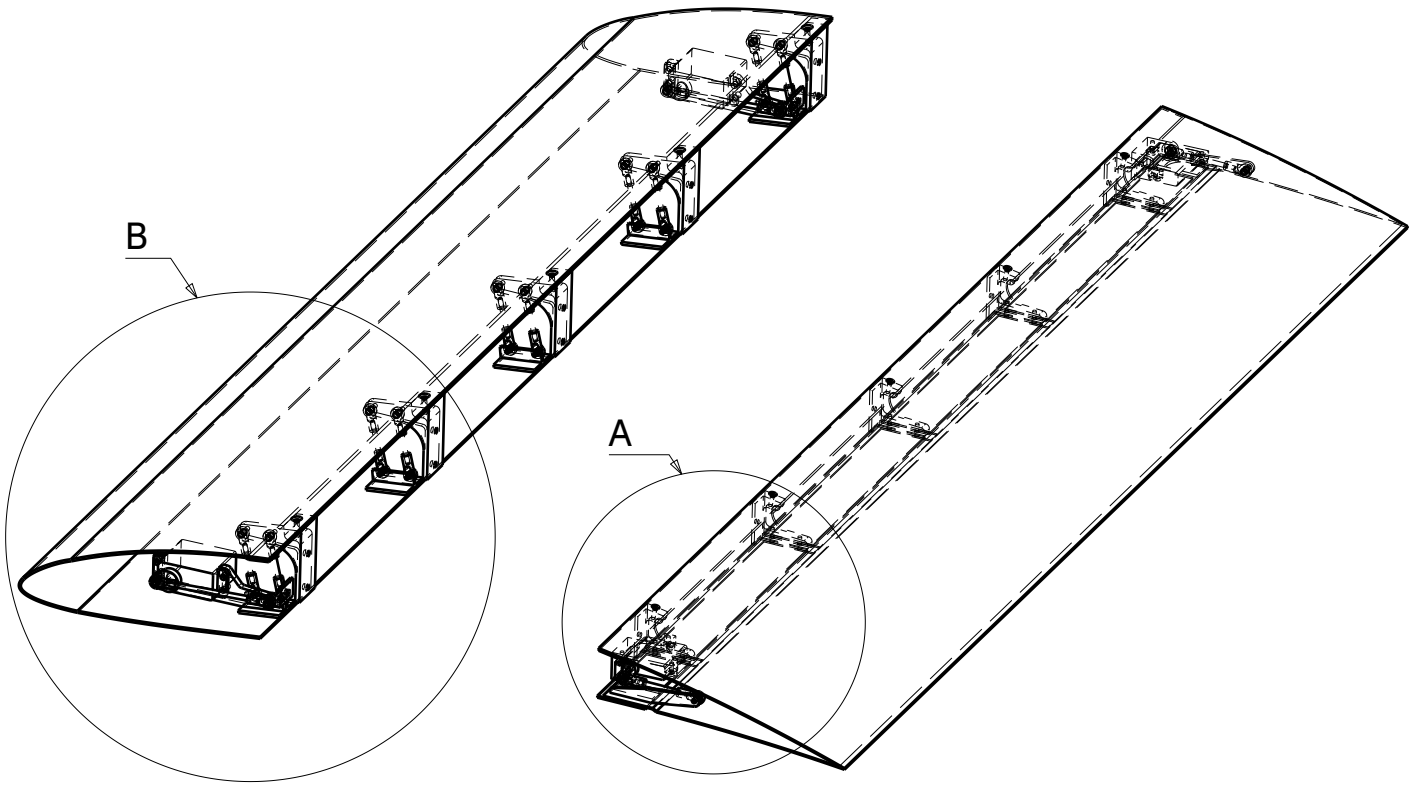

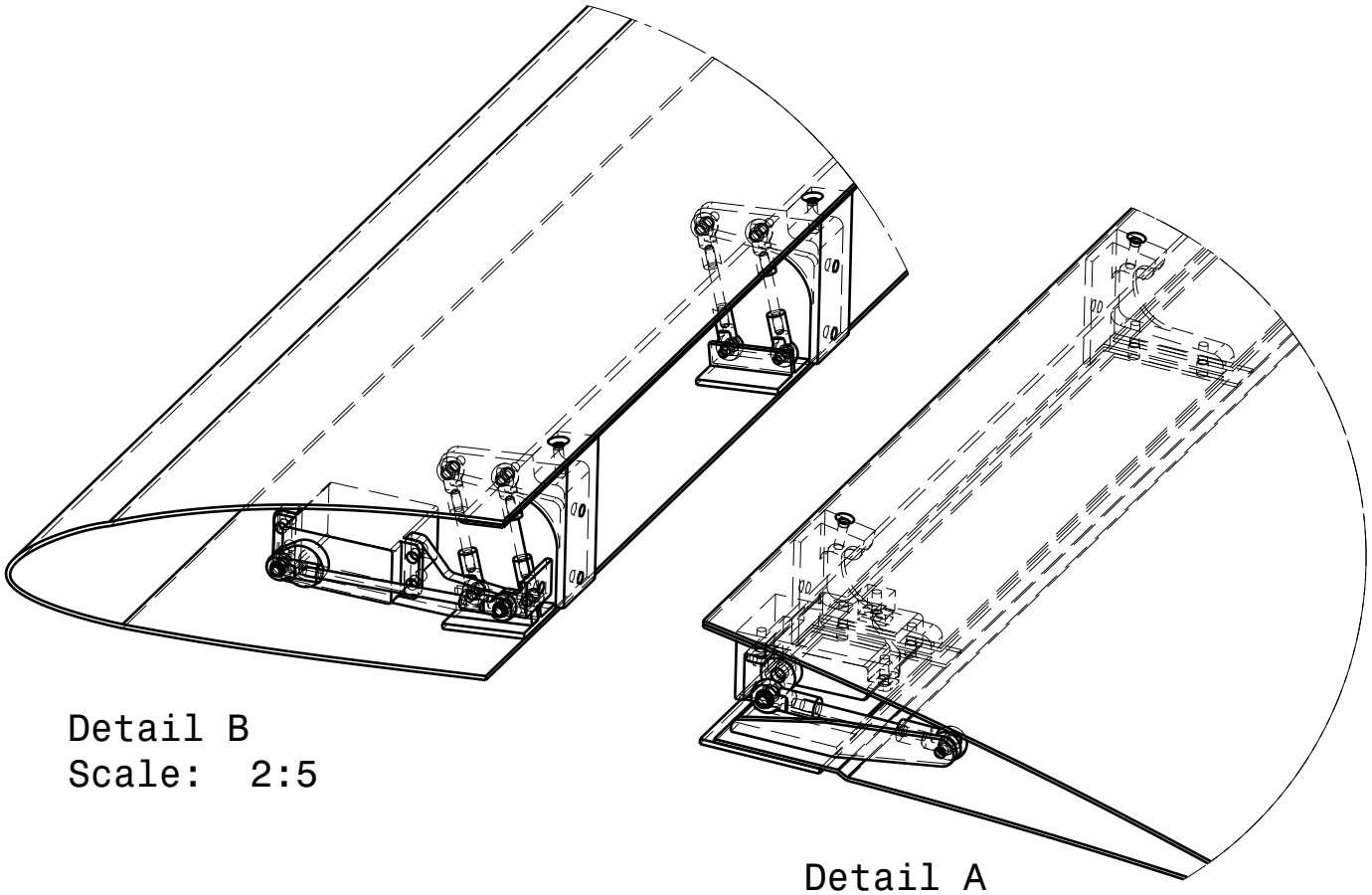

Detail B
Scale: 2:5

Detail A
Scale: 1:2

3mm countersunk hole,
locally reinforce with
extra GFRP layers

2.5

9

15

Side view
Scale: 1:1

Roughen with peelply
to improve bond with
T-extrusion

5

1.5

[45/0/45/0/45/0] quasi isotropic layup

NACA 6510 shape

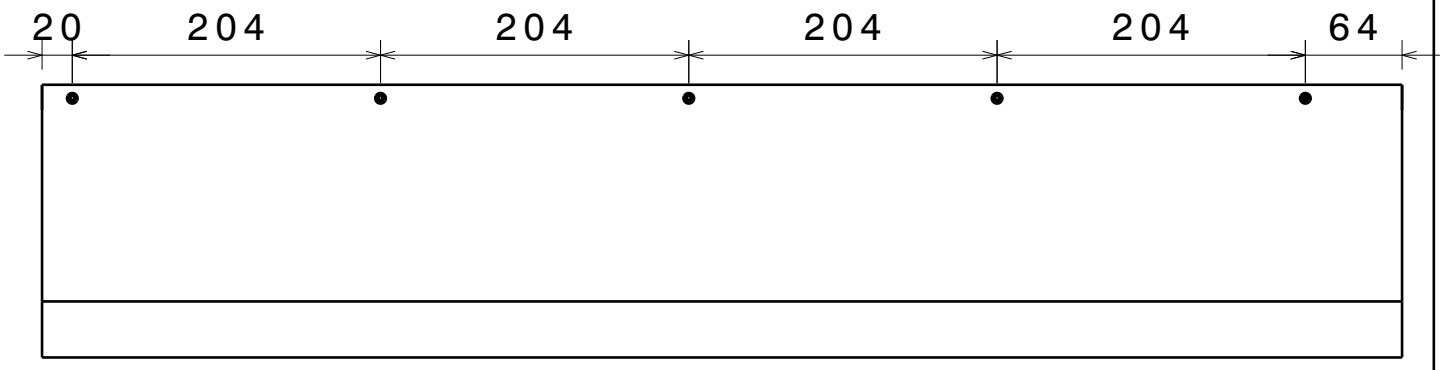

Top view
Scale: 1:5

SIZE	PART NAME	MATERIAL
A4	LE skin	EHG250-68-37
SCALE 1:1	WEIGHT(g) 1030	SHEET 1/1

Isometric view
Scale: 1:1

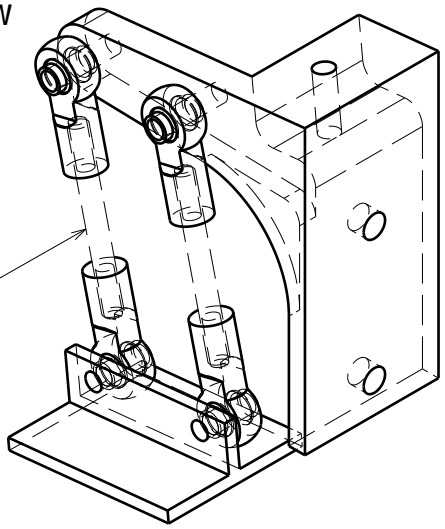

Ball linkages connect
with M3 threaded rod

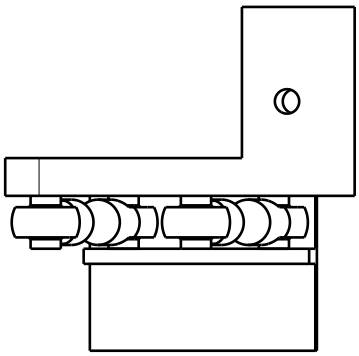

Fasten with M3
bolts and lock nuts

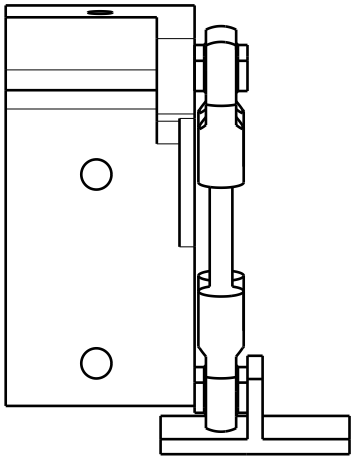

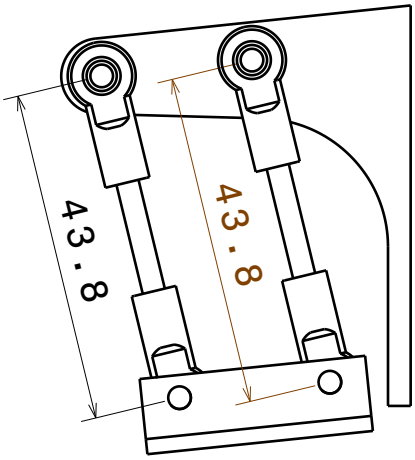

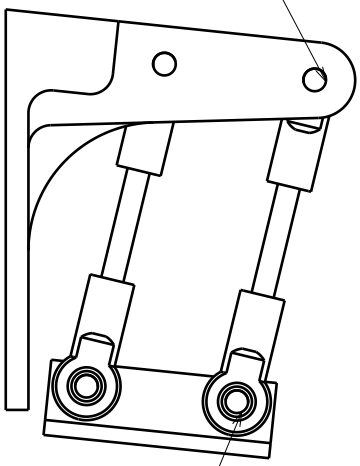

Fasten with M3
bolts and lock nuts

SIZE	NAME	MATERIAL
A4	LE linkages	-
SCALE 1:1	WEIGHT(g) -	SHEET 1/1

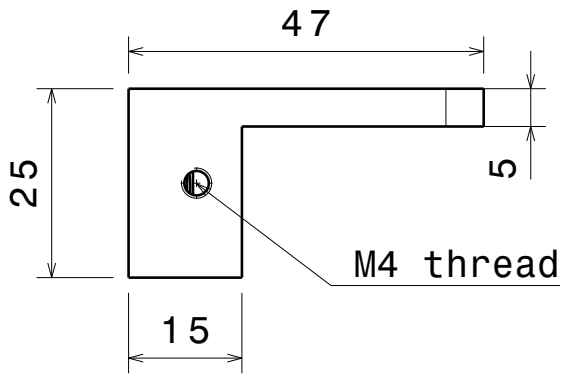

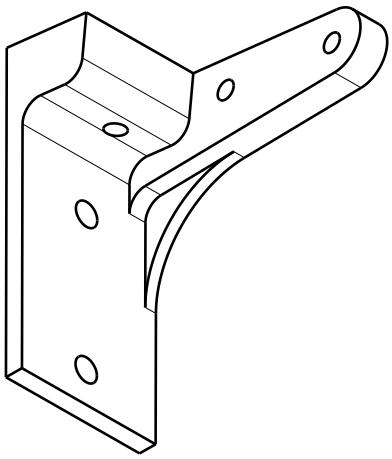

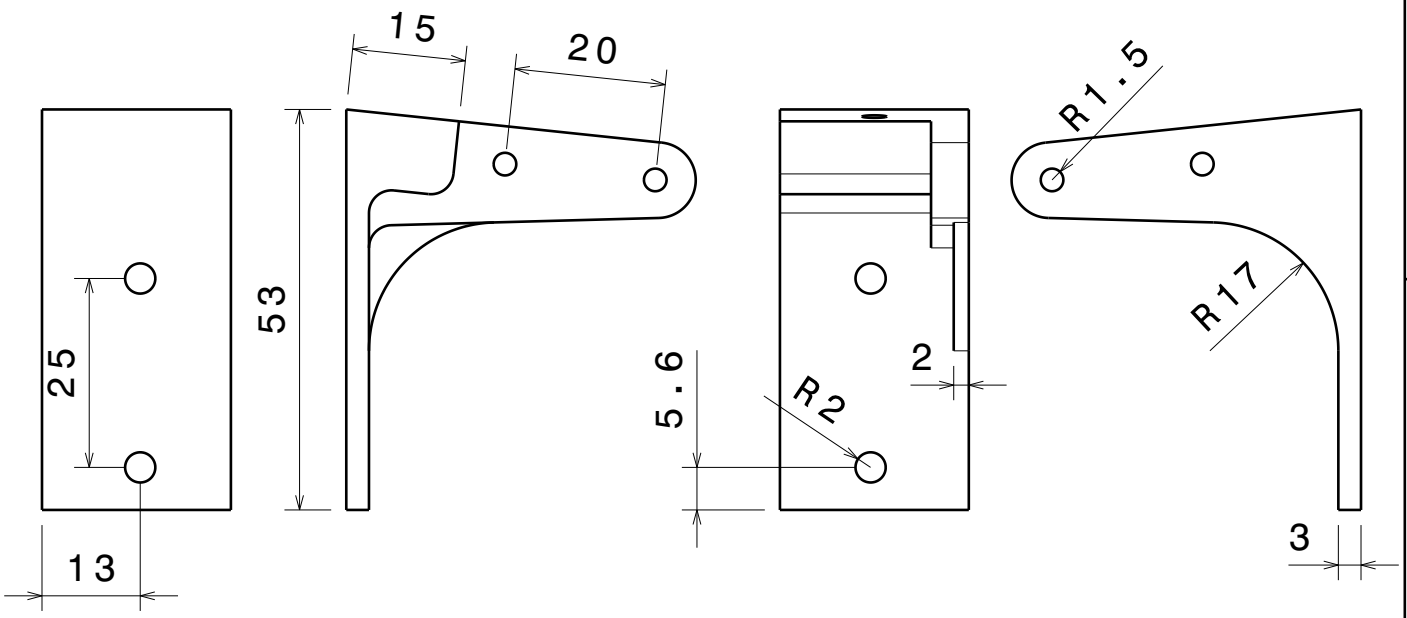

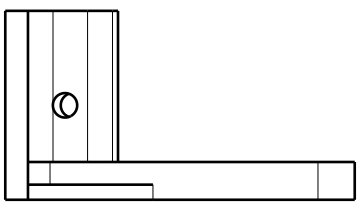

SIZE	PART NAME	MATERIAL
A4	LE rib	Al 7075 T6
SCALE 1:1	WEIGHT(g) 24	SHEET 1/1

Isometric view
Scale: 1:1

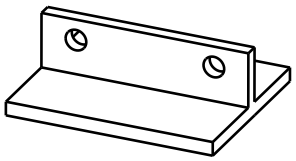

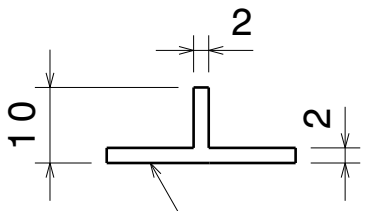

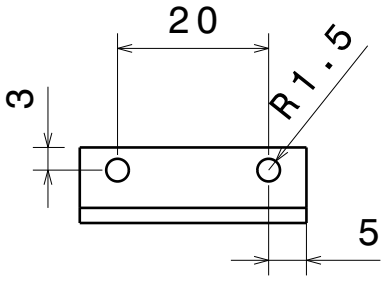

Prepare surface for bonding

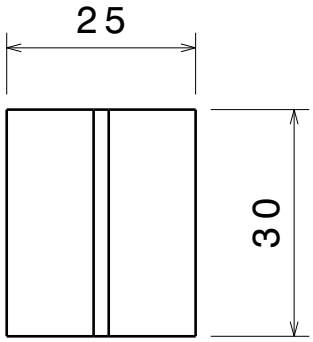

SIZE	PART NAME	MATERIAL
A4	T-extrusion	Al 6060 T66
SCALE 1:1	WEIGHT(g) 5	SHEET 1/1

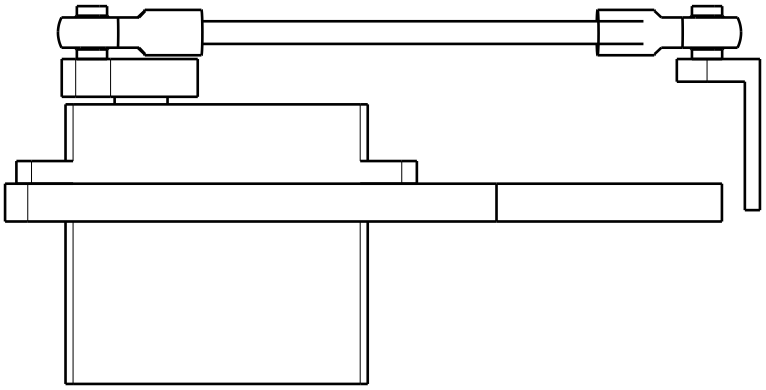

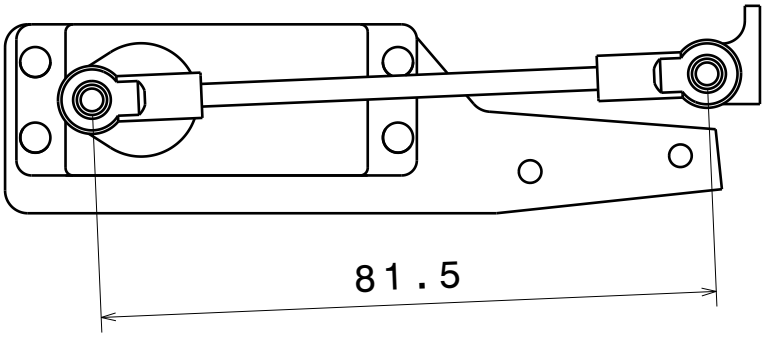

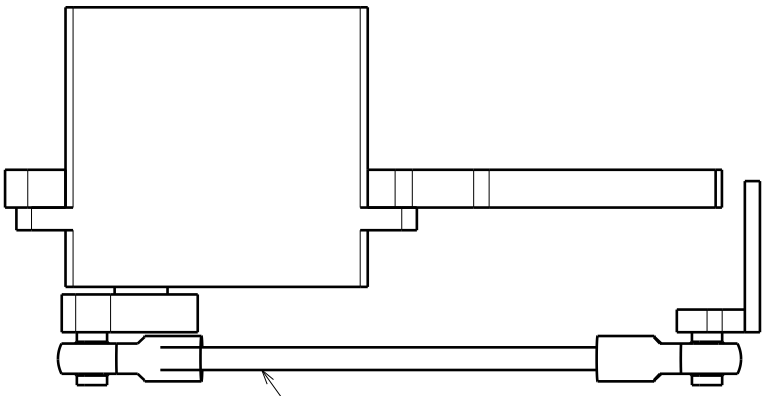

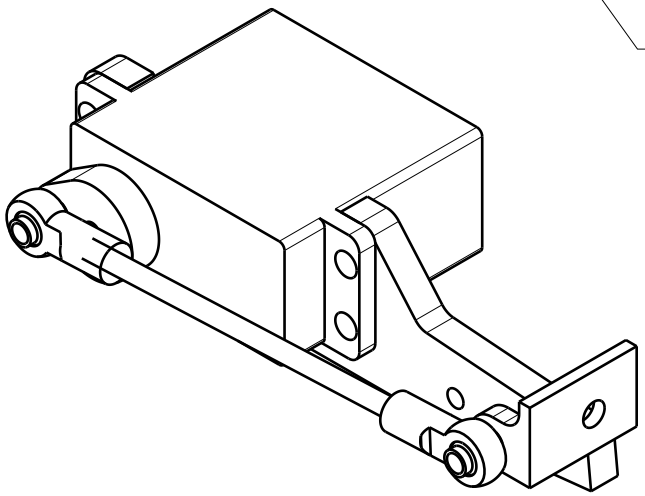

SIZE	NAME	MATERIAL
A4	LE servo assembly	-
SCALE 1:1	WEIGHT(g) -	SHEET 1/1

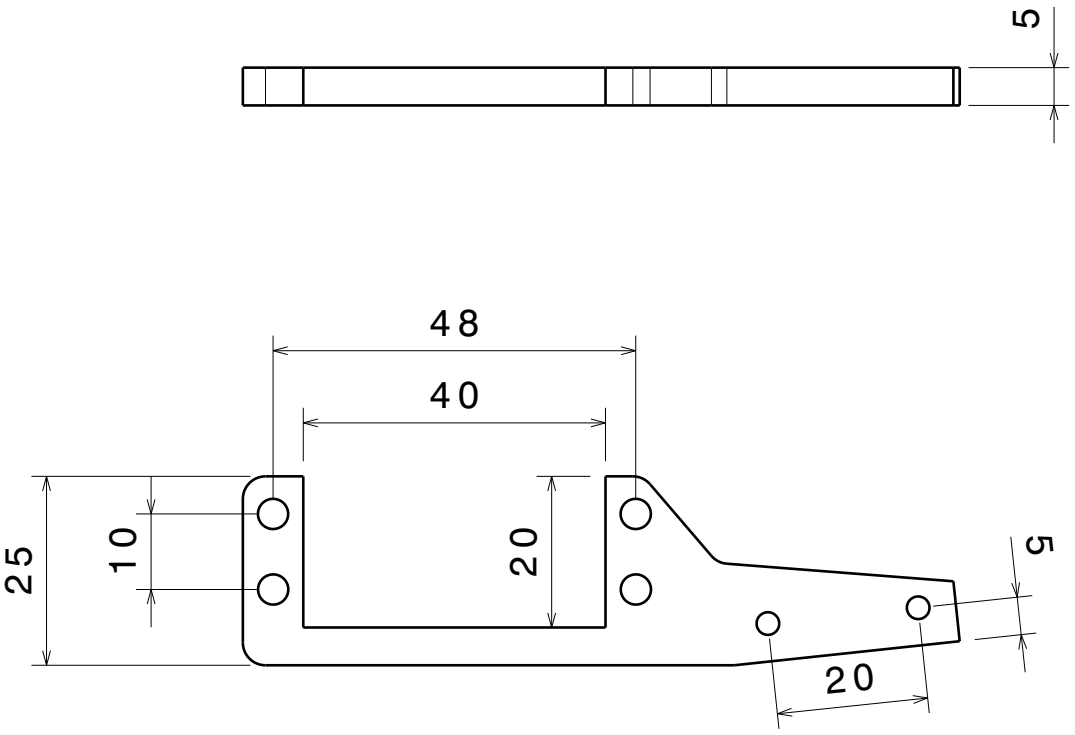

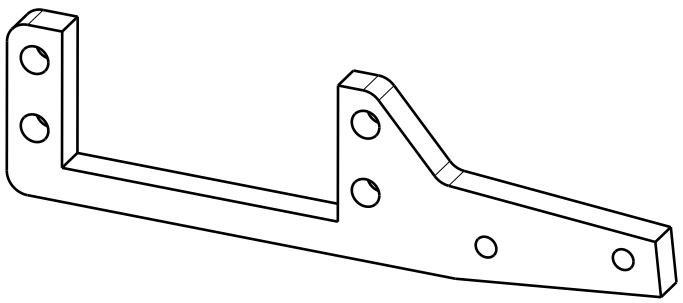

SIZE	PART NAME	MATERIAL
A4	LE servo plate	Al 7075 T6
SCALE 1:1	WEIGHT(g) 13	SHEET 1/1

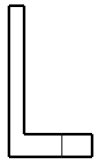

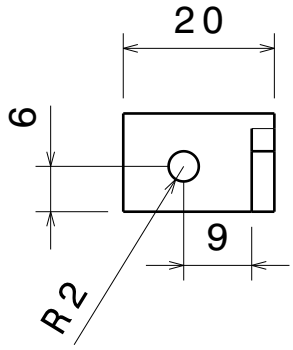

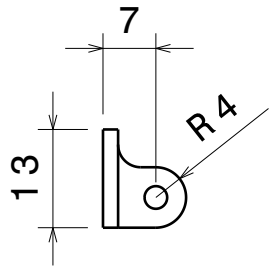

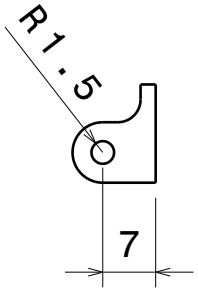

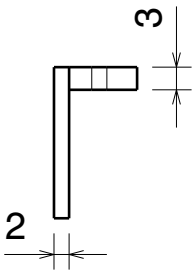

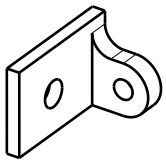

Isometric view
Scale: 1:1

SIZE	PART NAME	MATERIAL
A4	LE Servo lug	Al 7075 T6
SCALE 1:1	WEIGHT(g) 2	SHEET 1/1

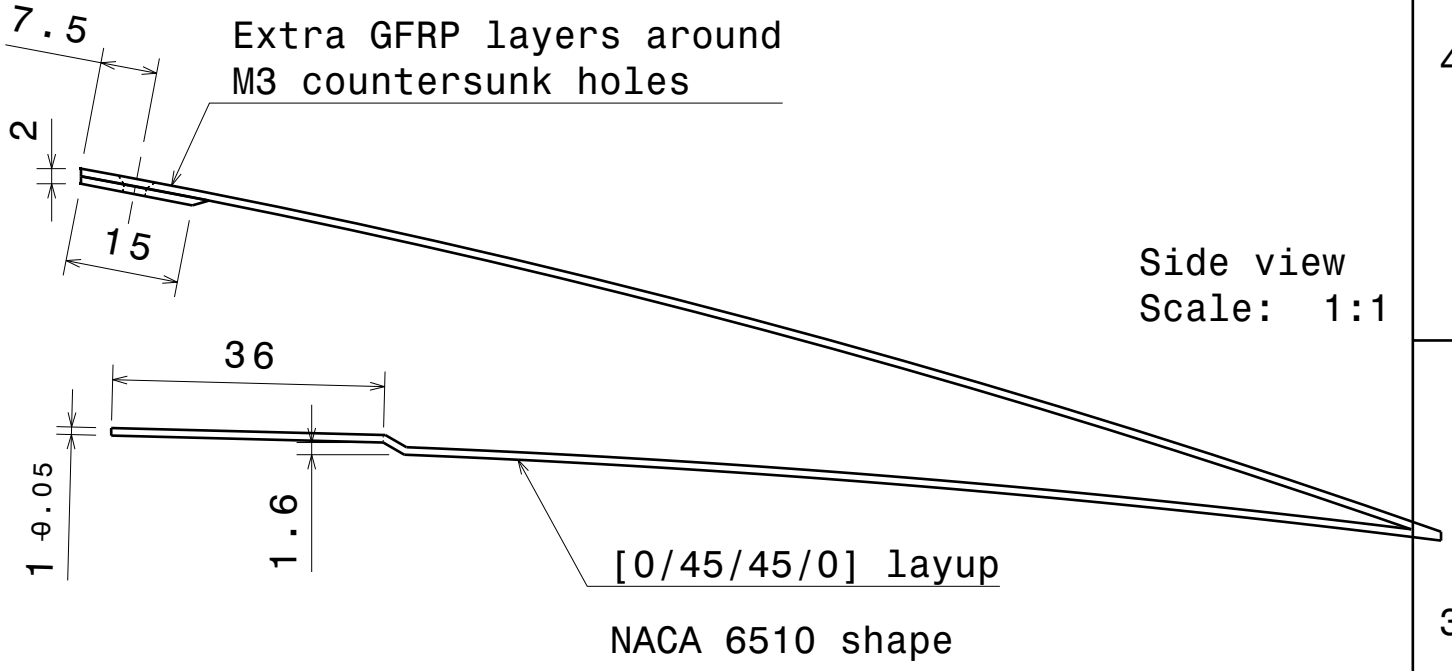

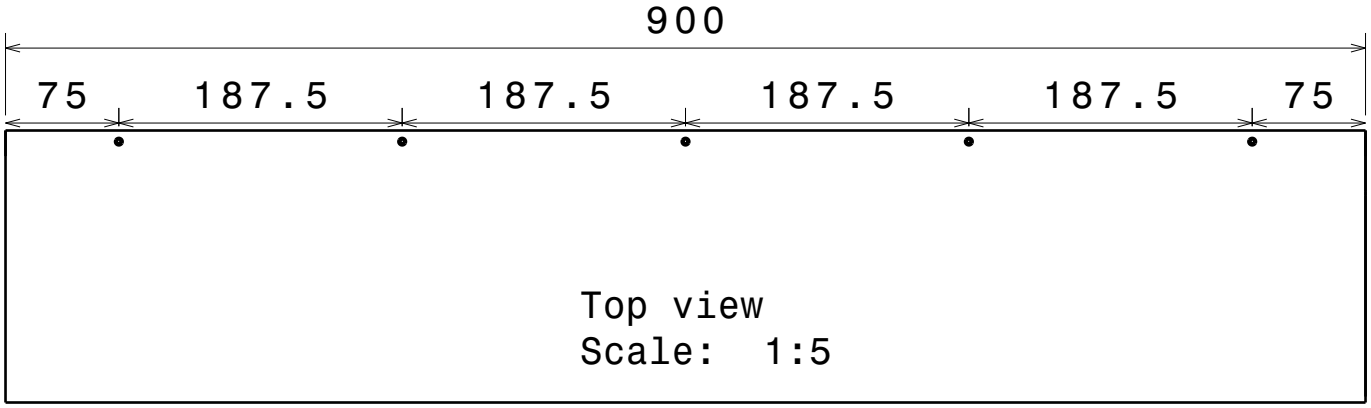

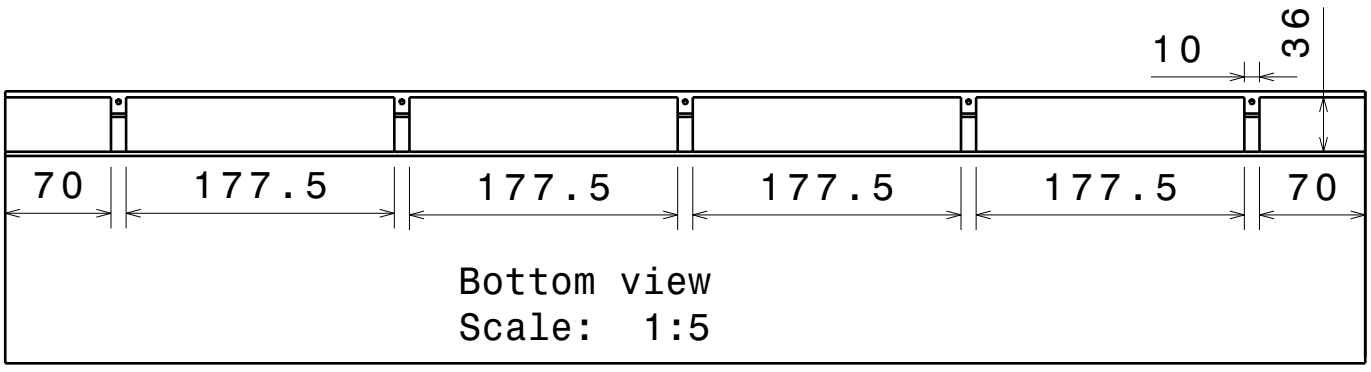

SIZE	PART NAME	MATERIAL
A4	TE skin	EHG250-68-37
SCALE 1:1	WEIGHT(g) 680	SHEET 1/1

M3 thread
perpendicular
to surface

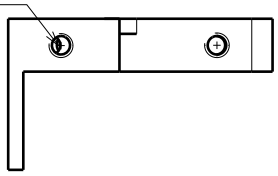

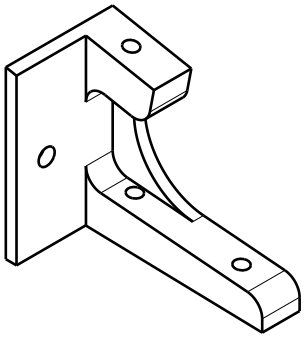

Isometric view
Scale: 1:1

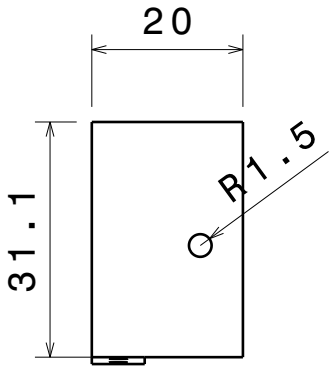

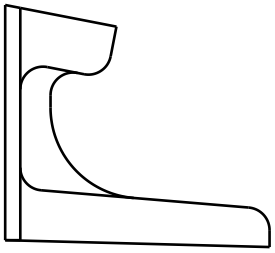

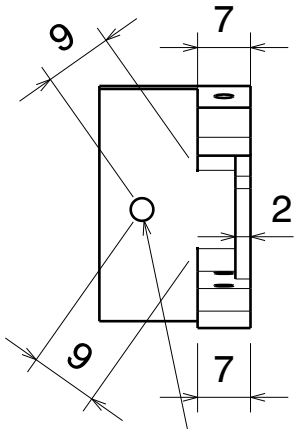

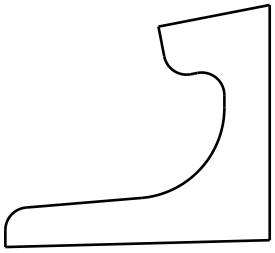

9mm clearance
for access with
5.5mm ratcheting
ring spanner

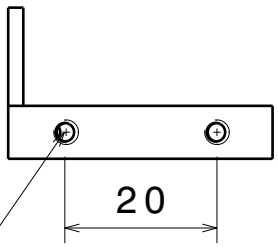

M3 thread
perpendicular
to surface

SIZE	PART NAME	MATERIAL
A4	TE rib	Al 7075 T6
SCALE 1:1	WEIGHT(g) 9	SHEET 1/1

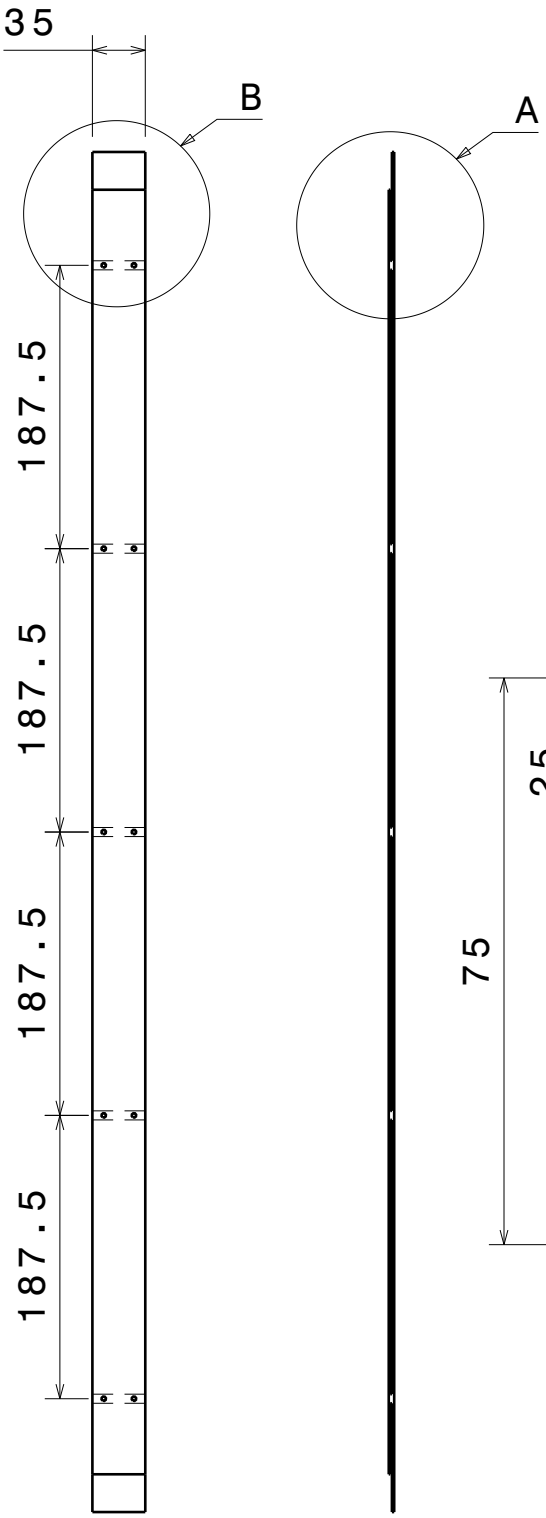

Top view
Scale: 1:5

Front view
Scale: 1:5

Isometric view
Scale: 1:5

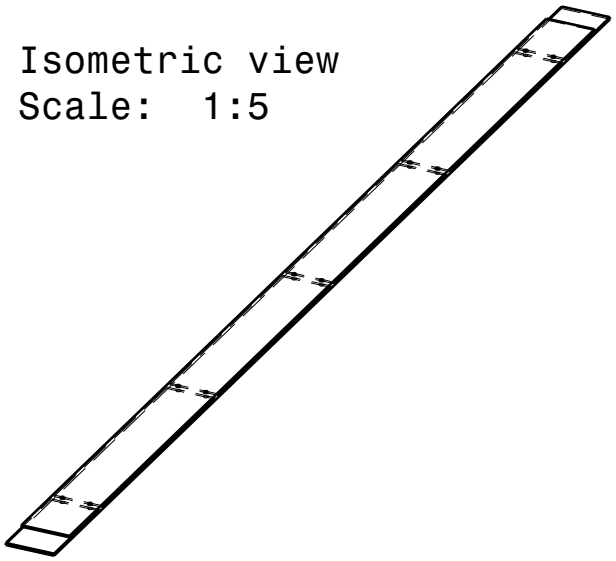

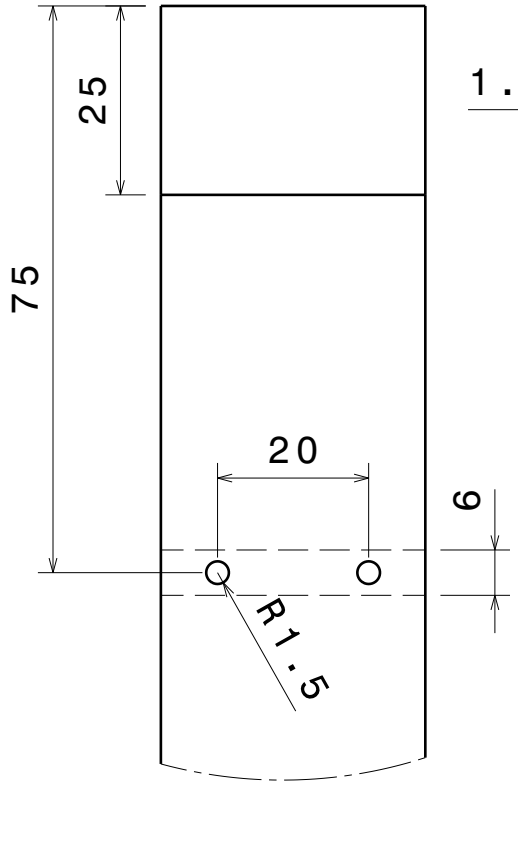

Detail B
Scale: 1:1

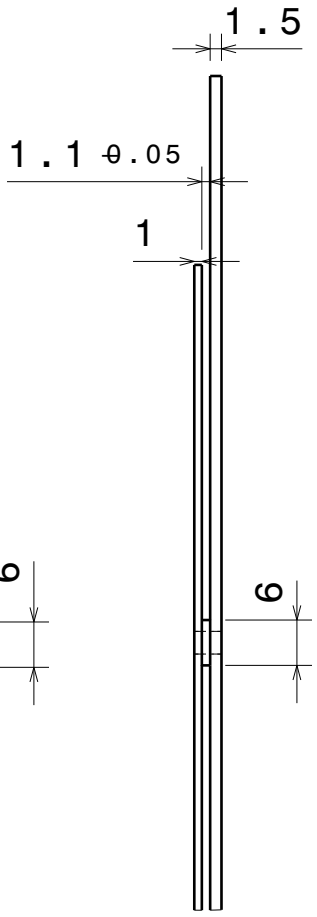

Detail A
Scale: 1:1

SIZE	PART NAME	MATERIAL
A4	Guide plates	Al 6061 T6
SCALE 1:5	WEIGHT(g) 211	SHEET 1/1

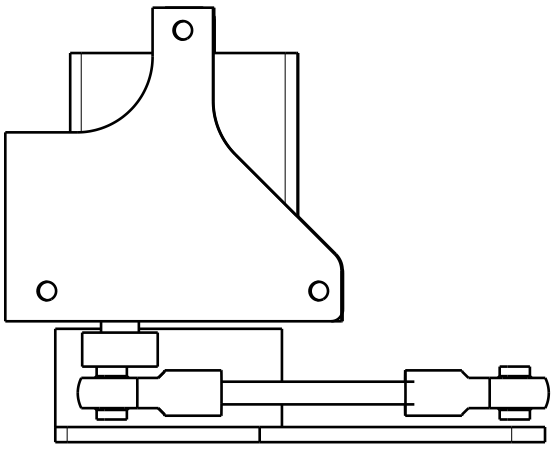

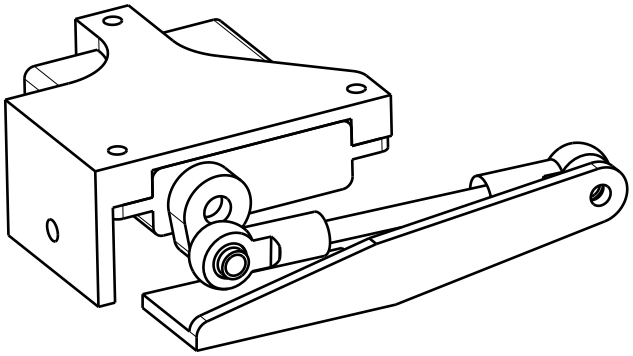

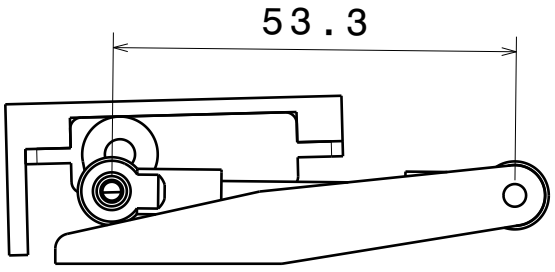

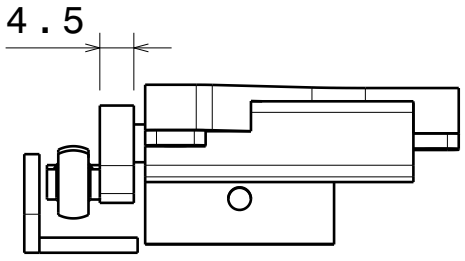

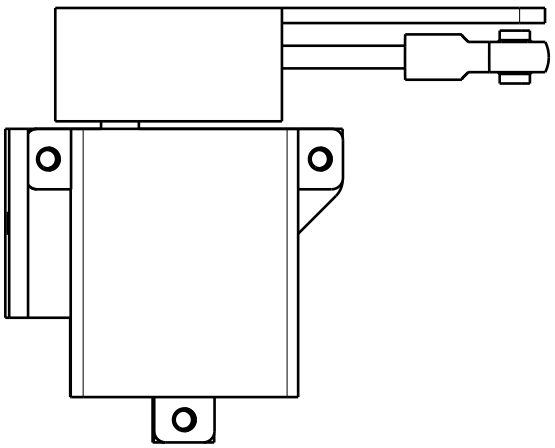

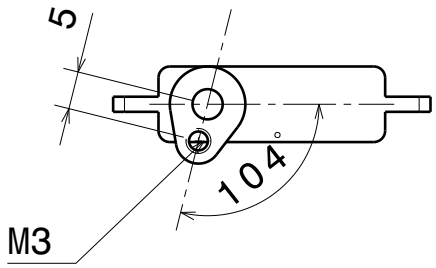

Servo arm in
neutral position

SIZE	NAME	MATERIAL
A4	TE servo assembly	-
SCALE 1:1	WEIGHT(g) -	SHEET 1/1

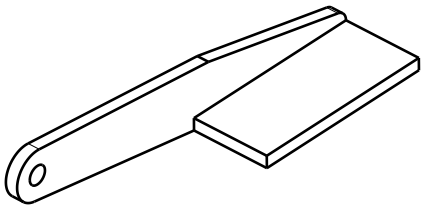

Isometric view
Scale: 1:1

Prepare surface
for bonding with
skin

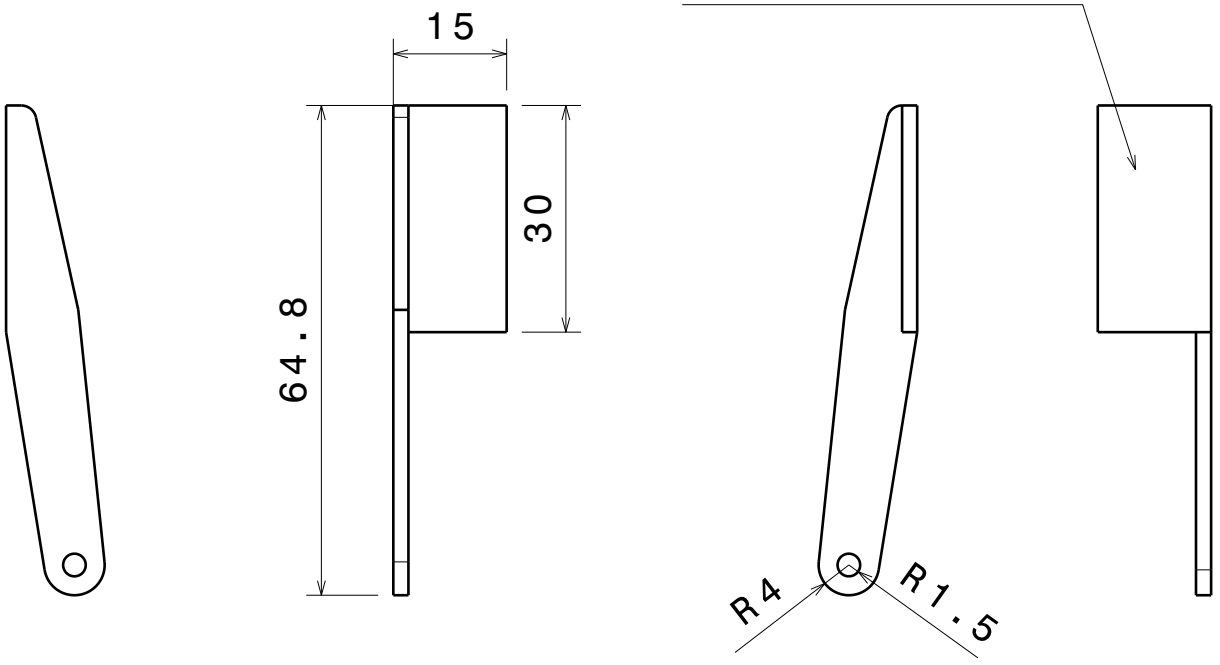

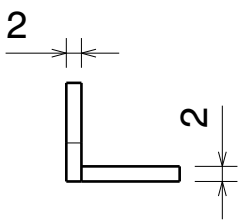

Bottom view
Scale: 1:1

SIZE	PART NAME	MATERIAL
A4	Servo horn	Al 2024 T3
SCALE 1:1	WEIGHT(g) 5	SHEET 1/1

Isometric view
Scale: 1:1

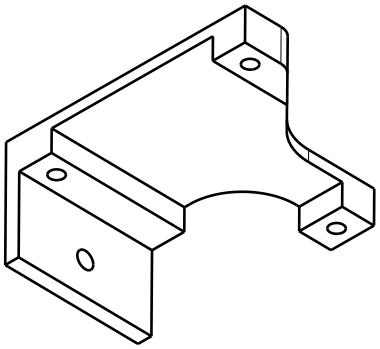

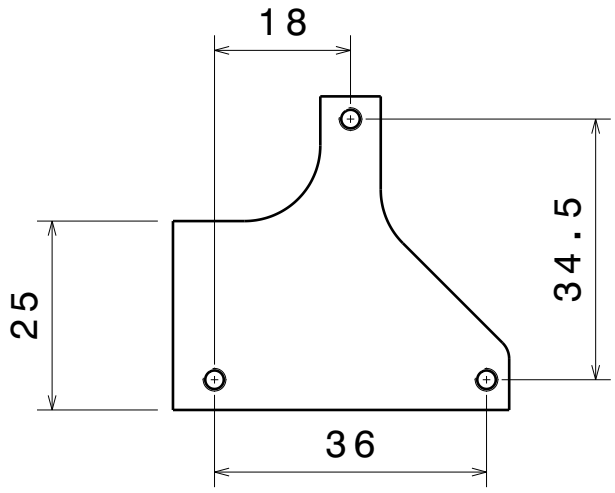

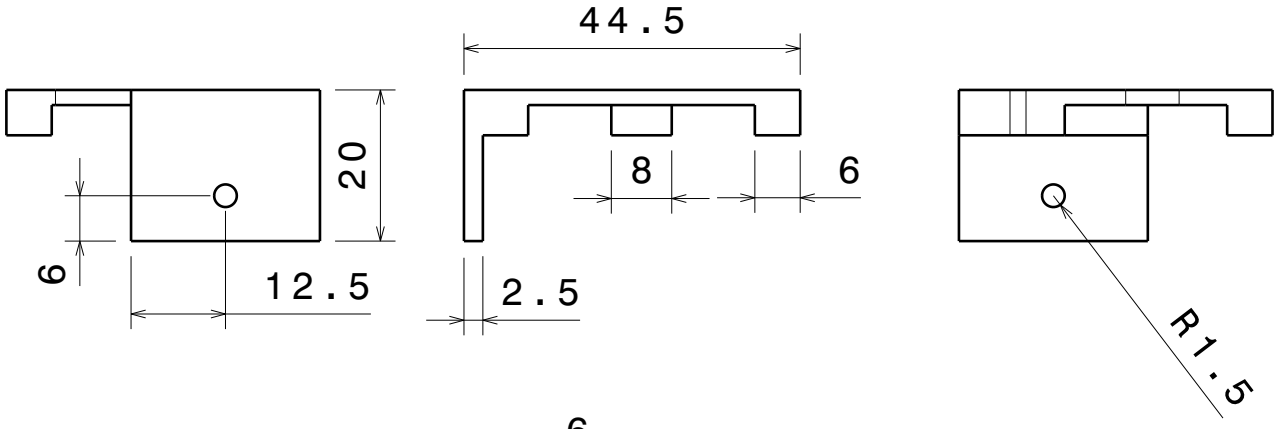

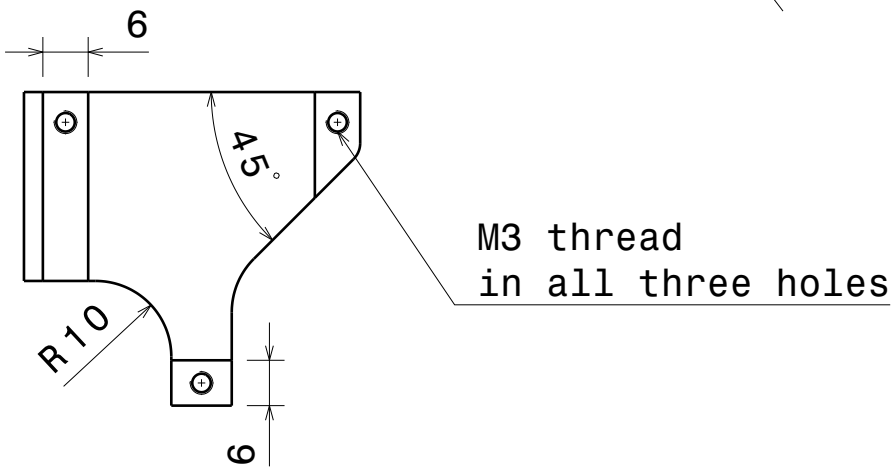

SIZE	PART NAME	MATERIAL
A4	TE servo mount	Al 7075 T6
SCALE 1:1	WEIGHT(g) 12	SHEET 1/1